The Astrophysical Journal, 966:130 (50pp), 2024 May 1 https://doi.org/10.3847/1538-4357/ad303c

Investigating the Drivers of Electron Temperature Variations in H II Regions with Keck-KCWI and VLT-MUSE

Ryan J. Rickards Vaught[1], Karin M. Sandstrom[2], Francesco Belfiore[3], Kathryn Kreckel[4], J. Eduardo Méndez-Delgado[4], Eric Emsellem[5,6], Brent Groves[7], Guillermo A. Blanc[8,9], Daniel A. Dale[10], Oleg V. Egorov[4], Simon C. O. Glover[11], Kathryn Grasha[12,13,17], Ralf S. Klessen[11,14], Justus Neumann[15], and Thomas G. Williams[16]

[1] Center for Astrophysics and Space Sciences, Department of Physics, University of California, San Diego, 9500 Gilman Drive, La Jolla, CA 92093, USA; rjrickar@ucsd.edu
[2] Department of Astronomy & Astrophysics, University of California, San Diego, 9500 Gilman Drive, La Jolla, CA 92093, USA
[3] INAF—Osservatorio Astrofisico di Arcetri, Largo E. Fermi 5, I-50157 Firenze, Italy
[4] Astronomisches Rechen-Institut, Zentrum für Astronomie der Universität Heidelberg, Mönchhofstr. 12-14, D-69120 Heidelberg, Germany
[5] European Southern Observatory, Karl-Schwarzschild Straße 2, D-85748 Garching bei München, Germany
[6] Univ Lyon, Univ Lyon1, ENS de Lyon, CNRS, Centre de Recherche Astrophysique de Lyon UMR5574, F-69230 Saint-Genis-Laval, France
[7] International Centre for Radio Astronomy Research, University of Western Australia, 7 Fairway, Crawley, 6009 WA, Australia
[8] Observatories of the Carnegie Institution for Science, 813 Santa Barbara Street, Pasadena, CA 91101, USA
[9] Departamento de Astronomía, Universidad de Chile, Camino del Observatorio 1515, Las Condes, Santiago, Chile
[10] Department of Physics & Astronomy, University of Wyoming, Laramie, WY 82071, USA
[11] Universität Heidelberg, Zentrum für Astronomie, Institut für Theoretische Astrophysik, Albert-Ueberle-Str. 2, 69120, Heidelberg, Germany
[12] Research School of Astronomy and Astrophysics, Australian National University, Canberra, ACT 2611, Australia
[13] ARC Centre of Excellence for All Sky Astrophysics in 3 Dimensions (ASTRO 3D), Australia
[14] Universität Heidelberg, Interdisziplinäres Zentrum für Wissenschaftliches Rechnen, Im Neuenheimer Feld 205, D-69120 Heidelberg, Germany
[15] Max-Planck-Institut für Astronomie, Königstuhl 17, D-69117 Heidelberg, Germany
[16] Sub-department of Astrophysics, Department of Physics, University of Oxford, Keble Road, Oxford OX1 3RH, UK
Received 2023 August 28; revised 2024 February 23; accepted 2024 March 1; published 2024 May 2

Abstract

H II region electron temperatures are a critical ingredient in metallicity determinations, and recent observations have revealed systematic variations in the temperatures measured using different ions. We present electron temperatures (T_e) measured using the optical auroral lines ([N II]λ5756, [O II]$\lambda\lambda$7320, 7330, [S II]$\lambda\lambda$4069, 4076, [O III]λ4363, and [S III]λ6312) for a sample of H II regions in seven nearby galaxies. We use observations from the Physics at High Angular resolution in Nearby Galaxies survey (PHANGS) obtained with integral field spectrographs on Keck (Keck Cosmic Web Imager) and the Very Large Telescope (Multi-Unit Spectroscopic Explorer). We compare the different T_e measurements with H II region and ISM environmental properties such as electron density, ionization parameter, molecular gas velocity dispersion, and stellar association/cluster mass and age obtained from PHANGS. We find that the temperatures from [O II] and [S II] are likely overestimated due to the presence of electron density inhomogeneities in H II regions. We measure high [O III] temperatures in a subset of regions with high molecular gas velocity dispersion and low ionization parameter, which may be explained by the presence of low-velocity shocks. In agreement with previous studies, the T_e–T_e between [N II] and [S III] temperatures have the lowest observed scatter and follow predictions from photoionization modeling, which suggests that these tracers reflect H II region temperatures across the various ionization zones better than [O II], [S II], and [O III].

Unified Astronomy Thesaurus concepts: Interstellar medium (847); H II regions (694); Spiral galaxies (1560)

Supporting material: machine-readable table

1. Introduction

The characterization of abundance variations within galaxies provides insight into the physical processes that drive galaxy and chemical evolution. A galaxy's gas-phase metal abundance (i.e., metallicity) reflects the history of chemical enrichment from stars and the net balance of gas flows (mixing, outflows, inflows of pristine material, etc.). In addition, the metallicity of interstellar medium (ISM) gas directly controls its cooling and other important ISM physics (Draine 2011; Peimbert et al. 2017).

The distribution of gas-phase metals in a galaxy is commonly traced by the abundance of oxygen, nitrogen, sulfur, and other metals using the emission from ionized gas located inside H II regions (e.g., Kennicutt & Garnett 1996; Bresolin et al. 2012; Hernandez et al. 2013; Ho et al. 2017; Kreckel et al. 2019, 2020; van Loon et al. 2021; Grasha et al. 2022). There are several indirect methods calibrated using strong optical emission lines to derive an estimate of the H II region metallicity (e.g., Kewley & Ellison 2008; Blanc et al. 2015). A "direct" measure of an H II region metallicity requires knowledge of the electron temperature (T_e) of the gas. Due to their exponential dependence on T_e, one of the ways to infer electron temperature is through the auroral-to-nebular line ratios of collisionally excited lines (CEL; Peimbert 1967; Osterbrock & Ferland 2006; Peimbert et al. 2017). Nebular and auroral lines originate from different excited states of ions. Auroral lines are from higher energy levels, but are still

[17] ARC DECRA Fellow.

accessible for collisional excitation in a $T \sim 10^4$ K gas. If the density of the gas is below the auroral and nebular line critical densities (i.e., when collisional de-excitation is negligible), then the auroral-to-nebular line ratio is sensitive to the electron temperature (e.g., Osterbrock & Ferland 2006). Given that the excitations to the auroral level are only accessible to electrons of higher energy, auroral-line emission can be >100 times weaker than nebular lines (Kennicutt et al. 2003; Esteban et al. 2004; Berg et al. 2020). One alternative way to measure T_e includes the ratio between recombination line (RL) emission from H and other species (Peimbert 1967; Osterbrock & Ferland 2006; Peimbert et al. 2017). But, because RLs of ions exhibit a much weaker dependence on temperature ($T_e^{-\kappa}$, where $-0.2 < \kappa < 0.2$; Peimbert et al. 2017), the optical RLs useful for temperature diagnostics are typically reserved for deep, high signal-to-noise ratio (S/N) spectra, as RL emission is typically much fainter than the emission from auroral lines.

For ions with optical auroral lines studied in this work, we can measure the temperatures for each ion using the following line ratios: $T_{e,[O\,III]} \rightarrow$ [O III]λ4363/$\lambda\lambda$4959, 5007, $T_{e,[O\,II]} \rightarrow$ [O II] $\lambda\lambda$7320, 7330/$\lambda\lambda$3726, 3729,[18] $T_{e,[S\,III]} \rightarrow$ [S III]λ6312/$\lambda\lambda$9069, 9532, $T_{e,[S\,II]} \rightarrow$ [S II]$\lambda\lambda$4069, 4076/$\lambda\lambda$6716, 6731, and $T_{e,[N\,II]} \rightarrow$ [N II]λ5756/$\lambda\lambda$6548, 6584. The O^+, N^+, and S^+ ions require energies of 13.6 eV, 14.5 eV, and 10.3 eV to be produced, while S^{++} and O^{++} require energies 23 eV and 35 eV, respectively.

Several effects play competing roles in determining the ionization and temperature structure of H II regions. These include a radially decreasing intensity and hardening of the radiation field (photons closest to 13.6 eV are absorbed first) as well as a change in the ions that dominate gas cooling and therefore the cooling efficiency (Stasińska 1980; Garnett 1992). Because of the varying degree of ionization within an H II region, a model with three ionization zones—low, intermediate, and high—is often used to describe them. Because each ionization zone could theoretically have different temperatures, this further stresses the importance of observing multiple auroral lines and developing temperature priorities for use in accurately determining abundances (e.g., Berg et al. 2015, 2020; Rogers et al. 2021).

Observing the full set of optical auroral lines in an H II region can be challenging. In addition to the large wavelength range needed, ~3700–10000 Å, some auroral lines are weaker than others, depending on the metallicity and temperature of the gas. Because of these challenges, it is very important to establish temperature relationships that allow us to infer the conditions of a certain ionization zone from the others. Photoionization modeling (e.g., Garnett 1992; Vale Asari et al. 2016) has been used to derive temperature relationships, but standard models consider only simple geometries and homogeneous physical and ionization conditions, which might not be suitable for more complex regions potentially affected by shocks, stellar feedback, or other mechanisms that produce density or temperature inhomogeneities (Peimbert 1967; Peimbert et al. 1991; Binette et al. 2012; Berg et al. 2015, 2020; Arellano-Córdova & Rodríguez 2020; Nicholls et al. 2020; Méndez-Delgado et al. 2023a, 2023b).

In the presence of temperature fluctuations, the exponential dependence of CEL strengths on temperature will bias auroral-to-nebular temperatures toward higher values than the true average (Peimbert 1967; Peimbert & Costero 1969). Such inhomogeneities may be related to the presence of turbulence, density structure, and shocks associated with either stellar winds or radiation-pressure-driven expansion. If the sources of temperature inhomogeneities are confined to the central part of the nebula, the effects that these phenomena have on temperature may primarily affect only the high-ionization zone. This has been suggested by Méndez-Delgado et al. (2023a), who presented evidence for temperature inhomogeneities affecting only the highly ionized gas traced by [O III]. In a sample of Galactic and extragalactic H II regions, they observed that differences between [O III] and [N II] temperatures correlated with the degree of deviation from the average temperature measured using faint O II recombination line emission. Furthermore, a strong correlation between the O II recombination and [N II] temperatures observed by Méndez-Delgado et al. (2023a) implies that temperatures inferred from the [N II] auroral line accurately measure the average T_e of the low-ionization zone (Méndez-Delgado et al. 2023a, 2023b).

Due to the importance of obtaining accurate temperatures for precise abundances, significant effort has been devoted to advancing our understanding of the temperatures of different H II region ionization zones. For example, previous works have found that the scatter between temperatures of different ionization zones may be correlated with other properties of the gas, such as the ionization parameter and metallicity (Berg et al. 2015; Arellano-Córdova & Rodríguez 2020; Berg et al. 2020; Yates et al. 2020).

To explore these questions, we use deep 3600–9500 Å IFU mapping to measure the set of optical auroral lines and nebular lines for a sample of H II regions. We use observations obtained from the Keck Cosmic Web Imager (KCWI; Morrissey et al. 2018) and Multi-Unit Spectroscopic Explorer (MUSE; Bacon et al. 2010) to measure the electron temperature from all three ionization zones in H II regions in nearby galaxies. In Section 2, we present our sample galaxies as well as primary and supplemental observations. In Section 3, we discuss the reduction of the KCWI data. We assess the quality of the KCWI mosaics in Section 3.5. We construct our H II region sample in Section 4. We present the auroral-line measurements in Section 5. We derive H II region properties from nebular diagnostics and from Atacama Large Millimeter/submillimeter Array (ALMA) and Hubble Space Telescope (HST) data in Section 6. The results and a discussion are presented in Sections 7 and 8.

2. Observations

The analysis presented here makes joint use of multi-wavelength observations of seven galaxies obtained with Keck-KCWI, VLT-MUSE, ALMA, and the HST.

2.1. Sample Selection

The seven galaxies in this analysis are drawn from the Physics at High Angular resolution in Nearby Galaxies survey (PHANGS)-MUSE sample (Emsellem et al. 2022). To date, 90 galaxies make up the full PHANGS sample[19] (Leroy et al. 2021b), and 19 have been observed by MUSE. In order for them to be observed with KCWI in the northern hemisphere, we selected the seven target galaxies from a subset of

[18] [O II]$\lambda\lambda$7320, 7330 is an unresolved quadruplet with transitions at λ7319, λ7320, λ7330, and λ7331 Å.

[19] http://phangs.org/

Table 1
Properties of the PHANGS-MUSE Galaxies Observed with KCWI

Name	Distance[a] (Mpc)	$\log_{10}(M_*)$ [b] ($M_\odot$)	R_{25}[c] (arcmin)	PSF_{MUSE}[d] (arcsec)	PSF_{KCWI}[e] (arcsec)
NGC 628	9.8 ± 0.6	10.34 ± 0.1	4.9	0.92	2.0 ± 0.4
NGC 1087	15.9 ± 2.2	9.93 ± 0.1	1.5	0.92	1.2 ± 0.1
NGC 1300	19.0 ± 2.3	10.62 ± 0.1	3.0	0.89[f]	1.3 ± 0.1
NGC 1385	17.2 ± 2.6	9.98 ± 0.1	1.7	0.77[f]	1.3 ± 0.1
NGC 2835	12.2 ± 0.9	10.00 ± 0.1	3.2	1.15	1.4 ± 0.1
NGC 3627	11.3 ± 0.5	10.83 ± 0.1	5.1	1.05	1.1 ± 0.1
NGC 5068	5.2 ± 0.2	9.40 ± 0.1	3.7	1.04	1.5 ± 0.4

Notes.
[a] From the compilation of Anand et al. (2021).
[b] Derived by Leroy et al. (2021b), using GALEX UV and the Wide-field Infrared Survey Explorer IR photometry.
[c] From LEDA (Makarov et al. 2014).
[d] The FWHM of the Gaussian point-spread function (PSF) for the homogenized COPT mosaic from PHANGS-MUSE (Emsellem et al. 2022).
[e] The average FWHM of the KCWI PSF for the set of a galaxy's observed pointings.
[f] Denotes galaxies observed with MUSE using ground-based adaptive optics.

PHANGS-MUSE galaxies with decl., $\delta > -30°$. Table 1 presents general properties of these galaxies, including distances, masses, sizes, and the angular resolution of the MUSE data.

2.2. Keck Cosmic Web Imager

We observed each galaxy using KCWI on the Keck II telescope with multiple pointings taken over several nights between the years 2017 and 2021. Clear conditions were present for the majority of observations, except for the nights of 2018 October 16 and 17, which suffered from variable cloud coverage. These poor conditions primarily affect the observations of NGC 628. The instrument was configured with the "Large" slicer and BL grating centered at 4600 Å. The usable spectral range afforded by this configuration is 3650–5550 Å with a spectral resolution $R \sim 900$, corresponding to an FWHM ~ 5.1 Å (or ~ 300 km s^{-1}) at the central wavelength. The Large slicer has an angular slice width of 1.″35. The field of view (FOV) using the Large slicer and BL grating is 33″ perpendicular and 20.″4 parallel to the slicer.

Because the FOV is small compared with the large angular size of each galaxy, we observed each galaxy over multiple fields. Most fields were observed two times using 1200 s (i.e., 20 minutes) integration times. The only exceptions were: all fields in NGC 3627, which were observed five times each with 120 s (2 minutes) integration times; field 17 in NGC 628, which was observed three times using 1200 s; and field 2 in NGC 5068 and field 5 in NGC 1385, both having only a single observation of 1200 s. A half slice width, or 0.″675, dither was applied between each exposure. We observed an off-galaxy region, selected to be free of extended emission and/or bright sources, in order to measure a sky spectrum close in time to the observations. These sky frames, observed using an integration time of 600 s (i.e., 10 minutes), were used for sky subtraction during data reduction. We summarize the number of fields, exposure times, and dates in Table 6 of Appendix A. The full data reduction is outlined in Section 3.

2.3. Multi-Unit Spectroscopic Explorer

MUSE observations of these galaxies come from the PHANGS-MUSE survey (Emsellem et al. 2022). MUSE covers wavelengths between 4800 and 9500 Å. Taken in combination, KCWI and MUSE span the full optical spectrum. The full details of the MUSE data reduction and data products are presented in Emsellem et al. (2022), and we provide a brief overview here. The PHANGS-MUSE program observed 19 galaxies using 168 individual $1' \times 1'$ pointings. The median spatial resolution across all pointings is ~ 50 pc (or $\sim 0.''80$) with a typical spectral FWHM of ~ 2.5 Å (but varying with wavelength). The data were reduced using the `pymusepipe`[20] and spectral fitting, and analysis was performed using the Data Analysis Pipeline[21] packages described in Emsellem et al. (2022). The individual MUSE pointings were homogenized to a uniform Gaussian point-spread function (PSF) with FWHM set to the largest FWHM measured for each target, resulting in "convolved and optimized" (COPT) mosaics. The PSFs of the COPT mosaics are listed in Table 1. We use the COPT mosaics in the following work.

2.4. ALMA

Our analysis makes use of ALMA data obtained as part of PHANGS-ALMA (Leroy et al. 2021b). PHANGS-ALMA observed the $J = 2$–1 rotational transition of ^{12}CO, hereafter CO, for 90 galaxies. The details of the data reduction are described in Leroy et al. (2021a). We make use of the ALMA data cubes with combined CO measurements from the 12 m and 7 m arrays plus Total Power (12m+7m+TP). The nominal angular resolution of 12m+7m+TP observations is $\sim 1.''3$, similar to the resolution of both KCWI and MUSE. The velocity resolution is 2.5 km s^{-1}.

2.5. HST

The PHANGS-HST survey (Lee et al. 2022) observed[22] our target galaxies using five HST filters: F275W (NUV), F336W (U), F438W (B), F555W (V), and F814W (I). Of the high-level data products produced from this data set, we make use of compact star cluster catalogs (Thilker et al. 2022; Maschmann et al. 2024) and multiscale stellar association catalogs (Larson et al. 2023). The association catalog identifies sources using

[20] https://pypi.org/project/pymusepipe/
[21] https://gitlab.com/francbelf/ifu-pipeline
[22] Lee et al. (2022) used previous NGC 628 HST imaging obtained as part of the Legacy ExtraGalactic Ultraviolet Survey (Calzetti et al. 2015).

both the V and near-UV (NUV) filters and has been convolved to several physical resolutions (8, 16, 32, and 64 pc, respectively). Following Scheuermann et al. (2023), we used the NUV-selected, 32 pc catalogs.

3. KCWI Data Reduction

The KCWI observations were reduced using the Version 1.0.1 Python implementation of the KCWI Data Extraction and Reduction Pipeline (KDRP).[23] It was built using the Keck Data Reduction Pipeline Framework package[24] and is a port of the initial IDL reduction pipeline[25] (Morrissey et al. 2018). The pipeline performs basic CCD reduction including bias and overscan subtraction, gain correction, cosmic-ray removal, dark and scattered light subtraction, and a flat-field correction.

Following these basic reductions, the KDRP used the continuum bar and thorium/argon arc lamp images to generate geometric and wavelength solutions to convert each 2D science image into a spectral data cube. The accuracy of the wavelength solutions was similar across all of the observation nights. The average rms for the derived wavelength solutions was 0.1 Å.

We derived an inverse sensitivity curve to flux calibrate each data cube from standard star observations. The measured standard deviation between all of the derived inverse sensitivity curves was ∼9% at $\lambda = 4600$ Å. The maximum standard deviation within the wavelength range containing the lines used in this analysis is ∼11%. Details of each standard star observation can be found in Table 7 of Appendix A. After flux calibration, each data cube was corrected for differential atmospheric refraction.

Because the instrument FOV is much smaller than each galaxy, our images contained no sky pixels. To perform sky subtraction, we observed dedicated sky positions interspersed between science observations. We assigned the sky frame closest in time to each science observation to be used for sky subtraction according to the instructions in the KDRP documentation.[26] The KDRP then performed sky subtraction using our preferred frames. The sky in all pixels was averaged together and scaled by the ratio of science-to-sky exposure time to estimate the sky observed in the "on" position. The final data products output by the pipeline include flux-calibrated science and 1σ uncertainty cubes, as well as a bad-pixel mask cube.

3.1. Image Reprojection

Next, we constructed mosaics from the individual KCWI pointing data cubes. The steps involved included image registration, matching the flux calibration to MUSE, and image coaddition. We also compared the absolute flux calibration of the final KCWI mosaics to MUSE and the Sloan Digital Sky Survey (SDSS).

The data cubes output by the KDRP have rectangular pixels with a pixel scale of $1\farcs35 \times 0\farcs29$. We reprojected the cubes onto a square pixel grid using the astronomical mosaic software `Montage`.[27] Prior to running `Montage`, we converted the KCWI data to surface brightness units (erg s^{-1} cm^{-2} Å^{-1} sr^{-1}) by dividing the flux per pixel by the pixel solid angle in steradians. The reprojected images have a final square pixel grid with a uniform pixel scale of $0\farcs29 \times 0\farcs29$. We validated the flux conservation in our data before and after reprojection.

3.2. Image Registration

To coadd each galaxy's set of cubes into a spectral mosaic, we placed each cube onto a common world coordinate system (WCS). It is typical to perform image registration by matching the location of foreground stars or background galaxies to known positions found in catalogs. However, in our case, most individual fields did not contain a sufficient number of bright point sources. Instead, we performed image registration by maximizing the cross-correlation between individual KCWI fields and overlapping MUSE data in order to match the KCWI pointing astrometry to MUSE. The astrometry of the MUSE galaxy mosaics was validated against wide-field broadband imaging and stellar positions from the Gaia DR1 as described in Emsellem et al. (2022). The MUSE astrometry, when compared to broadband imaging, exhibited better than 100 mas rms. in both R.A. and decl.

To cross-correlate KCWI and MUSE, we created synthetic photometry (P_S) images from spectral regions where the wavelength coverage of KCWI overlaps with that of MUSE. Because there is some saturation in Hβ and [O III] at the brightest locations in the KCWI data, we masked out those lines in both cubes to avoid any issues with the comparison between the two data cubes.

In order to determine the optimal astrometric shifts to apply to each KCWI science frame, we utilized a two-step grid search operation, first shifting in 1 pixel (or $0\farcs29$) steps ±17 pixels (or $5''$) from the center of the KCWI pointing in order to find the optimal R.A. and decl. offsets, which maximize the correlation of the KCWI and corresponding MUSE P_S images. After locating first-pass shifts, we performed a secondary grid search using finer 0.5 pixel increments over a smaller range ($\pm1''$ from the image center). The 0.5 pixel sampling corresponds to $0\farcs145$, which is less than the MUSE pixel scale of $0\farcs20$ but also corresponds to 1/10th the typical KCWI FWHM, which is equal to $1\farcs2$. Across the galaxy sample, the final offsets correspond to correlation coefficients >0.9 between KCWI and MUSE.

3.3. Matching the MUSE Flux Calibration

In order to correct for any additive and/or multiplicative offsets between the MUSE and KCWI flux calibrations, we compared the surface brightness (SB) calculated in apertures in overlapping position and wavelength. To do this, we made use of the P_S images, described in Section 3.2, and measured the surface brightness inside a number of $3''$ radius apertures located at randomly drawn positions inside the combined KCWI and MUSE coverage. The aperture size was chosen to be large enough to minimize effects arising from the different PSFs of KCWI and MUSE. We determined the best-fit line to the measured SB_{KCWI} versus SB_{MUSE} relationship, where the slope, m, and y-intercept, b, reflect the multiplicative and additive offset between the KCWI and MUSE flux calibration. We applied the correction by multiplying the KCWI data cubes by m and adding b to the full spectrum in each pixel. The average multiplicative and additive offsets were $m = 1.03 \pm 0.02$ and $b = -7.6 \pm 1.7 \times 10^{-20}$ erg s^{-1} cm^{-2} Å^{-1}. This ∼3% deviation from a 1-1 slope

[23] KCWI DRP-Python (https://github.com/Keck-DataReductionPipelines/KCWI_DRP).
[24] KeckDRPFramework (https://github.com/Keck-DataReductionPipelines/KeckDRPFramework).
[25] KCWI DRP-IDL (https://github.com/Keck-DataReductionPipelines/KCWIDRP).
[26] https://kcwi-drp.readthedocs.io/en/latest/sky_subtraction.html
[27] See http://montage.ipac.caltech.edu/.

and the low level of additive offset show that the calibrations were already in good agreement.

3.4. PSF of Individual KCWI Fields

Because the MUSE mosaics have been homogenized to a uniform Gaussian PSF, we have an image with a known (parameterized) PSF. This is advantageous, as we can directly measure the KCWI PSF per pointing using cross-convolution, following the steps outlined in Emsellem et al. (2022). We briefly summarize the procedure here. (1) We produced P_S images of both the MUSE mosaic and the individual KCWI pointings. (2) We reprojected the MUSE cutout onto the KCWI $0\farcs29 \times 0\farcs29$ pixel grid. (3) We convolved the KCWI pointing with a 2D Gaussian kernel with PSF equal to the reference MUSE PSF. (4) In an iterative manner, the reference MUSE image is then convolved with a 2D Gaussian kernel, PSF_k, where the PSF_k represents the KCWI pointing PSF, which is a free parameter. We then varied the FWHM of this kernel until we maximized the correlation between the KCWI pointing and the reference MUSE image. For the set of images observed for each galaxy, we present the average and standard deviation of the measured PSFs in Table 1. The average PSF across the galaxy sample is $1\farcs4 \pm 0\farcs2$, which is consistent with the PSFs measured using the Standard Star observations presented in Appendix A. We chose not to homogenize the PSF of the KCWI data. To do so would mean convolving the KCWI data to the largest observed PSF. In turn, this would increase the mismatch in resolution between KCWI and MUSE as well as lead to larger H II region boundaries. The larger regions have higher susceptibility to contamination from the diffuse ionized gas.

3.5. Image Coaddition

After the KCWI data cubes had been aligned and flux calibrated to match the MUSE mosaics, the KCWI data cubes were coadded to create KCWI galaxy mosaics. The image coaddition was performed with `Montage`. The `mAddCube` call to `Montage` initiates the coaddition. The coaddition is performed by stacking the aligned images, according to the output WCS determined by `Montage`, and then taking the average value between any overlapping pixels. Pseudo g-band images for the final mosaics of each galaxy are shown in Figure 1.

3.6. Absolute Calibration of KCWI Compared to MUSE

We assessed the absolute calibration of the coadded KCWI mosaics by comparing the SBs between the KCWI and MUSE mosaics. Comparisons of the MUSE mosaics with SDSS imaging in the r band described in Emsellem et al. (2022) showed that the MUSE absolute flux calibration is consistent with SDSS calibration within the instrument uncertainty of 0.06 mag (Padmanabhan et al. 2008). We calculated the SB inside $r = 3''$ apertures, randomly placed in the KCWI coverage. The SB offsets between the KCWI and MUSE mosaics are shown in Figure 2. The resulting offsets, summarized in Table 2, reveal acceptable agreement between the MUSE and KCWI absolute calibration. The average percent SB offset with respect to the SDSS imaging, $\Delta\mathrm{SB}/\mathrm{SB}_{\mathrm{SDSS}}$, is between -1.1% and 0.7% with a median value across all galaxies of $-0.1\% \pm 4\%$.

3.7. Absolute Calibration of KCWI Compared to SDSS

We have shown agreement between KCWI and MUSE, but this comparison is only an assessment of the flux calibration in the overlapping wavelength range of KCWI and MUSE. To assess the absolute flux calibration across a wider wavelength range, we compared synthetic g-band images of the KCWI mosaics to SDSS (Abazajian et al. 2003) images of the same galaxies. Only four galaxies with KCWI mosaics have SDSS imaging: NGC 628, NGC 1087, NGC 3627, and NGC 5068. We constructed synthetic g-band images of these galaxies by convolving the spectrum in each pixel, $F_\lambda(x, y)$, with the g-band transmission curve, $T_g(\lambda)$, according to the following equation:

$$F_g(x, y) = \frac{\int F_\lambda(x, y) T_g(\lambda) d\lambda}{\int T_g(\lambda) d\lambda}. \quad (1)$$

The SDSS imaging is presented in units of *nanomaggies* or $f_\nu = 3.631 \times 10^{-6}$ Jy. To compare with the KCWI data, with native units of flux density, f_λ, we converted to flux density with the following expression (Tokunaga & Vacca 2005):

$$f_\lambda = \frac{c}{\lambda_p^2} f_\nu, \quad (2)$$

where λ_p is the pivot wavelength of the bandpass. The pivot wavelength for the g-band filter is $\lambda_p = 4702$ Å. The surface brightnesses for both KCWI and SDSS are measured inside $3''$ radius apertures. The mean and 1σ scatter of the measured surface brightnesses are shown in Figure 3. We found overall agreement of the absolute calibration between KCWI and SDSS for the four galaxies. Summarized in Table 2, the median offset across the sample galaxies, $\Delta\mathrm{SB}/\mathrm{SB}_{\mathrm{SDSS}}$, ranges between -1.0% and 3.0% and exhibits scatter between 3% and 10%. The source of the largest scatter is from the northernmost observation of NGC 628. In spite of the quality of this KCWI field, we find that this field contains a single H II region, and as shown in Figure 27 of Appendix C, it contains detectable auroral and nebular emission from ions only within the MUSE spectrum. Because of this, including this KCWI field will have no negative impact on the overall analysis. The median SB offset across all galaxies is $1\% \pm 7\%$, which suggests that the KCWI calibration is in good agreement with SDSS.

4. H II Region Catalog

In order to assess the emission-line properties of H II regions, we determine the H II region location and boundaries using Hβ maps constructed from the KCWI spectral data cubes and the image-segmentation software `HIIphot` (Thilker et al. 2000). Although H II region masks have previously been constructed from the MUSE Hα maps for these galaxies (Kreckel et al. 2019; Santoro et al. 2022; Congiu et al. 2023; Groves et al. 2023), the MUSE angular resolution is higher than that of KCWI. Because of this, the H II region boundaries derived from MUSE may not fully encapsulate the spatial extent of the H II regions observed using KCWI. Furthermore, simply convolving or reprojecting the MUSE H II masks to the KCWI resolution or grid would introduce uncertainty on the boundaries for tightly spaced H II regions. We therefore perform H II region identification directly on the KCWI data.

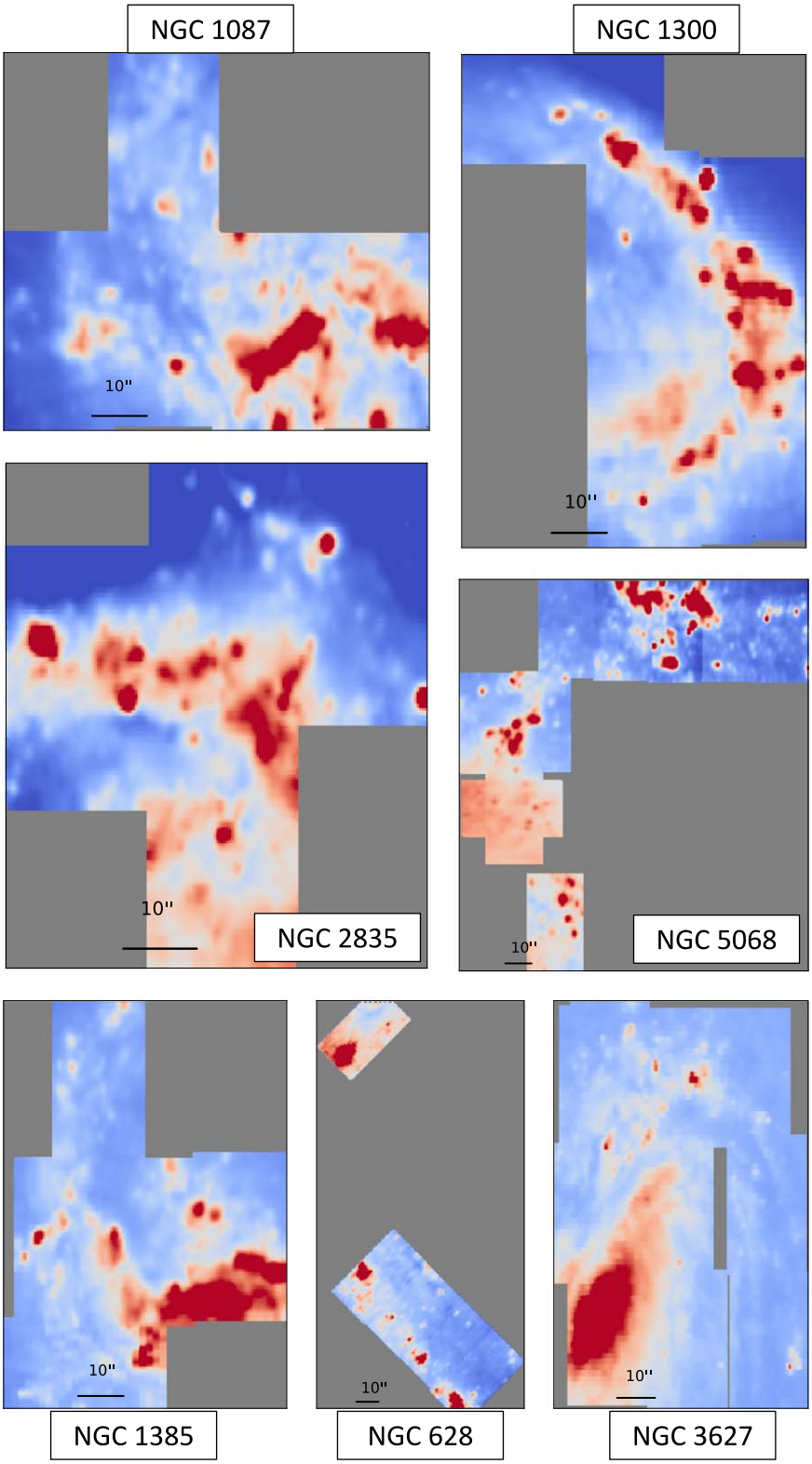

Figure 1. Pseudo *g*-band images of the KCWI mosaics. A 10″ scale bar is shown in the bottom of each image. Images are oriented to have north pointing upward.

4.1. Construction of Hβ Maps

Hβ is the brightest H I recombination line observed by KCWI, and maps of this emission for the galaxies will be used to define our H II regions. The continuum near and underlying the Hβ emission must be removed in order to accurately map its emission. To remove the continuum, we used `LZIFU`, an emission-line-fitting code designed specifically for use with IFUs (Ho et al. 2016). `LZIFU` implements and streamlines the penalized pixel-fitting software (`PPXF`; Cappellari & Emsellem 2004; Cappellari 2017) for using `PPXF` on IFU emission-line maps. To fit the continuum of the input spectrum, `LZIFU` matches a series of input single-metallicity, $-1.31 < [Z/H]$

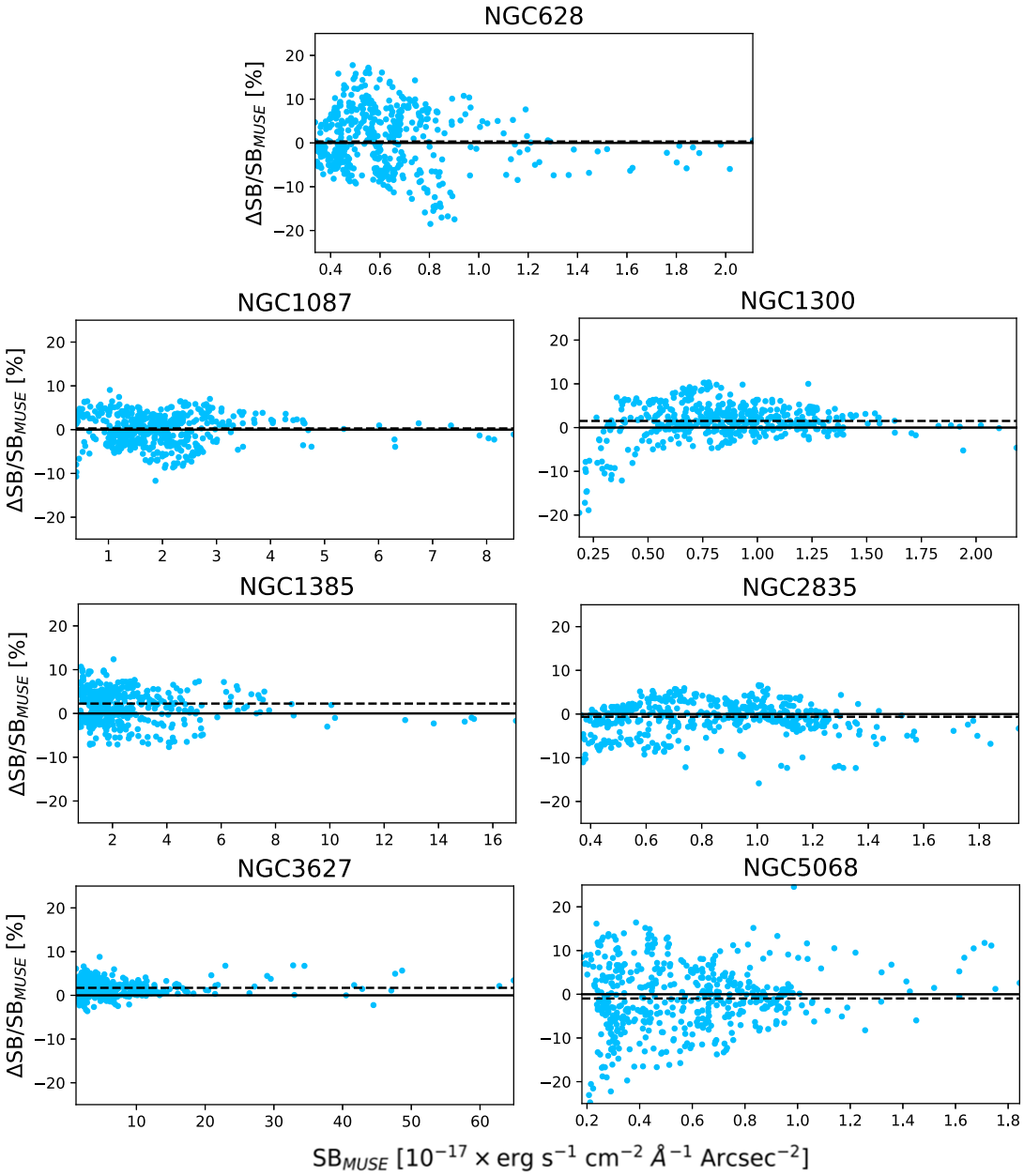

Figure 2. Comparison of P_S image surface brightness measured in $r = 3''$ apertures from synthetic KCWI and MUSE P_S mosaics of the seven galaxies. In each panel, we show the fractional SB differences between KCWI and MUSE vs. the SB of MUSE. The median fractional offset (black dashed) is shown relative to the zero line (black solid). Across all galaxies, the median offset is $\sim -0.1\%$.

< 0.22, stellar population models (Vazdekis et al. 2010; MILES) that have been redshifted and convolved to match the input spectrum PSF. `LZIFU` fits Gaussian models at the location of emission lines. In the output Hβ map, pixels with weak or no Hβ can contain "NaN" values, which can be problematic for `HIIphot`. To avoid these artifacts, we subtract the stellar continuum from each pixel's spectrum and construct the final Hβ maps by integrating the continuum-subtracted spectra between 4856 and 4876 Å. The final maps are suitable for H II region identification using `HIIphot`.

4.2. H II Region Identification

`HIIphot` was designed to identify H II regions and complexes (unresolved or blended H II regions) while also minimizing the inclusion of surrounding diffuse ionized gas (or DIG). `HIIphot` works by first defining "seeds" at the location of peak emission in Hβ (or Hα), then iteratively grows each "seed" and terminates only when the gradient of the Hβ (or Hα) surface brightness distribution matches a termination value, in mandatory units of emission measure (EM), set by the user. The gradient of the surface brightness distribution is a more robust method of stopping uncontrolled growth at lower S/N compared to using only the average local background level. For each galaxy, we apply the same termination gradient, $\Delta = 5$ EM pc^{-1} or $2.43 \times$erg s^{-1} arcsec^{-2} pc^{-1}, as the recent PHANGS-MUSE work by Santoro et al. (2022).

`HIIphot` uses the PSF to convolve the input Hβ map to different spatial scales to identify seeds. Using a constant PSF for all galaxies can potentially miss valid regions or generate nonphysical regions. The PSF of the input Hβ emission map is

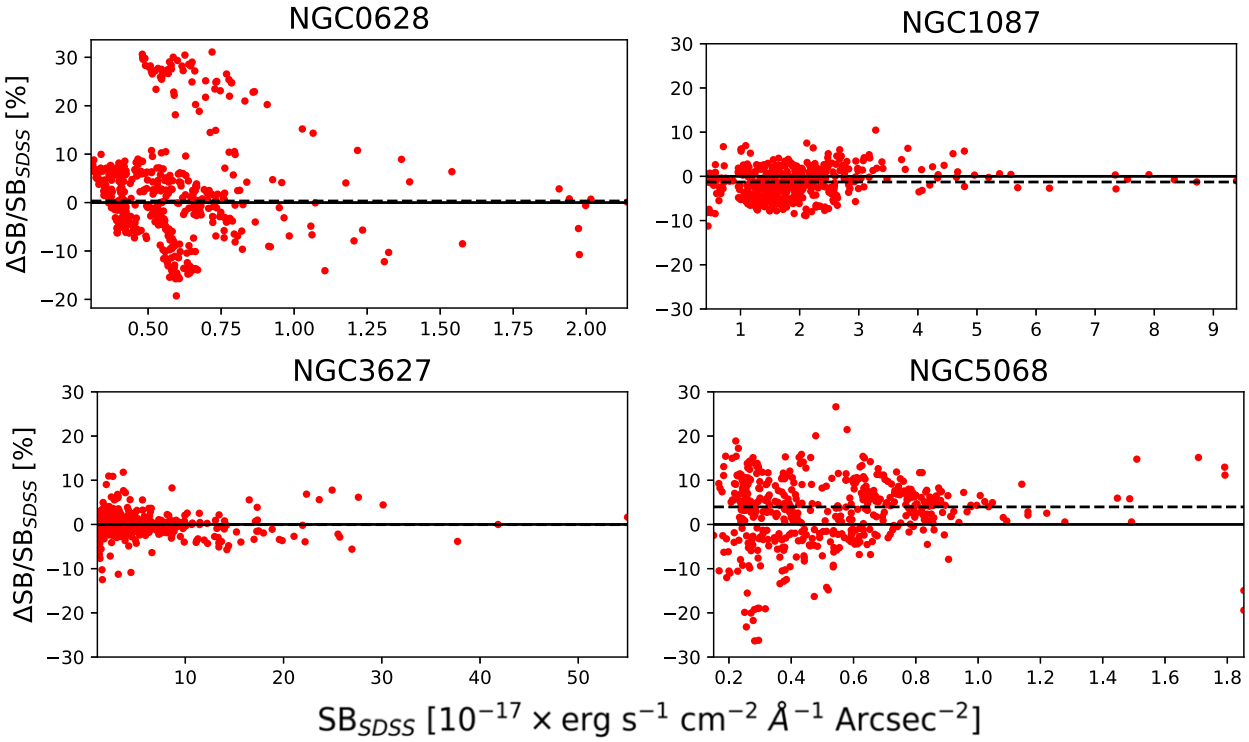

Figure 3. Comparison of g-band surface brightness measured in $r = 3''$ apertures from synthetic KCWI g-band mosaics and SDSS imaging for the four KCWI galaxies with available SDSS data. The surface brightness offset between KCWI and SDSS is shown vs. the SDSS g-band surface brightness. The median offset (black dashed) is shown relative to the zero line (solid black). Across the sample, the offset between the KCWI and SDSS surface brightness is ∼1%.

Table 2
Flux Calibration Comparisons between KCWI, SDSS, and MUSE

Name	$\mu(\Delta SB)$[a] (%)	$\sigma(\Delta SB)$[b] (%)	$\mu(\Delta SB_g)$[c] (%)	$\sigma(\Delta SB_g)$[d] (%)
NGC 628	0.3	6.0	0.3	10.0 [e]
NGC 1087	0.5	3.6	−1.0	3.4
NGC 1300	1.5	4.0	⋯	⋯
NGC 1385	−0.6	4.3	⋯	⋯
NGC 2835	−0.4	3.6	⋯	⋯
NGC 3627	1.7	1.6	−0.05	2.6
NGC 5068	0.3	6.7	2.9	8.4

Notes.
[a] The median fractional surface brightness offset between KCWI and MUSE in percent.
[b] The standard deviation of the fractional surface brightness offset between KCWI and MUSE in percent.
[c] The median g-band surface brightness offset between KCWI and SDSS.
[d] The standard deviation of g-band surface brightness offset between KCWI and SDSS.
[e] Removing the problematic field, discussed in Section 3.7, reduces this standard deviation to 7%, which is comparable to those of the other galaxies.

required by `HIIphot`. For each galaxy mosaic, we used the average PSF from its KCWI pointings (see Table 6 in Appendix A) as the input for `HIIphot`. As shown in Figure 4, the resulting 2D mask returned by `HIIphot` contains H II regions with smooth and reasonable boundaries, as judged via the distinction between clearly separated H II regions, as well as the minimization of spurious small and pixelated regions or runaway growth. In total, `HIIphot` identifies ∼688 H II regions or complexes across all of the KCWI mosaics. This number is smaller than the 2169 potential H II regions identified for the Nebular catalog (Kreckel et al. 2019; Santoro et al. 2022; Groves et al. 2023), as well as the 2124 potential H II regions from Congiu et al. (2023), inside the same KCWI footprints. This is largely due to the differences in angular resolution between KCWI and MUSE, as well as the threefold decrease in strength of Hβ emission relative to Hα. In Figure 20 of Appendix C, we show histograms of the Hβ luminosity and radii for KCWI and Nebular catalog regions as well as comparisons of the spatial masks in Figures 21–27 of Appendix C. Additionally, we also present in Table 8 of Appendix C the number of regions detected per galaxy.

4.3. Generation of Integrated H II Region Spectra

The KCWI H II region masks, produced by `HIIphot`, are used to isolate and sum the spectra in pixels belonging to each H II region, resulting in an integrated H II region spectrum. To produce a matching MUSE H II region mask, we transformed the H II regions coordinates/boundaries from the KCWI pixel grid onto the MUSE pixel grid. These are then used to construct MUSE-integrated spectra for each H II region. The KCWI and MUSE H II region spectra for a single H II region, with the full set of auroral lines highlighted, is shown in Figure 5.

We also produce integrated variance spectra for each H II region. The variance spectra for both KCWI and MUSE H II regions are constructed by propagating the pipeline-produced variance data cubes for pixels contained within each H II region boundary. In the case of MUSE, the data cubes have undergone an additional convolution process in order to generate mosaics with uniform PSF, which introduces a correlation between

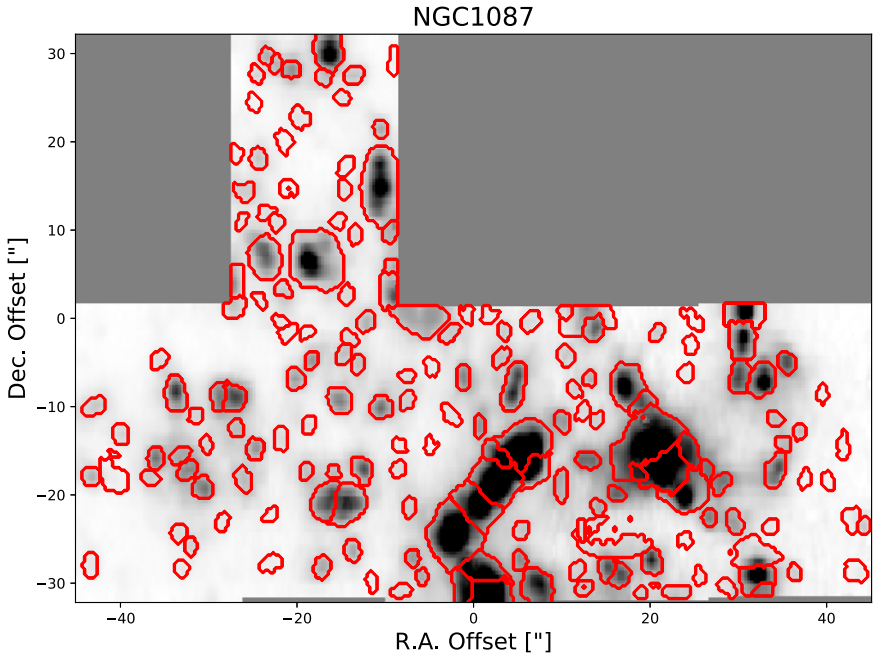

Figure 4. Region boundaries returned by `HIIPhot`. Pixels within the (red) boundaries are identified as corresponding to a potential H II region. The boundaries for the remaining sample galaxies are shown in Appendix C. The R.A. and decl. offset are centered on the R.A. and decl. coordinates $02^{h}\,46^{m}.0\,25^{s}.53$, $-00°\,29'\,38''.8$.

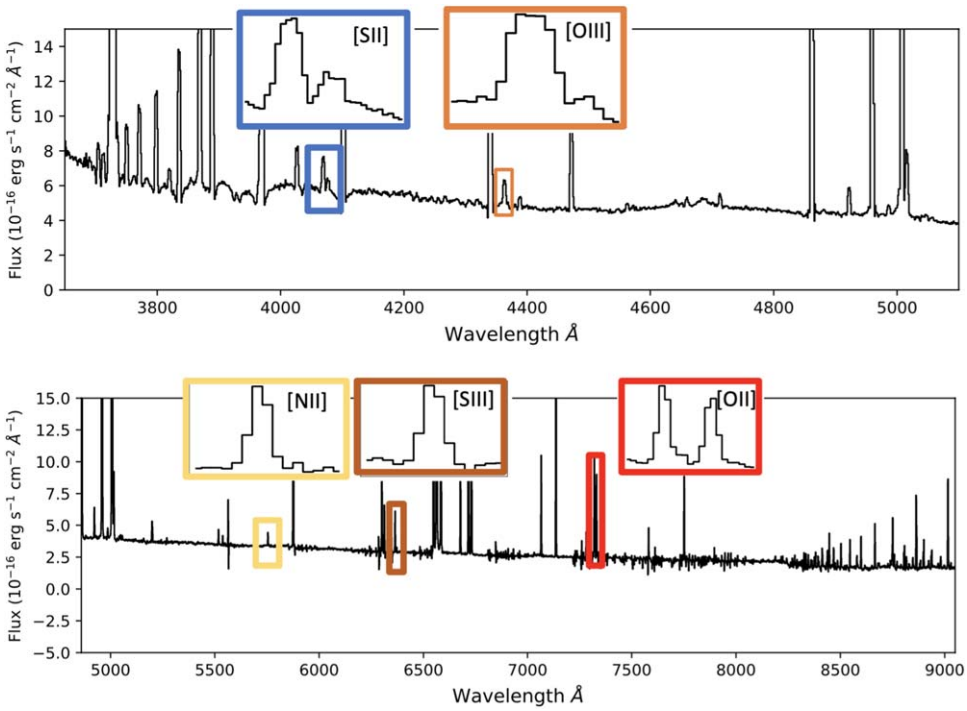

Figure 5. A KCWI (shown in the top panel) and a MUSE (shown in the bottom panel) H II region spectrum. Example spectrum for an H II region in NGC 5068. The full wavelength range afforded by combining both KCWI and MUSE captures the full set of optical auroral lines: [S II]$\lambda\lambda$4068, 4078, [O III]λ4363, [N II]λ5756, [S III]λ6312, and [O II]$\lambda\lambda$7320, 7330, which are identified with zoomed-in insets.

neighboring pixels (Emsellem et al. 2022). Because of the additional convolution, we generated the MUSE variance spectra, assuming fully correlated conditions, by adding the pixel variance spectra linearly (Taylor 1997).

We verify this choice by comparing the median standard deviation of the propagated MUSE variance spectra, $\sigma_{\rm propagated}$, to the median standard deviation of the H II region spectrum, $\sigma_{\rm measured}$, in the emission-line-free wavelength range 5400–5450 Å. We measured an average ratio between the propagated and measured error of $\sigma_{\rm measured}/\sigma_{\rm propagated} = 1.1 \pm 0.2$, implying that we are appropriately propagating the error. We also perform a similar comparison for KCWI, and find agreement, $\sigma_{\rm measured}/\sigma_{\rm propagated} = 1.9 \pm 0.5$, between the measured and propagated error using uncorrelated pixel error propagation. To

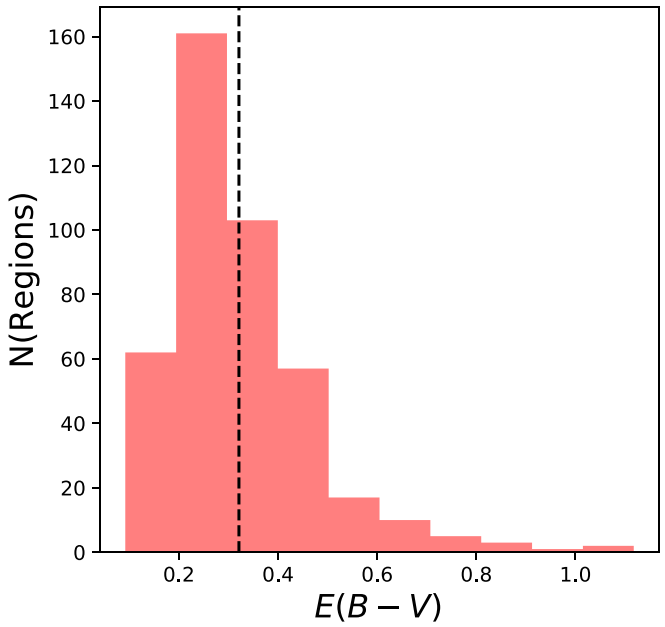

Figure 6. Histogram of derived extinction, $E(B-V)$. We measured $E(B-V)$ using the O'Donnell (1994) extinction law for the regions identified by HIIPhot. A (black dashed) line is located at the mean $E(B-V)$, 0.30 ± 0.14 mag.

generate the appropriate variance, we propagated the error using uncorrelated, for KCWI, and fully correlated error, for MUSE, propagation methods.

4.4. H II Region Stellar and Emission-line Fitting

We modeled the stellar continuum and emission lines of the integrated H II region spectra using the general PPXF toolkit. Although the LZIFU implementation of PPXF allowed for the streamlined, full-data-cube fitting of the KCWI Hβ emission-line map, the general PPXF toolkit offers more flexibility in the input-fitting parameters. For example, we can input a wavelength-dependent line-spread function as well as fix the kinematics between emission lines of doublets and lines with similar levels of ionization. We followed Emsellem et al. (2022) and fit the emission lines simultaneously with the stellar continuum. This particular fitting recipe was chosen to mirror the philosophy of the Mapping Nearby Galaxies at APO Data Analysis Pipeline (MaNGA DAP; Law et al. 2016; Emsellem et al. 2022) and is suggested to mitigate the biases on emission-line fluxes introduced by the masking of stellar absorption features around affected lines (Sarzi et al. 2006; Oh et al. 2011; Belfiore et al. 2019). PPXF robustly fits the stellar continuum by matching a set of templates to the observed H II region spectrum. The templates originate from the E-MILES library of simple stellar population (SSP) models (Vazdekis et al. 2016). The SSP ages were between 0.15 and 13.5 Gyr. Each age bin contained SSPs with the following metallicities: $[Z/H] = [-1.49, -0.96, -0.35, 0.06, 0.26, 0.4]$. Typically, PPXF convolves the SSP templates with a Gaussian model accounting for the spectral resolution of the input spectrum and the stellar velocity dispersion. However, because the KCWI line profile deviates significantly from a Gaussian (see Appendix B), we convolved the PPXF templates with a four-moment Gauss–Hermite function while fitting KCWI emission lines. We constrained the fits of h_4 and h_3 in the Gauss–Hermite functions to values listed in Appendix B. We performed the PPXF fitting of the KCWI H II region spectra independently from the MUSE H II region spectra. The fractional difference between the H II region Hβ flux for KCWI and MUSE is $-2.3\% \pm 7.5\%$.

We obtained errors on the emission-line fluxes from the output of PPXF. The output errors are considered reliable if the PPXF-derived reduced $\chi^2 \approx 1$. Together, the resulting fits for both the KCWI and MUSE have an average reduced $\chi^2_{\rm reduced} \approx 2.0$, indicative that the input variance spectra are underestimated. We obtained a better estimate of the errors by rescaling the returned errors, for each fit to KCWI and MUSE spectra, by a factor of $\sqrt{\chi^2_{\rm reduced}}$ (Cappellari & Emsellem 2004; Cappellari 2017; Emsellem et al. 2022).

4.5. Dust Correction

We derive the V-band extinction (A_V) for each H II region using the Balmer decrement. To evaluate this decrement while also taking into account the errors on the measured Hα and Hβ emission, we construct a distribution of the MUSE Hα/Hβ ratios by sampling the error for each line. Next, using PyNeb, we calculate the extinction by comparing the average of the Hα/Hβ distribution to the theoretical value assuming the Case B recombination conditions $n_e = 10^3\,{\rm cm}^{-3}$ and $T_e = 10^4\,{\rm K}$ (Storey & Hummer 1995). We explore how changing the assumed T_e could affect the derived A_V by sampling a range of temperatures between 5000 K and 1.5×10^4 K, and we find that the standard deviation of A_V for a fixed Balmer decrement is $\sim$0.06 mag. We apply the wavelength-dependent extinction correction assuming an O'Donnell (1994) extinction curve. We present a histogram of the derived $E(B-V)$ in Figure 6. The average $E(B-V)$ for the regions is 0.30 mag and corresponds to an $A_V \sim 0.9$ mag. We find a negligible difference when using KCWI Hβ in place of the MUSE Hβ flux. We should add that a recent investigation has shown that correcting, or not correcting, the Balmer lines for DIG contamination can impact the measured $E(B-V)$ (Congiu et al. 2023). For the range of $E(B-V)$ observed, a DIG-corrected $E(B-V)$ may return values of A_V 0.05–0.1 mag lower than presented here. We discuss the effects that under/overestimated extinction may have on the measured electron temperature in Section 7.1.1. Furthermore, given the good agreement between the integrated KCWI and MUSE H II region fluxes, we replace any saturated integrated H II region KCWI Hβ and [O III] fluxes with those measured from their integrated MUSE spectrum.

4.6. Diffuse Ionized Gas

Emission from Balmer transitions, [S II]$\lambda\lambda$6716, 6731, [N II] λ6584, and other lines originating from DIG surrounding the H II regions can contaminate the H II region emission-line fluxes of the same transitions. Measuring the DIG contribution to the H II region line flux is only beginning to be explored by IFU studies (see Belfiore et al. 2022; Congiu et al. 2023). In order to remove regions with a large degree of DIG contamination, we calculate the contrast between H II/DIG emission following the scheme outlined in Kreckel et al. (2022). First, we mask each H II region in the MUSE emission-line maps for Hα, Hβ, [S II], [N II], and [O I]. For each emission line, we place a $10'' \times 10''$ aperture around each H II region and measure the median DIG flux in pixels with S/N > 3 and Hα surface brightness $\log_{10}({\rm SB_{H\alpha}}/[{\rm erg\ s^{-1}\ kpc^{-2}}]) < 38$ (see Belfiore et al. 2022). Finally, we calculate the "integrated" DIG emission by multiplying the median DIG flux by the H II region size. For each DIG emission line, we calculate the percent contrast between the

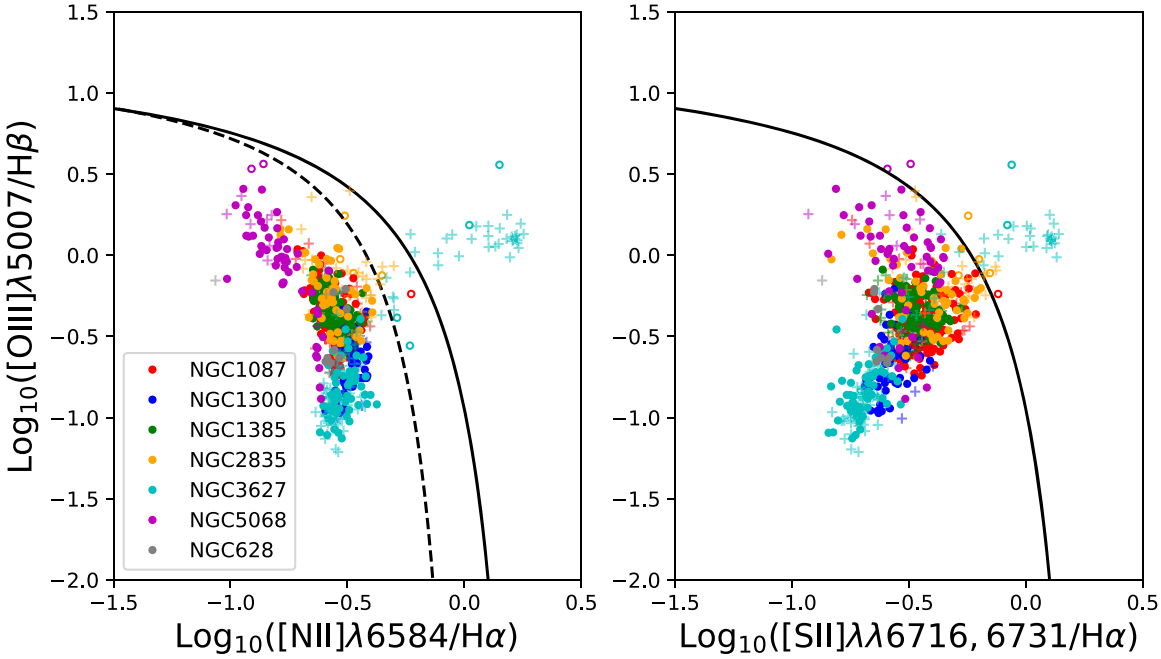

Figure 7. BPT diagrams showing [O III]/Hβ vs. [N II]/Hα, in the left panel, and [O III]/Hβ vs. [S II]/Hα ratios, in the right panel, for each region identified by `HIIphot`. Regions with emission-line ratios consistent with photoionization by stars are expected to populate the parameter space below the theoretical (solid black; Kewley et al. 2001) and empirical (dashed black; Kauffmann et al. 2003) classification lines. The H II regions are marked by filled markers. The regions above either of the classification lines are labeled with nonfilled markers and are rejected from the catalog. Regions marked by "+" symbols have been rejected by our other considered constraints.

measured H II region flux and DIG flux. If the contrast between the H II region flux and DIG flux of any low-ionization emission line is <50%, we exclude it from the sample.

4.7. Quality Assessment and Classification of Regions

The regions identified by `HIIphot` are potentially a mix of H II regions, planetary nebulae, supernova remnants, or low S/N in critical emission lines. We perform a set of cuts to reject non-H II regions and/or low-S/N spectra from the catalog of H II regions.

1. We exclude any H II region whose centroid coordinates are within 2″ from the edge of the mosaic. This step removes 86 H II regions.
2. We require the strong lines used for temperature determinations, namely Hβ, Hα, [O III]$\lambda\lambda$4959, 5007 [O II]λ3727, [N II]$\lambda\lambda$6548, 6584, [S III]λ9069, and [S II] $\lambda\lambda$6716, 6731, to be detected above a threshold of S/N > 5. This step cuts 72 H II regions from the sample.
3. Using the lines of Hβ, Hα, [O III], and [N II], we construct a Baldwin–Phillips–Terlevich (BPT; Baldwin et al. 1981) diagram. We require H II regions to be consistent with photoionization by massive stars. Therefore, we require them to fall below the empirical [O III]/Hβ versus [N II]/Hα (Kauffmann et al. 2003) and [O III]/Hβ versus [S II]/Hα (Kewley et al. 2001) lines. The BPT diagram showing the location of each H II region is shown in Figure 7. Out of the sample, 11 H II regions are above the empirical and theoretical line cutoffs and are removed.
4. We exclude H II regions that fail our DIG contrast check in Section 4.6. This step removes 98 H II regions.

The constraints together remove 267 out of the 688 detected H II regions, leaving 421 H II regions remaining for use in future analysis. For these 421 regions, comparisons of line ratios in Figure 7 to model classifications in Figure 3 of Congiu et al. (2023) suggest that this sample is consistent with their H II region classification. In order to compare the electron temperatures derived from the lines, which are critical for T_e–T_e comparisons, we also exclude regions with less than two significant (i.e., S/N > 3; see Section 5) detections in any auroral line. This cut removes 161 regions, leaving a final sample of 260 H II regions. We report in Table 8 of Appendix C the number of regions with at least two auroral lines for each galaxy.

5. Measurement of Auroral-line Emission

In order to robustly measure the flux and uncertainty for the faint, temperature-sensitive auroral lines from [N II]λ5756, [O II]$\lambda\lambda$7320, 7330, [S II]$\lambda\lambda$4069, 4076, [O III]λ4363, and [S III]λ6312, we implement a specific auroral-line-fitting scheme in place of `PPXF`. This is necessary because any under/oversubtraction of the continuum at the location of the faint auroral lines can bias the measured auroral-line flux.

The framework of the auroral-line fit is as follows. We first subtract the stellar continuum spectrum fitted by `PPXF`. This results in an H II region spectrum that contains only emission lines and residuals from the continuum subtraction. Next, we measure the standard deviation of the residuals, $\sigma_{\rm cont}$, in a region near the auroral line but also free of emission. We then perform a large number of fits to the auroral line, with random noise added to each wavelength bin, drawn from a normal distribution with standard deviation $\sigma_{\rm cont}$. In each trial, we fit a single Gaussian (or double, depending on the auroral line) plus a linear offset to the spectrum. The linear term is needed to correct for any residual continuum present in the continuum-subtracted spectrum. After completing the N trials, we calculate the average integrated line flux, $F_{\rm avg}$, and the standard

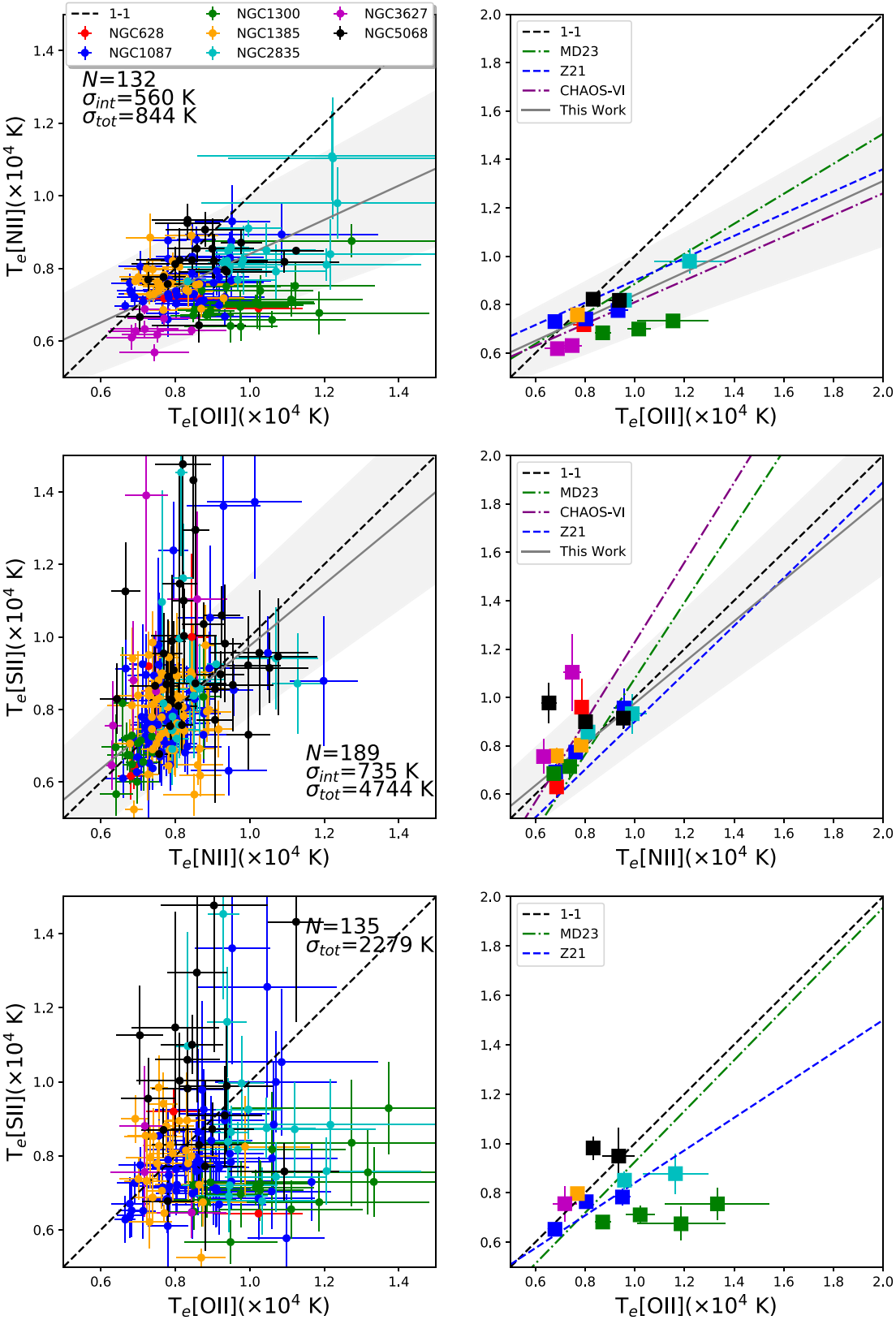

Figure 8. T_e–T_e relationships for the low-ionization zone temperatures measured from H II regions in nearby galaxies. The left panel in each row displays the individual temperatures and errors with each point colored according to the host galaxy. The right panel in each row shows the T_e–T_e relations for temperatures binned in steps of 2000 K in the x-axis, with a minimum of two H II regions per bin, for each galaxy, compared to T_e–T_e trend lines from Z21 (blue dash), CHAOS-VI (purple dotted–dashed), and MD23 (green dotted–dashed). To aid the eye, we include the 1-1 line (black dashed). For comparisons with p-value $< 10^{-3}$, we include the best-fit line (gray solid) and 1σ fit uncertainty (gray shaded).

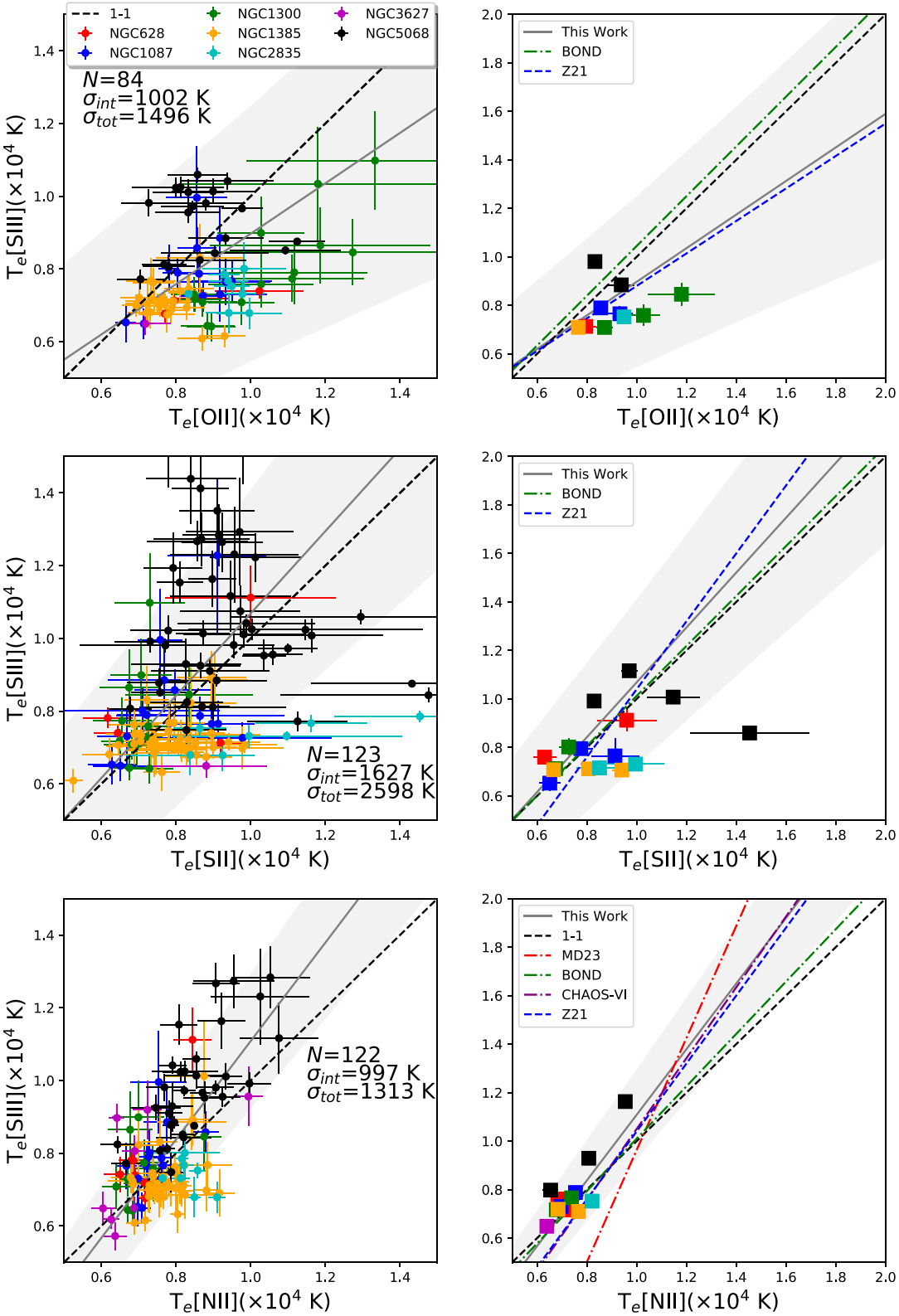

Figure 9. T_e–T_e relationships between the low- and intermediate-ionization zone temperatures measured from H II regions in nearby galaxies. The temperatures measured from H II regions in this work are color coded by host galaxy. The left panel in each row displays the individual temperatures and errors, with each point colored according to the host galaxy. The right panel in each row shows the T_e–T_e relations for temperatures binned in steps of 2000 K on the x-axis, with minimum 2 H II regions per bin, for each galaxy, compared to T_e–T_e trend lines from Z21 (blue dash), CHAOS-VI (purple dotted–dashed), BOND (green dotted–dashed), and MD23 (red dotted–dashed). To aid the eye, we include the 1-1 line (black dashed). For comparisons with p-value $< 10^{-3}$, we include the best-fit line (gray solid) and 1σ fit uncertainty (gray shaded).

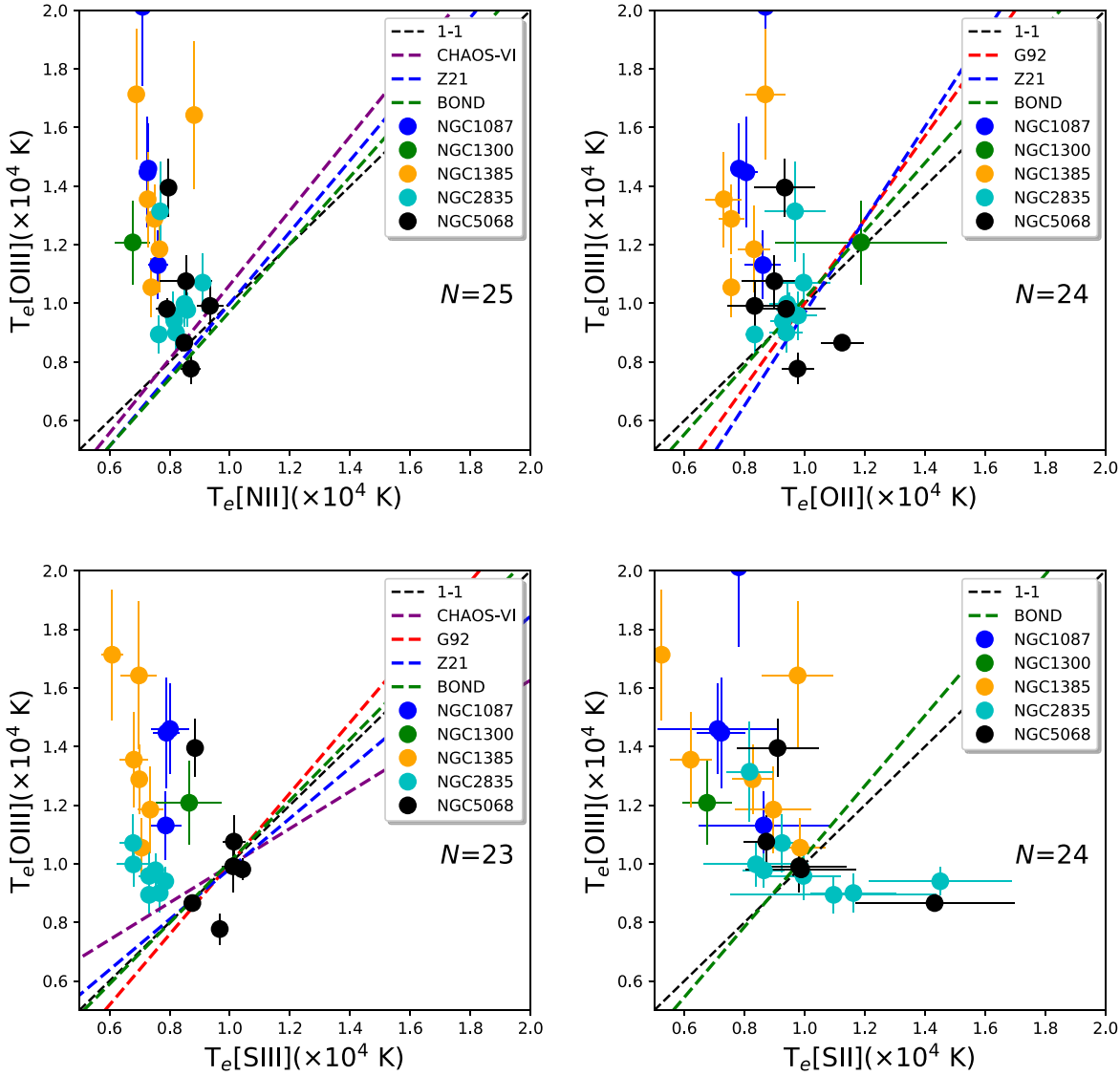

Figure 10. T_e–T_e relationships for the high-ionization zone. The temperatures measured from H II regions in this work are color coded by host galaxy. The blue dashed line shows the T_e–T_e relationships from Z21. The red dashed line shows trends from CHAOS-VI. The purple dashed and green dashed lines show trends from the photoionization models of G92 and BOND. To aid the eye, we also show the 1-1 line, in black, in each panel.

deviation of the measured fluxes, σ_{avg}. If S/N > 3, we consider the auroral line detected. In Figure 28 of Appendix D, we show the model fits and residuals for a region in NGC 5068.

Although this general process is performed for all of the auroral lines, the auroral line from [O III] is subject to additional constraints because emission from [O III]λ4363 can be blended with that from [Fe II]λ4360. This has been observed in both stacked galaxy and individual H II region spectra (Curti et al. 2017; Arellano-Córdova & Rodríguez 2020; Berg et al. 2020). The strength of the [Fe II]λ4360 emission has been observed to increase with the metallicity of the gas (Curti et al. 2017), although continuum-pumping fluorescence contributes strongly to its emissivity (Rodríguez 1999). [Fe II]λ4360 and [Fe II]λ4288 arise from the same atomic upper level, and their relative intensities are independent of the physical conditions of the gas and depend solely on the atomic transition probabilities. Because $I(\lambda4360)/I(\lambda4288) = 0.73$ (Mendoza et al. 2023), if [Fe II]λ4360 is detected, [Fe II]λ4288 should be present too.

To remove blending of the [O III]λ4363 line by [Fe II]λ4360, we use the fixed ratio, $I(\lambda4360)/I(\lambda4288) = 0.73$, to estimate the degree of contamination by measuring the strength of the brighter [Fe II]λ4288 emission. For each region, we first fit the [Fe II]λ4288 line using a single Gaussian plus a linear continuum model. The initial guesses for the line center and width are taken from the parameters of Hγ returned by the PPXF fits. In the case that the [Fe II]λ4288 is not detected above an S/N threshold of 3, we instead use the 3σ upper limit. We next fit [O III]λ4363 using a single Gaussian plus constant offset model. The initial guesses for the kinematics of [O III] λ4363 are taken from the PPXF fit of [O III]λ4958. After adding random noise, we generate a model for the [Fe II]λ4360 using the best-fit parameters and errors derived from the fit to [Fe II]λ4288, using the fixed $I(\lambda4360)/I(\lambda4288)$ ratio. After generating the [Fe II]λ4360 model, we subtract it from the trial spectrum and proceed to then fit for the emission-line flux originating from [O III]λ4363. We also note that, by performing the above fitting scheme on each region, we may be introducing a bias in the form of a systematic reduction of the [O III]λ4363 flux. However, this bias would favor systematically lower $T_{e,[O\ III]}$, and as shown in Section 7, we do not

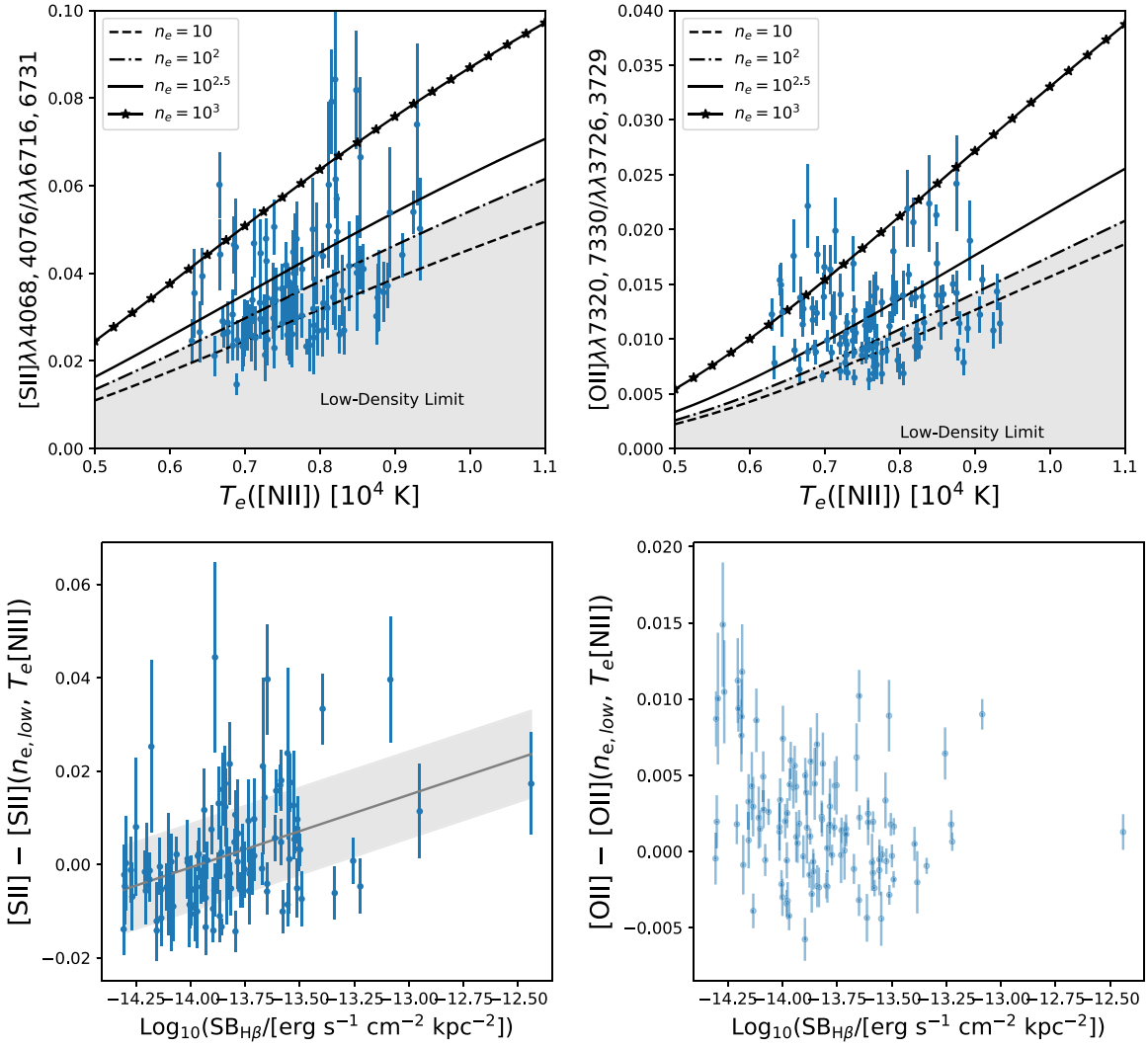

Figure 11. In the top panels, we show auroral-to-nebular line ratios measured from [S II] and [O II] against their measured $T_{e,[N\ II]}$. We assume equality between the low-ionization zone temperatures and overlay lines of predicted [S II] and [O II] auroral-to-nebular line ratios for fixed electron densities $n_e = 10$ cm^{-3}, $n_e = 10^2$ cm^{-3}, $10^{2.5}$ cm^{-3}, and 10^3 cm^{-3}, vs. $T_{e,[N\ II]}$. The gray shaded region in the top panels shows a regime with auroral-to-nebular line ratios for densities below the low-density limits for the [S II] and [O II] density diagnostics. In the bottom panels, we show the departure of the measured [S II] and [O II] auroral-to-nebular line ratios from the theoretical auroral-to-nebular line ratio predicted using $n_e = 100$ cm^{-3} and $T_{e,[N\ II]}$ against the Hβ surface brightness. In the bottom left [S II] panel, we show the best-fit line (gray solid) and 1σ fit uncertainty (gray shaded).

observe any behavior with $T_{e,[O\ III]}$ that would indicate the presence of such a systematic.

We detect emission from [Fe II]λ4288 in 30 H II regions: two of these are in regions with measurable [O III]λ4363. The low number of [Fe II]λ4288 detections suggests that the combination of high metallicity, needed for the presence of iron lines, and the exponential dampening of [O III]λ4363 makes the contamination of [O III]λ4363 by [Fe II]λ4360 a rare occurrence in spiral galaxies. From the nondetections, we determined that the 3σ upper limit on the [Fe II]λ4360 flux is 3.5×10^{-17} erg s^{-1} cm^{-2} pc^{-1}, which is $\sim$20% of the average [O III]λ4363 flux. We show in Figure 29 of Appendix D an example [O III]λ4363 fit that has had significant [Fe II]λ4360 contribution removed.

6. H II Region Nebular, Environmental, and Stellar Properties

We assess the ionized gas physical conditions—n_e, T_e, and ionization parameter U—of each H II region using a subset of the dust-corrected emission-line fluxes. We also measure a number of characteristics of the H II region's environment and local stellar population, as described below. The emission line fluxes, and all the derived properties, are presented in Table 9 of Appendix C.

6.1. Electron Density

Using `PyNeb`, we calculate the electron density n_e for each H II region using the [S II]$\lambda\lambda$6716, 6731 doublet. Based on our constraints discussed in Section 4.7, each H II region is guaranteed to have measured emission from this doublet at S/N > 5. The [O II]$\lambda\lambda$3726, 3729 doublet is also commonly used to estimate n_e. The atomic levels responsible for [S II] $\lambda\lambda$6716, 6731 and [O II]$\lambda\lambda$3726, 3729 both have critical densities, when collisional and radiative de-excitation are occurring at equal rates, that are on the order of 10^3 cm^{-3}. The critical densities, as well as other references for the atomic data used, are listed in Table 3. Both the [S II]$\lambda\lambda$6716, 6731 and [O II]$\lambda\lambda$3726, 3729 doublets are sensitive to densities 10^2 cm$^{-3} < n_e < 10^{3.5}$ cm^{-3}. However, in the KCWI

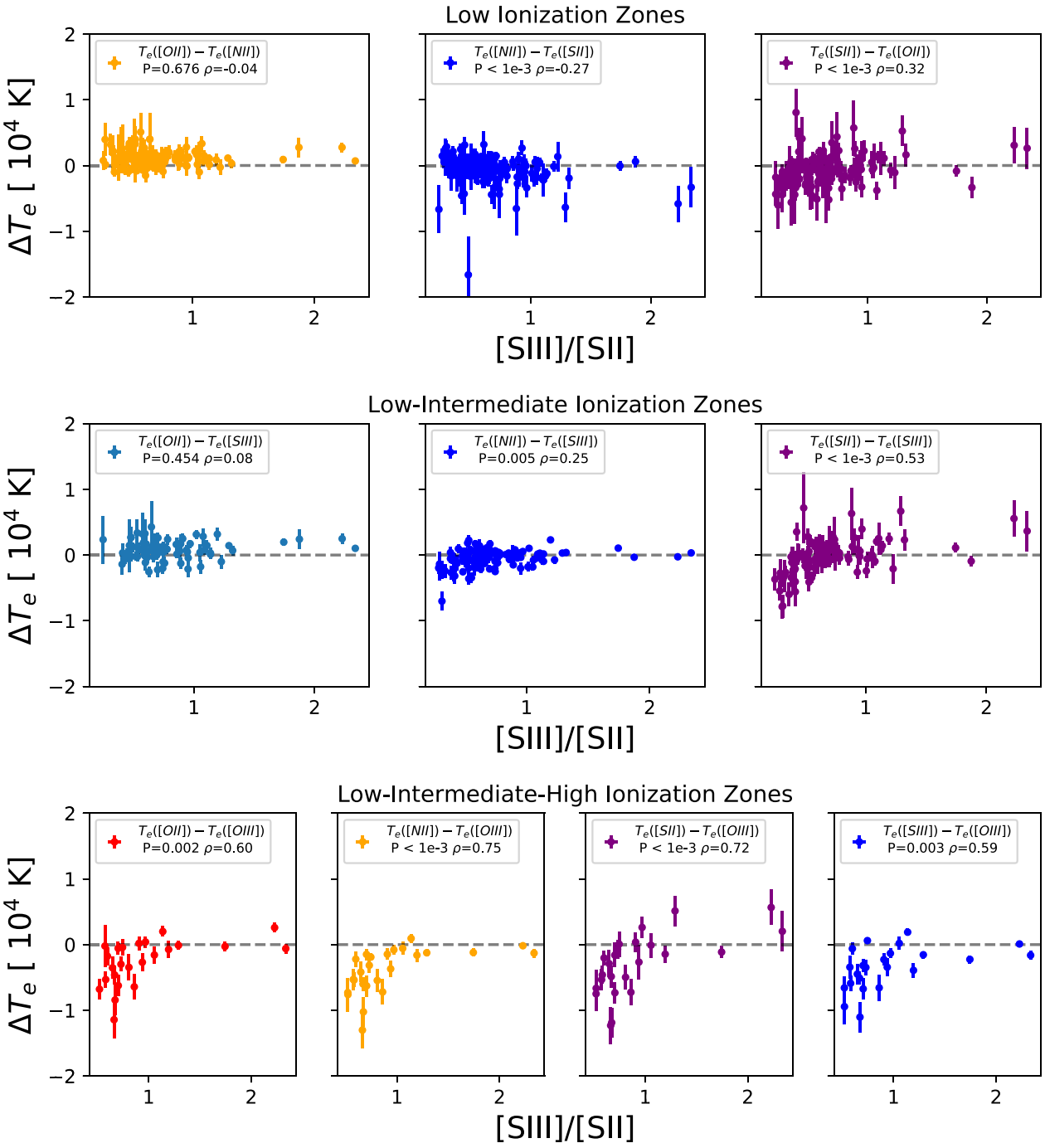

Figure 12. Electron temperature differences compared to the H II region ionization parameter, U, traced by [S III]/[S II]. Top: the values of ΔT_e between the low-ionization zone temperatures. Middle: the values of ΔT_e between the low- and intermediate-ionization zone temperatures. Bottom: the values of ΔT_e between the low-, intermediate-, and high-ionization zone temperatures. We observe significant correlations with U, traced by [S III]/[S II], between the low-ionization zone temperatures differences $\Delta(T_{e,[N\ II]}, T_{e,[S\ II]})$ and $\Delta(T_{e,[S\ II]}, T_{e,[O\ II]})$, between the low- and intermediate-ionization zones $\Delta(T_{e,[S\ II]}, T_{e,[S\ III]})$, and between the high-ionization zone $\Delta(T_{e,[N\ II]}, T_{e,[S\ III]})$ and $\Delta(T_{e,[S\ II]}, T_{e,[O\ III]})$.

measurements, the [O II]$\lambda\lambda$3726, 3729 doublet is unresolved, and therefore we do not use it to measure n_e. As shown in Figure 30 in Appendix E, with the exception of a handful of regions, the measured electron densities are in the low-density limit, $n_e < 100$ cm^{-3}.

6.2. H II Region Electron Temperatures

The auroral lines allow for the determination of the electron temperatures for the O^+, O^{2+}, N^+, S^+, and S^{2+} ions, or $T_{e,[O\ II]}$, $T_{e,[O\ III]}$, $T_{e,[N\ II]}$, $T_{e,[S\ II]}$, and $T_{e,[S\ III]}$, respectively. The temperatures are calculated via `PyNeb` using the collision strengths and transition probabilities, listed in Table 3, as well the measured upper limits of the electron density, n_e, to convert an auroral-to-nebular ratio to temperature. The critical densities of the requisite lines, see Table 3, used to estimate $T_{e,[O\ III]}$, $T_{e,[N\ II]}$, and $T_{e,[S\ III]}$ are high enough such that the auroral-to-nebular lines ratios are insensitive to a choice of $n_e < 10^4$ cm^{-3}. The density sensitivity in the lines used for $T_{e,[O\ II]}$ and $T_{e,[S\ II]}$

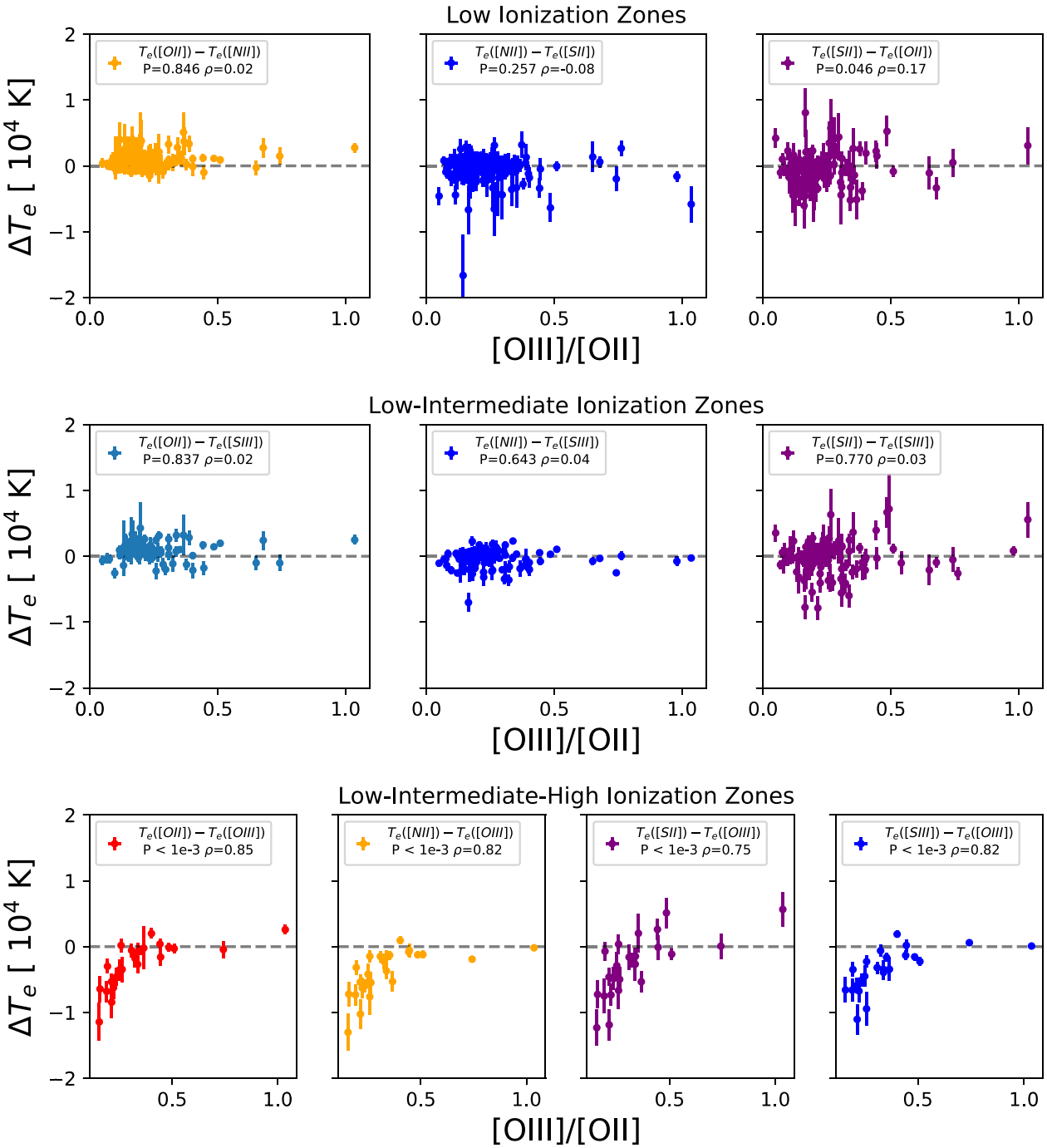

Figure 13. Electron temperature differences compared to the H II region ionization parameter, U, traced by [O III]/[O II]. The ionization zones depicted in each row follow those in Figure 12. We observe strong correlations between all of the ΔT_e involving $T_{e,[O\ III]}$. The correlations between the low- and intermediate-ionization zones and U, traced with [S III]/[S II] and shown in Figure 12, do not appear when tracing U with [O III]/[O II].

begins at smaller densities $n_e \approx 10^3$ cm^{-3} and is further discussed in Section 7.3. The uncertainty for each temperature measurement is the standard deviation of the distribution of temperatures constructed by Monte Carlo sampling of the error for each auroral and nebular line included in the temperature determination. We summarize the number of detections and median temperature for each ion in Table 4.

6.3. H II Region Ionization Parameters

The ionization parameter is an indicator of the strength of the ionizing radiation field. The Strömgren sphere descriptions of H II regions define the ionization parameter as $U = Q_0/(4\pi R^2 n_H c)$, where Q_0 is the emission rate of photons capable of ionizing hydrogen (i.e., with energy >13.6 eV), R is the radius of the ionized region, and n_H and c are the hydrogen density and speed of light. However, calculating the ionization parameter using this definition is difficult (Kreckel et al. 2019, 2022), as resolved studies show that H II regions exhibit a range of nonspherical morphologies and nonuniform densities (Wood & Churchwell 1989).

Instead, we trace the ionization parameter using both the [S III]/[S II] and [O III]/[O II] emission-line ratios.

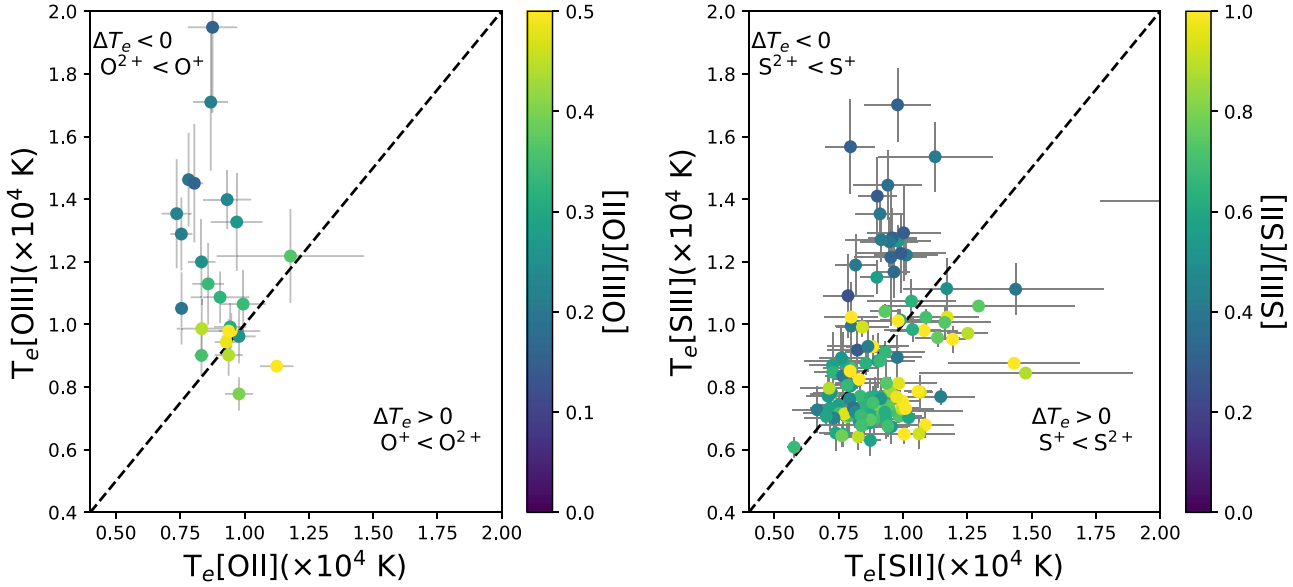

Figure 14. The T_e–T_e relation between (left) $T_{e,[O\ III]}$–$T_{e,[O\ II]}$ and (right) $T_{e,[S\ III]}$–$T_{e,[S\ II]}$ colored by the value of [O III]/[O II] and [S III]/[S II]. In both panels, the largest ratios of $T_{e,[X\ III]}/T_{e,[X\ II]}$, where X is either S or O, occur for the lowest values of ionization parameter, as indicated by the value of the line ratio, as expected according to the results of Yates et al. (2020).

Photoionization modeling has shown that both the [S III] $\lambda\lambda$9069, 9532/[S II]$\lambda\lambda$6716, 6731 and [O III]$\lambda\lambda$4959, 5007/[O II]$\lambda\lambda$3626, 3729 correlate with the ionization parameter, U (Dors et al. 2011). Although it has a positive correlation with the ionization parameter, the [O III]/[O II] also has a secondary dependence on metallicity, increasing with decreasing metallicity. [S III]/[S II] is not as sensitive to metallicity, making the ratio a more reliable tracer of the ionization parameter (Kewley & Dopita 2002). Differences between these diagnostics are discussed further in Section 7.3.1. While [S III]λ9532 is not observed with MUSE, we measure the [S III]λ9069 and assume the fixed theoretical line ratio of [S III]λ9532/λ9069 = 2.5 (Froese Fischer et al. 2006) in all calculations. Without observations of [S III]λ9532, we cannot use this theoretical ratio to assess any impact of atmospheric absorption. Despite this, and as discussed in Section 7.1.2, the low scatter between $T_{e,[N\ II]}$ and $T_{e,[S\ III]}$ suggests that the decrease in the [S III] λ9069 flux due to atmospheric absorption may be negligible.

6.4. ALMA-CO: Intensity, Peak Temperature, and Velocity Dispersion

Using the ALMA 12m+7m+TP data cubes, we calculate moment 0 and 2 (integrated intensity and velocity dispersion) for molecular gas near each H II region. Because molecular and ionized gas are not entirely cospatial at our resolution, it is necessary to make a selection to capture gas near the H II region. One possibility is to match H II regions to molecular clouds via a nearest-neighbor algorithm (Grasha et al. 2019; Zhang et al. 2021; Zakardjian et al. 2023). We instead choose to integrate the ALMA spectrum contained in the H II region boundaries in order to measure the properties of the molecular gas closest in projection to the ionized gas (i.e., in front, behind, or blended due to the resolution of KCWI) and likely affected by the radiative feedback. To measure the CO spectra, we reproject the H II region masks onto the grid of the ALMA data cubes and integrate the ALMA spectra for pixels located inside the footprint of each H II region.

From the ALMA spectrum, we then calculate the integrated intensity, I_{CO}, peak temperature, T_{peak}, and the velocity dispersion, $\sigma_{v,CO}$. In order to accurately measure these CO moments in the presence of noise, we construct a signal mask following the basic approach from Leroy et al. (2021a). To do this, we locate the velocity channel that contains the peak emission and construct an integration window around this channel by including velocity channels with signal above the 1σ noise.

As a check on our analysis of molecular gas, we compare the calculated velocity dispersions to those from a sample of nearest-neighbor-matched H II regions and GMCs constructed by Zakardjian et al. (2023). We find that our $\sigma_{v,CO}$ span a similar range, up to $\mathrm{Log}_{10}(\sigma_{v,CO}/[\mathrm{km\,s^{-1}}]) = 1.5$, with an average and standard deviation of $\mathrm{Log}_{10}(\sigma_{v,CO}/[\mathrm{km\,s^{-1}}]) = 0.88 \pm 0.25$; this is in line with the average from Zakardjian et al. (2023), which suggests that this method of extracting and measuring the CO properties is reasonable.

6.5. H II Region Compact Clusters and Associations

In order to test for correlations between the young stellar populations that power H II regions and their electron temperatures, we compile the stellar masses and ages of compact clusters and multiscale stellar associations within our KCWI H II regions using results from HST observations.

We match the HST clusters to H II regions with two or more auroral lines by simply selecting all of the clusters whose on-sky coordinates fall inside any H II region's spatial footprint. For the associations, we match the NUV-selected, 32 pc scale, stellar associations to the individual H II regions in the same manner as Scheuermann et al. (2023). The associations catalog comes with spatial masks identifying the footprint of all of the detected associations. Because the association masks have a finer pixel scale than the KCWI H II region masks, we reproject the KCWI mask onto the association mask pixel grid. We find for cluster matches that only 65 of 260 or (25%) of our H II regions are matched to a single cluster. Additionally, 150 of 260 (or 57%) of our H II regions have zero matches. For

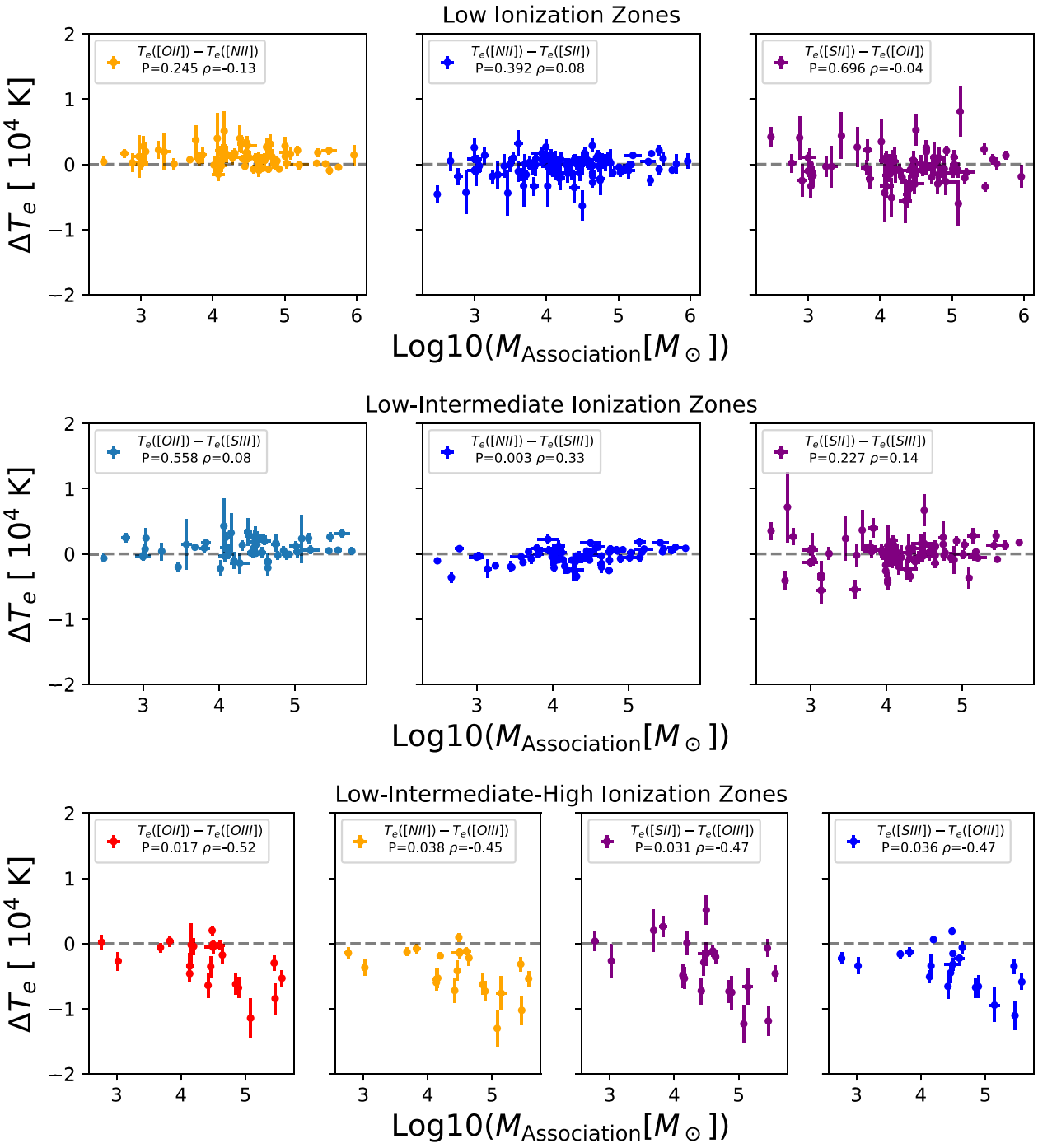

Figure 15. Electron temperature differences compared to stellar association mass. The ionization zones depicted in each row follow those in Figure 12. Although the correlations are insignificant according to their p-value, we observe potential, weak correlations between $\Delta(T_{e,[N\ II]}, T_{e,[S\ III]})$, and all ΔT_e involving $T_{e,[O\ III]}$, with stellar association mass.

association matches, only 85 of 260 (or 33%) of our H II regions are matched to a single association; 45 of 260 (or 17%) of our H II regions have zero matches.

For the remaining regions with more than one cluster or association match, because we expect that the youngest and most massive clusters or associations contribute most to the overall ionization of the H II region, we assign to each H II region the age (mass) of the youngest (most massive) available cluster/association.

7. Results

We present electron temperatures derived using the auroral-to-nebular line ratios from [O II], [N II], [S II], [S III], and [O III]. We construct T_e–T_e diagrams to compare any multi-ionization zone T_e relationships to recently measured and/or modeled trends. We then compare the temperatures to properties of the ionized gas such as electron density, n_e, and ionization parameter, U. We also relate the temperatures to properties of the molecular gas and stellar populations. We

present in Table 9 a summary of the measured emission lines and derived properties for the H II regions with two or more detected auroral lines.

7.1. Temperature–Temperature Relations

We show T_e–T_e relations for our sample H II regions in Figures 8–10. The left panel displays the individual H II region measurements. To assess the significance of each T_e–T_e relation, we calculate its p-value. A correlation is judged to be significant if it exhibits $p \lesssim 10^{-3}$. With the exception of $T_{e,[N\,II]}$–$T_{e,[O\,II]}$ and the relations involving $T_{e,[O\,III]}$, the remaining T_e–T_e relations are deemed significant according to their p-value. For these significant T_e–T_e relations, we derive the best-fitting linear relation using the Bayesian linear regression tool LINMIX,[28] which itself is a Python implementation of linear mixture model algorithm, LINMIX_ERR, constructed by Kelly (2007). The linear regression in LINMIX includes an additional term to represent the intrinsic scatter weighting each data point. In the panels of Figures 8 and 9, we report σ_{int}, or the median of the Normal distributed scatter around the linear regression, and the total scatter, σ_{tot}. Furthermore, to better see T_e–T_e relationships in individual galaxies, we show in the right panel the T_e–T_e relations for temperatures binned in steps of 2000 K on the x-axis, with minimum 2 H II regions per bin, for each galaxy. Alongside the binned data, we show recent T_e–T_e relations from Berg et al. (2020, hereafter CHAOS-IV), Rogers et al. (2021, hereafter CHAOS-VI), Zurita et al. (2021, hereafter Z21), Garnett (1992, hereafter G92), Vale Asari et al. (2016, hereafter BOND), and Méndez-Delgado et al. (2023b, hereafter MD23).

7.1.1. Low-ionization Zone

The low-ionization zone T_e–T_e relations are shown in Figure 8. The top panels show the $T_{e,[N\,II]}$–$T_{e,[O\,II]}$ comparison. We observe that $T_{e,[O\,II]}$ gives higher values than $T_{e,[N\,II]}$ by 1000 K on average. The magnitude of this offset is largest when $T_{e,[O\,II]} > 1.0 \times 10^4$ K. The $T_{e,[O\,II]} > T_{e,[N\,II]}$ inequality is also reflected in the relations from Z21, CHAOS-VI, and MD23. We also show in gray the best-fit line, and the corresponding 1σ uncertainty, described by, $T_{e,[N\,II]} = (0.47 \pm 0.13) \times T_{e,[O\,II]} + (0.36 \pm 0.10)$. The CHAOS-VI, MD23, and Z21 relations are within the uncertainties of the fit, indicating that the $T_{e,[N\,II]}$–$T_{e,[O\,II]}$ relation is in good agreement with these studies. We also measure scatter around the trend line of $\sigma_{int} = 560$ K and $\sigma_{tot} = 844$ K, both of which are in good agreement with the reported values of $\sigma_{int} = 588$ K and $\sigma_{tot} = 810$ K by CHAOS-VI.

The comparison between $T_{e,[S\,II]}$ and $T_{e,[N\,II]}$ is shown in the middle panel of Figure 8. The best-fit line is described by $T_{e,[S\,II]} = (0.85 \pm 0.15) \times T_{e,[N\,II]} + (0.13 \pm 0.12)$. Only the trend from Z21 is within the uncertainties of our fit. Both CHAOS-VI and MD23 favor a steep slope (i.e., hotter $T_{e,[S\,II]}$) and are outside the 1σ bounds of our fit. We measure a low intrinsic scatter $\sigma_{int} = 735$ K but a larger total scatter $\sigma_{tot} = 4744$ K. For comparison, CHAOS-VI reports $\sigma_{int} = 945$ K and $\sigma_{tot} = 1460$ K.

We show the temperature relation between $T_{e,[S\,II]}$ and $T_{e,[O\,II]}$ in the bottom left panel. We observe large scatter around the line of equality, $\sigma_{tot} = 2279$ K, toward hot temperatures, and we measure a p-value, $p = 0.09$, that suggests the two temperatures are uncorrelated. We discuss a potential, physical explanation of the scatter in Section 7.2, but first we explore effects on the correlation due to low-S/N detections. Low-S/N detections of weak emission can have an intrinsic bias toward higher values (see Rola & Pelat 1994), which in the case of weak detections of the auroral lines of [S II] and [O II] would result in high temperatures. To explore how S/N changes the observed trend, we recalculated the p-value line using only T_e derived from [S II] and [O II] auroral lines with S/N > 5. Using the higher-S/N threshold, the p-value returned is now $p = 0.04$, but this is not significant according to our criteria. Furthermore, the total scatter, $\sigma_{tot} = 1743$ K, around the 1-to-1 line is high.

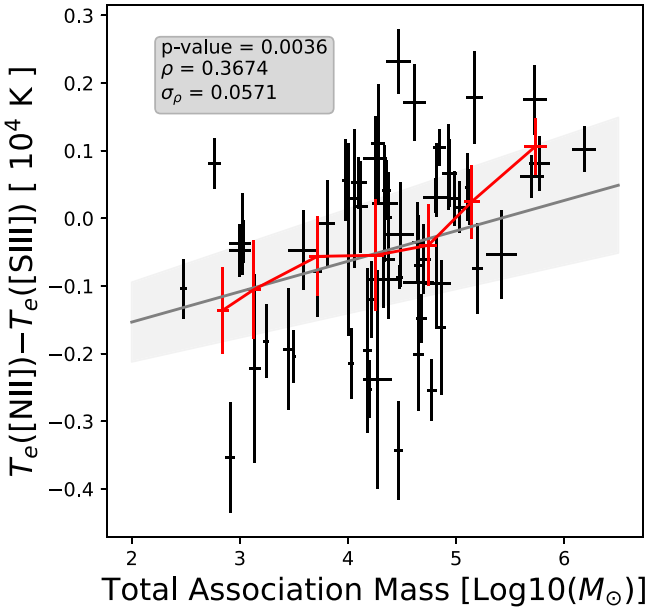

Figure 16. The $T_{e,[N\,II]}$−$T_{e,[S\,III]}$ temperature difference vs. the total stellar association mass. The black points are individual H II region association masses. In red, we show the average temperature differences and H II region association masses calculated in Log10($M_\odot$) = 0.5 bins. We also show a fit and 1σ fit in gray. Compared to using the largest mass measurement (see the middle row of Figure 15), the p-value using the total stellar mass p-value is higher, indicating a less statistically significant correlation.

We observe in the T_e–T_e relations that $T_{e,[O\,II]}$ and $T_{e,[S\,II]}$ are systematically hotter than $T_{e,[N\,II]}$. Based on photoionization models (e.g., Campbell et al. 1986; Garnett 1992), the low-ionization zone temperatures are expected to be equal. There are systematic effects that could increase $T_{e,[O\,II]}$ and $T_{e,[S\,II]}$ temperatures such that $T_{e,[O\,II]} \sim T_{e,[S\,II]} > T_{e,[N\,II]}$. The wide wavelength range between [O II]$\lambda\lambda$7320, 7330 and [O II] $\lambda\lambda$3726, 3729 as well as [S II]$\lambda\lambda$4068, 4076 and [S II] $\lambda\lambda$6716, 6731, make these ratios sensitive to the applied reddening correction. An overestimate in the extinction would lead to an underestimate of $T_{e,[O\,II]}$ and underestimate of $T_{e,[S\,II]}$. At the same time, this would leave $T_{e,[N\,II]}$ relatively unchanged, due to the proximity in wavelength of the requisite lines. We see that both $T_{e,[O\,II]}$ and $T_{e,[S\,II]}$ are greater than $T_{e,[N\,II]}$, which is not compatible with the effects of overestimated extinction correction. Despite the above, our temperature hierarchy could potentially be produced by underestimated extinction, as this would lead to overestimates of $T_{e,[O\,II]}$ and $T_{e,[S\,II]}$ while again leaving $T_{e,[N\,II]}$ unchanged. We tested two different extinction prescriptions (O'Donnell 1994; Fitzpatrick 1999) and found no change in our results.

[28] https://github.com/jmeyers314/linmix

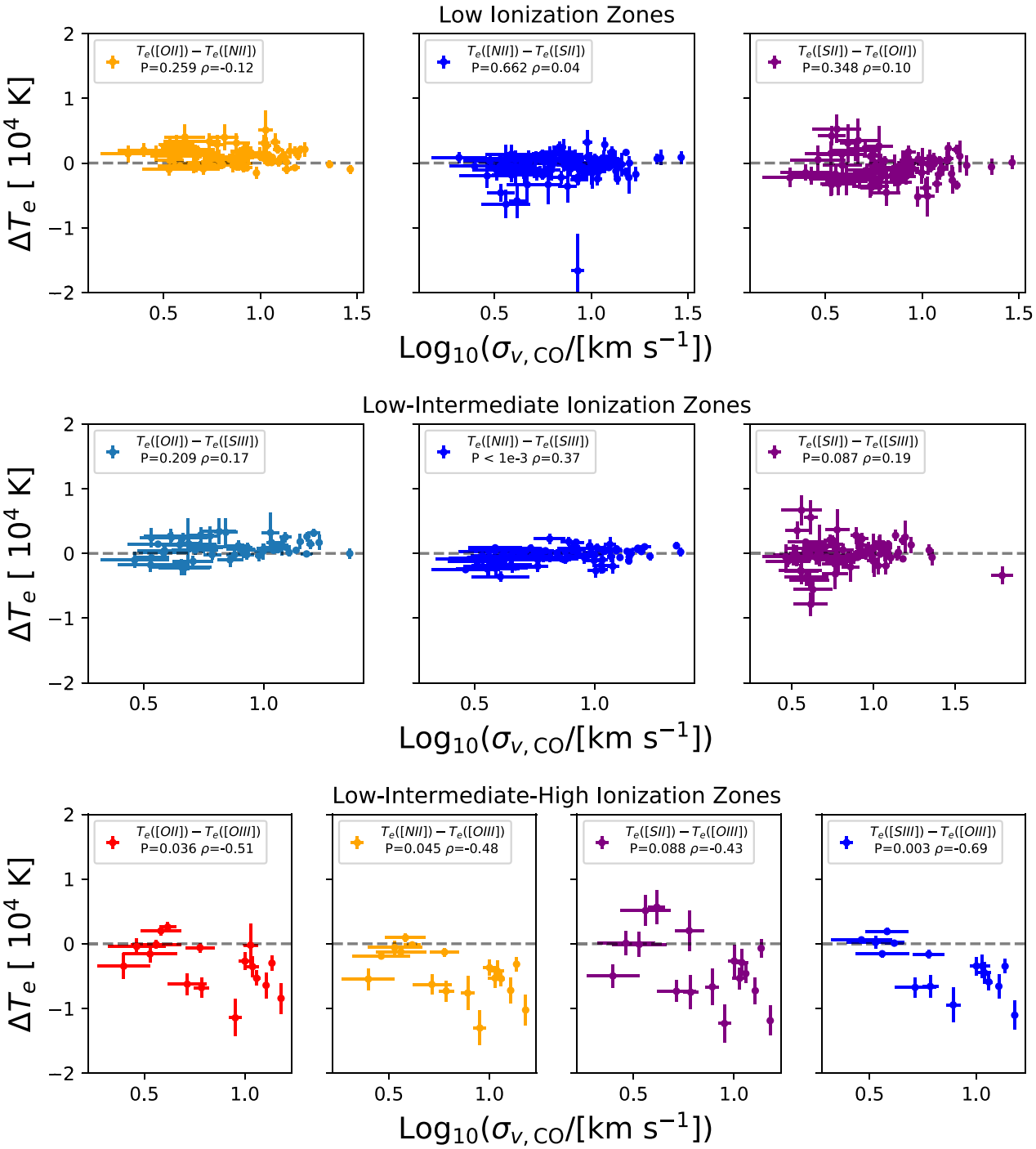

Figure 17. Electron temperature differences compared to the CO velocity dispersion, $\sigma_{v,\mathrm{CO}}$. The order of the panels follows that in Figure 12. We observe a weak correlation between $\Delta(T_{\mathrm{e,[N\ II]}}, T_{\mathrm{e,[S\ III]}})$. Although insignificant according to their p-values, we also observe that highest $T_{\mathrm{e,[O\ III]}}$ values are associated with the highest $\sigma_{v,\mathrm{CO}}$.

Due to the possible DIG contribution to the measured extinction, it is more likely that we could be overestimating the extinction than underestimating it (Congiu et al. 2023). Telluric contamination to the line emission at [O II]$\lambda\lambda$7320, 7330 could be an additional systematic error, but it is unlikely to be significant in our data because the [O II]λ7320/λ7330 ratio measured for our sample is 1.27 ± 0.3, in agreement with values predicted by the transition probabilities and the collisional strengths (Zeippen 1982; Kisielius et al. 2009) and observed in nearby H II regions (Seaton & Osterbrock 1957; Kaler et al. 1976; Yates et al. 2020; Méndez-Delgado et al. 2022). The [S II]$\lambda\lambda$4068, 4076 doublet may contain $\sim$10% contamination due to O II recombination emission near the location of [S II]$\lambda\lambda$4068, 4076 (Méndez-Delgado et al. 2023b) that could bias $T_{\mathrm{e,[S\ II]}}$ upward by $\sim 0.2 \times 10^4$ K for $T_{\mathrm{e,[S\ II]}} < 2.0 \times 10^4$ K. The KCWI spectral resolution is too low to separate out any contamination in the measurements of [S II] $\lambda\lambda$4068, 4076. Finally, $T_{\mathrm{e,[O\ II]}}$ and $T_{\mathrm{e,[S\ II]}}$ have a higher sensitivity to electron density inhomogeneities than $T_{\mathrm{e,[N\ II]}}$ (Rubin 1989; Osterbrock & Ferland 2006; Méndez-Delgado

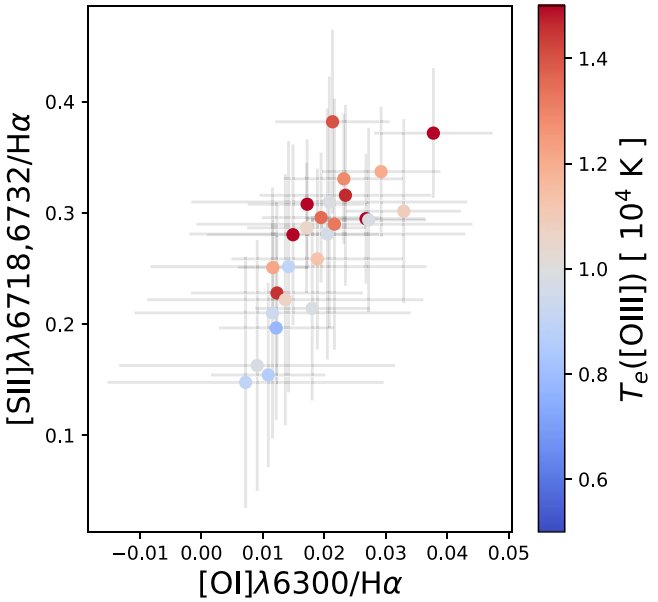

Figure 18. We compare the relative strength of the low-ionization species [O I] and [S III] to Balmer emission. We color-code each data point by the value of its measured [O III] temperature. The hottest $T_{e,[O\ III]}$ regions also have the highest line ratios. The higher line ratios are indicative of the existence of a partially ionized zone that may be due to the presence of shocks or harder photons such as X-rays (Grisé et al. 2008).

Table 3
Transitions Probabilities, Collision Strengths, and Critical Densities for the Relevant Emission Lines Used in the PyNeb Temperature Determinations

Ion	Transition Probabilities	Collision Strengths	$n_{crit,nebular}$ (10^3 cm^{-3})
[O II]	Zeippen (1982)	Kisielius et al. (2009)	2[a]
[O III]	Froese Fischer & Tachiev (2004)	Storey et al. (2014)	691
[N II]	Froese Fischer & Tachiev (2004)	Tayal (2011)	88
[S II]	Rynkun et al. (2019)	Tayal & Zatsarinny (2010)	3[b]
[S III]	Froese Fischer et al. (2006)	Tayal & Gupta (1999)	543[c]

Notes.
[a] Average critical density for [O II]λλ3726, 3729.
[b] Average critical density for [S II]λλ6716, 6731.
[c] Average critical density for [S III]λλ9069, 9532.

et al. 2023b). [O II] and [S II] start to be dependent on density around $n_e \approx 10^3$ cm^{-3}, while [N II] is independent of density up to $n_e \approx 10^4$ cm^{-3}.

Despite all of the above factors, including S/N considerations, and given the agreement of the $T_{e,[S\ II]}$–$T_{e,[N\ II]}$ and $T_{e,[N\ II]}$–$T_{e,[O\ II]}$ trends with those from Z21 using the S/N > 3 [O II] and [S II] auroral lines, we are motivated to explore potential biases due to uncertainties in the measured electron density; see Section 7.2.

7.1.2. Intermediate-ionization Zone

The T_e–T_e relations between the low- and intermediate-ionization zone temperatures are shown in Figure 9. Given the lower ionization potentials of O^+, N^+, and S^+ with respect to S^{++}, it is possible to have differences in the temperature in the different ionization zones (Garnett 1992). We compare our observed T_e–T_e relations to predictions from photoionization models for giant H II regions produced by the Bayesian oxygen and nitrogen abundance project BOND and found in the Mexican Million Models database (Morisset 2009). When available, we also compare the observations to relations from CHAOS-VI, MD23, and Z21.

Table 4
Median Temperature for Each Ion

$T_{e,Ion}$	Median[a] (10^4 K)	$N_{regions}$[b]
$T_{e,[O\ II]}$	$0.95^{+0.22}_{-0.12}$	156
$T_{e,[N\ II]}$	$0.81^{+0.12}_{-0.09}$	245
$T_{e,[S\ II]}$	$0.94^{+0.19}_{-0.14}$	305
$T_{e,[S\ III]}$	$0.89^{+0.30}_{-0.10}$	143
$T_{e,[O\ III]}$	$1.20^{+0.35}_{-0.16}$	26

Notes.
[a] The 50th ± the 16th–84th percentile of the measured temperatures.
[b] Number of H II regions with temperature measured from the particular ion.

The top panel of Figure 9 shows the temperature comparisons between $T_{e,[S\ III]}$ and $T_{e,[O\ II]}$. The best-fit line, $T_{e,[S\ III]} = (0.67 \pm 0.27) \times T_{e,[O\ II]} + (0.022 \pm 0.022)$, closely follows the relationship reported by Z21. We measure an intrinsic scatter $\sigma_{int} = 1002$ K and a total scatter $\sigma_{tot} = 1496$ K. The (BOND) models predict that the temperature $T_{e,[S\ III]}$ should be greater than $T_{e,[O\ II]}$ by a small constant offset across the full temperature range. However, our data suggest $T_{e,[O\ II]}$ rises faster than $T_{e,[S\ III]}$. Our binned data favor the empirical trend line from Z21. However, there is a grouping of points from NGC 5068 that show contrasting behavior in both the individual and binned data comparisons.

The $T_{e,[S\ III]}$ and $T_{e,[S\ II]}$ comparison, comprising 108 H II regions, is shown in the middle panel of Figure 9. The best-fit line for this comparison is described by $T_{e,[S\ III]} = (1.11 \pm 0.25) \times T_{e,[S\ II]} - (0.045 \pm 0.21)$. Within uncertainties, the values of $T_{e,[S\ III]}$–$T_{e,[S\ II]}$ agree with trends observed by Z21 and that derived from BOND. However, both the intrinsic scatter, $\sigma_{int} = 1627$ K, and the total scatter, $\sigma_{tot} = 2598$ K, are large. The binned data do not reveal a preference for either of the literature trends.

The series of CHAOS T_e–T_e comparisons (see Berg et al. 2015, 2020; Rogers et al. 2021, 2022) and Z21 have observed a tight relationship between $T_{e,[S\ III]}$ and $T_{e,[N\ II]}$. We show in the bottom panel of Figure 9 a comparison of $T_{e,[S\ III]}$ and $T_{e,[N\ II]}$. Satisfying the expectations driven by these past studies, we observe that the trend between $T_{e,[S\ III]}$ and $T_{e,[N\ II]}$ exhibits the smallest scatter of the T_e–T_e relations presented here. The trend between these temperatures is described by $T_{e,[S\ III]} = (1.35 \pm 0.15) \times T_{e,[N\ II]} - (0.24 \pm 0.11)$, and it exhibits intrinsic scatter $\sigma_{int} = 997$ K and total scatter $\sigma_{tot} = 1313$ K, both of which are larger than the $\sigma_{int} = 173$ K $\sigma_{tot} = 507$ K reported by CHAOS-VI.

For the $T_{e,[S\ III]}$ and $T_{e,[N\ II]}$ comparison, there are available empirical relations from CHAOS-VI, Z21, and MD23, which we overlay in addition to the BOND models. The data show a clear disagreement with the trend observed by MD23. We observe a large fraction of the binned data that lie near the CHAOS-VI model, as well as Z21 relations at low $T_{e,[N\ II]}$.

Table 5
Summary of the p-values and Spearman Rank Coefficients for Comparisons between ΔT_e and the Ionization and Radiation Softness Parameters of the H II Regions

ΔT_e	[S III]/[S II] (ρ, p)	[O III]/[O II] (ρ, p)	η (ρ, p)
$\Delta(T_{e,[O\ II]}, T_{e,[N\ II]})$	⋯	⋯	⋯
$\Delta(T_{e,[N\ II]}, T_{e,[S\ II]})$	$(-0.27, <10^{-3})$	⋯	⋯
$\Delta(T_{e,[S\ II]}, T_{e,[O\ II]})$	$(0.32, <10^{-3})$	⋯	⋯
$\Delta(T_{e,[O\ II]}, T_{e,[S\ III]})$	⋯	⋯	⋯
$\Delta(T_{e,[N\ II]}, T_{e,[S\ III]})$	⋯	⋯	⋯
$\Delta(T_{e,[S\ II]}, T_{e,[S\ III]})$	$(0.53, <10^{-3})$	⋯	$(0.46, <10^{-3})$
$\Delta(T_{e,[O\ II]}, T_{e,[O\ III]})$	⋯	$(0.85, <10^{-3})$	⋯
$\Delta(T_{e,[N\ II]}, T_{e,[O\ III]})$	$(0.72, <10^{-3})$	$(0.82, <10^{-3})$	⋯
$\Delta(T_{e,[S\ II]}, T_{e,[O\ III]})$	$(0.75, <10^{-3})$	$(0.75, <10^{-3})$	⋯
$\Delta(T_{e,[S\ III]}, T_{e,[O\ III]})$	⋯	$(0.82, <10^{-3})$	⋯

Regions with hotter $T_{e,[N\ II]}$ and $T_{e,[S\ III]}$ would be needed in order to further differentiate between the models and empirical trends.

7.1.3. High-ionization Zone

We show T_e–T_e relations between [O III] temperatures (which trace the high-ionization zone) and those from the low- and intermediate-ionization zones in Figure 10. Additionally, we overlay T_e–T_e relations from CHAOS-IV, Z21, and G92. Although we observe some H II regions with T_e–T_e relations that agree with literature relations, we also observe numerous H II regions with values of $T_{e,[O\ III]}$ that are much higher than those predicted by models with the given low- and intermediate-ionization zone temperatures. The total scatter around the line of equality in $T_{e,[O\ III]}$ ranges between 3100 and 4500 K. Given this large scatter, we do not perform a linear regression analysis for these comparisons.

Based on previous findings from Z21 and CHAOS-VI, the scatter toward large excess in $T_{e,[O\ III]}$ for regions with cooler low- and intermediate-ionization zone temperatures is unexpected. With IFUs, we are perhaps capturing a wider range of H II regions. Furthermore, Z21 and CHAOS-VI extend to lower metallicities, and possibly higher ionization parameters, where $T_{e,[O\ III]}$ may be better behaved. Nevertheless, these regions represent an extremely limited subset of the data and are at the boundary of significance, so they are subject to higher uncertainty. For the ∼solar metallicities for our H II region sample, where the relative flux [O III]λ4363 is expected to be $<10^{-2} \times H\beta$ (Berg et al. 2015), the temperature from [O III] λ4363 would have to be high in order to be detected. The small number of [O III]λ4363 detections reflects this. Because we do not expect to detect the line in most H II regions, the ones we do detect may be unusual cases or statistical outliers, especially given that the average S/N of the [O III] detections is ∼4. We explore S/N effects by increasing the threshold for comparison to S/N > 5 in [O III]λ4363. This reduces the sample of regions with $T_{e,[O\ III]}$ measurements to 5, which is too low to confidently fit a trend, but we measure a large total scatter, $\sigma_{tot} > 2000$ K, around the line of equality. Discussed further in Section 7.3.1 and in Yates et al. (2020), these regions exhibit low [O III]/[O II] ratios, meaning they are systems with low O^{++}/O^{+}. This would mean that a small fraction of the total nebulae volume would be described by the high $T_{e,[O\ III]}$. Despite this, there has been evidence (Peimbert et al. 1991; Binette et al. 2012) that shock excitation can preferentially enhance the high-ionization zone temperature, with the highest enhancement occurring in high-metallicity environments. How this scenario could apply to this small subset of H II regions is explored in Section 7.3.4.

7.2. The Impact of Density Inhomogeneities on [S II] and [O II] Temperatures

Recent studies have suggested that the temperatures obtained from the auroral-to-nebular lines ratios of [O II] and [S II] can be biased upward due to the presence of density inhomogeneities, even while the average density is underestimated by nebular doublet line [O II]$\lambda\lambda$3726, 3729 and [S II]$\lambda\lambda$6716, 6731 diagnostics.

For example, in a sample of 190 high-S/N spectra of H II regions and other photoionized nebulae, Méndez-Delgado et al. (2023b) observed systematically hotter $T_{e,[O\ II]}$ and $T_{e,[S\ II]}$ relative to $T_{e,[N\ II]}$, similar to what we observe, which they attribute to the presence of density inhomogeneities. The atomic levels responsible for the nebular lines [S II]$\lambda\lambda$6731, 6716 and [O II]$\lambda\lambda$3726, 3729, listed in Table 3, have critical densities of the order of 10^3 cm^{-3}, which are at least 2 orders of magnitude lower than the critical densities for the nebular levels of [N II]. In addition, the auroral levels of the same ions have very high critical densities. This makes the auroral-to-nebular temperature diagnostics of $T_{e,[O\ II]}$ and $T_{e,[S\ II]}$ densities sensitive to levels above 10^3 cm^{-3}, and therefore susceptible to biases if there are important contributions to the line flux from gas above that density. The auroral-to-nebular ratio of [N II], however, is not susceptible to such sensitivity until much higher densities.

Both [S II]$\lambda\lambda$6731, 6716 and [O II]$\lambda\lambda$3726, 3729 nebular line doublet ratios serve as density diagnostics for densities 10^2 cm$^{-3} < n_e < 10^{3.5}$ cm^{-3}. Furthermore, because of the bias described above, Méndez-Delgado et al. (2023b) showed that, at fixed temperatures, the auroral-to-nebular line ratios for [O II] and [S II] can serve as a density diagnostic over a large range of electron density, 10^2 cm$^{-3} < n_e < 10^6$ cm^{-3}. For a uniform-density H II region, the n_e returned from both of these diagnostics should be identical, as long as n_e is within the sensitivity range of the diagnostics. However, in the presence of density inhomogeneities, different density diagnostics can return conflicting values. Even if high-density gas clumps make up a small fraction of the gas, such regions can continue to contribute to the auroral-line emission while no longer contributing significantly to the nebular lines, because the effects of collisional de-excitation on the nebular lines will reduce their emissivities relative to the auroral lines (Rubin 1989). Because of this, the nebular [S II] and [O II] lines can reflect the dominant contribution of low-density gas, while the auroral [S II] and [O II] lines will be sensitive to the volume of high-density gas (Peimbert 1971; Rubin 1989; Méndez-Delgado et al. 2023b).

To investigate whether the presence of density inhomogeneities could bias our measured $T_{e,[S\ II]}$ and $T_{e,[O\ II]}$, we compare the observed auroral-to-nebular line ratios [O II] and [S II] to those predicted using fixed $T_{e,[N\ II]}$. For this comparison, we use the regions with auroral-line detections for all three low-ionization zone ions. We show in Figure 11 the measured [O II] $\lambda\lambda$7320, 7330/$\lambda\lambda$3726, 3729 and [S II]$\lambda\lambda$4069, 4076/$\lambda\lambda$6716, 6731 line ratios versus the region's $T_{e,[N\ II]}$. We overlay the predicted trends of auroral-to-nebular line ratios calculated

using $n_e = 10^2\,cm^{-3}$, $10^{2.5}\,cm^{-3}$, and $10^3\,cm^{-3}$. We see in Figure 11 that, under the assumption that $T_{e,[N\,II]} = T_{e,[S\,II]} = T_{e,[O\,II]}$, the largest measured auroral-to-nebular line ratios could be consistent with T_e traced by $T_{e,[N\,II]}$ but with a higher electron density than that returned by [S II]$\lambda\lambda$6731, 6716 in the low-density limit. This suggests that, under inhomogeneous conditions, underestimated contributions from $>10^3\,cm^{-3}$ gas to the nebular [O II] and [S II] lines could bias the density diagnostics, and then the use of underestimated densities in temperature calculations for ions with low critical densities like [O II] and [S II] could lead to hotter estimated temperatures inferred from auroral-to-nebular ratios.

At the same time, Figure 11 also shows that the lowest measured auroral-to-nebular ratios lie below the theoretical curves for ratios with densities equal to the low-density limit. It may be the case that, under our assumption that the H II region low-ionization zone T_e is described by $T_{e,[N\,II]}$, these regions physically exhibit volumes of gas with $n_e \lesssim 10\,cm^{-3}$ or lower (Kennicutt 1984). However, we are unable to verify this using the available diagnostics, because densities returned by either the [O II] and [S II] doublet or their auroral-to-nebular line ratios are uncertain in this regime. For this reason, we do not pursue further interpretation of these points.

We can further explore potential density inhomogeneities by comparing the measured auroral-to-nebular lines to a region's Hβ surface brightness. The emission from any recombination lines is proportional to $n_e n(X^+)\alpha_{eff}$, where $n(X^+)$ is the number density of the emitting ion and α_{eff} is the effective recombination coefficient (Peimbert et al. 2017). For Hβ, $n(X^+) \propto n_e$ because 90% of free electrons will come from the photoionization of H, which represents ~90% of all of the gas. For a uniform-density H II region, the Hβ surface brightness, $SB_{H\beta}$, would be proportional to n_e^2. In the case of H II regions with high-density inclusions, the variance of n_e would be expected to rise due to the increase in the average of the density squared (i.e., $\langle n_e^2 \rangle$). Under such conditions, it would be reasonable to expect that Hβ surface brightness would increase as $SB_{H\beta} \propto \langle n_e^2 \rangle$.

If we interpret the departure of the measured auroral-to-nebular lines ratios from the theoretical ratios calculated by fixing the electron density at the low-density limit, $n_e = 100\,cm^{-3}$ and $T_e = T_{e,[N\,II]}$, then we could expect that this deviation would correlate with the Hβ surface brightness. We show in the bottom panels of Figure 11 the degree of inhomogeneities, measured by [S II]–[S II]($n_e = 100$, $T_{e,[N\,II]}$) and [O II]–[O II]($n_e = 100$, $T_{e,[N\,II]}$), against the regions Hβ surface brightness.

We find a significant correlation, p-value $< 10^{-3}$, between [S II]–[S II]($n_e = 100$, $T_{e,[N\,II]}$) and $SB_{H\beta}$, which suggests that the regions with large deviations from the predicted low-density limit auroral-to-nebular line ratios are consistent with density inhomogeneities. The best-fit line is described by [S II]–[S II]($n_e = 100$, $T_{e,[N\,II]}$) $= 0.0147(\pm 0.004) \times SB_{H\beta} + 0.20(\pm 0.05)$. To account for any uncertainties in the atomic data, we vary the absolute value of the [S II]($n_e = 100$, $T_{e,[N\,II]}$) curve by ±10% (Mendoza & Bautista 2014) and find no change in correlation strength. While this correlation is suggestive of density inhomogeneities, we acknowledge that the H II regions are not fully resolved, which means we are measuring a PSF-averaged surface brightness. Because of this, it is unclear whether this correlation can be fully linked to density inhomogeneities.

For the comparison involving [O II]–[O II]($n_e = 100$, $T_{e,[N\,II]}$), we find no significant correlation with Hβ surface brightness, even when using S/N > 5 auroral lines. While the exact reason for the noncorrelation between [O II]–[O II]($n_e = 100$, $T_{e,[N\,II]}$) and Hβ surface brightness is unknown, it is important to note that the ionization potential of [S II] is less than those of both $H\beta$ and [O II]. This difference in ionization potential means that H II region [S II] and [O II] may not be cospatial, and they may have different sensitivities as tracers of high-density inclusions. However, given that these regions have measurements of all three low-ionization zone auroral lines and survive a DIG contrast constraint, we find that the correlation between [S II]–[S II]($n_e = 100$ and $SB_{H\beta}$ suggests that density inhomogeneities may be affecting the low-ionization zone temperatures. Future studies with multiple density diagnostics and high spatial resolution will be valuable to exploring the potential impact that inhomogeneous conditions have on these diagnostics.

7.3. Temperature Differences Compared to H II Region Ionized Gas, Stellar Population, and Molecular Gas Properties

Studies have shown that H II region temperatures for different ionization zones can be differently impacted by properties of the ISM. Temperature comparisons presented in Berg et al. (2020) using H II regions observed in four nearby galaxies revealed that the dispersion around low-intermediate and intermediate-high T_e–T_e relationships increased (or decreased) with the ionization parameter. Another trend with ionization parameter was observed by Yates et al. (2020). They found that systems with low ionization, or larger ratios of the O^+/O^{2+} parameter, would exhibit systematically hotter $T_{e,[O\,III]}$. However, Arellano-Córdova & Rodríguez (2020) argued this could be explained by increased iron contamination to [O III]λ4363. As discussed in Section 7.2, density fluctuations can also bias the temperatures for the low-ionization zone, due to the sensitivity of [O II] and [S II] to density (Méndez-Delgado et al. 2023a, 2023b).

Given that stars are the primary source of ionizing photons, it is reasonable to suspect that the properties of the stellar population ionizing the H II region can potentially play a role in setting the T_e structure of H II regions. Another potential factor in the T_e structure—and one that is traced by its effects on the surrounding molecular gas—is the degree of stellar feedback within H II regions. Although very important to our understanding, the physical processes that impact the T_e structure in H II regions remain uncertain (Garnett et al. 1991; Nicholls et al. 2020).

The KCWI+MUSE H II regions, combined with the PHANGS-HST and PHANGS-ALMA observations, allow us to investigate how T_e is impacted by different H II ISM, stellar, and molecular gas properties. We compare temperature differences, $\Delta(T_{ion,1}, T_{ion,2}) = T_{ion,1} - T_{ion,2}$, between the low-, intermediate-, and high-ionization zone temperatures. H II region properties are derived from emission-line diagnostics; the properties of the surrounding molecular gas are measured from ALMA (Leroy et al. 2021a); stellar population masses/ages are obtained from SED fitting to HST photometry (Lee et al. 2022; Thilker et al. 2022; Larson et al. 2023).

To gauge the significance and monotonicity of each comparison, we calculate the Pearson correlation coefficient (i.e., p-value or p), as well as the Spearman rank correlation coefficient, ρ. A correlation is judged to be significant if it

exhibits $p \lesssim 10^{-3}$. The strength of the correlation is separated into the following regimes: $1 > |\rho| > 0.8$ corresponds to a *strong* correlation, $0.8 > |\rho| > 0.4$ corresponds to a *moderate* correlation, and $0.4 > |\rho| > 0$ identifies a *weak* or no correlation.

As expected, we observe strong correlations between temperature differences with ionization parameter. We do not report any significant correlations between ΔT_e and any of the following properties: integrated CO intensity, CO peak temperature, molecular gas velocity dispersion, cluster mass, cluster age, or association age. Figures showing the ΔT_e comparisons to these parameters are shown in Appendix E. Despite the absence of significant correlations, we do find interesting behavior between $\Delta(T_{e,[N\,II]}, T_{e,[S\,III]})$ with association mass, and excess $T_{e,[O\,III]}$ with molecular gas velocity dispersion. We discuss these special cases and the details of the comparisons in the sections that follow. The statistics of the correlations with H II region ionization parameter are summarized in Table 5.

7.3.1. Correlations between Temperature Differences, Ionization Parameter, and Radiation Softness Parameter

We show in Figures 12 and 13 the comparisons between temperature differences and the ionization parameter, U, traced with both [S III]/[S II] and [O III]/[O II]. In both comparisons, the low-ionization zones show no correlations, but there is a moderate correlation between the low- and intermediate-ionization zones, traced by $\Delta(T_{e,[S\,II]}, T_{e,[S\,III]})$, with [S III]/[S II]. Comparisons of the low-intermediate and high-ionization zones reveal high correlations with both [S III]/[S II] and [O III]/[O II].

We observe correlations between $\Delta(T_{e,[S\,II]}, T_{e,[S\,III]})$ with [S III]/[S II]. For all temperature differences with $T_{e,[O\,III]}$, we also observe strong correlations between ΔT_e and [S III]/[S II]. The largest temperature differences are associated with the smallest values of [S III]/[S II]. As [S III]/[S II] increases, ΔT_e converges to $\Delta T_e = 0$. In Figure 13, we present the same temperature differences but using [O III]/[O II] as a tracer for U. All of the correlations with ionization parameter that do not involve $T_{e,[O\,III]}$ disappear when using [O III]/[O II] as a tracer. The remaining ΔT_e that include $T_{e,[O\,III]}$ show similar correlations as before with ionization parameter when using [O III]/[O II]. In both cases, the largest temperature differences occur at the lowest values of the ionization parameter, traced by either [S III]/[S II] or [O III]/[O II].

Our correlations with ionization parameter tracers are similar to the results presented in Yates et al. (2020). When comparing the temperatures of the low- and high-ionization zones for oxygen, Yates et al. (2020) observed an increase in the $T_{e,[O\,III]}/T_{e,[O\,II]}$ ratio that is anticorrelated with the ratio of O^{2+}/O^{+} (which closely follows the ionization parameter traced by [O III]/[O II]). Our H II regions are all likely to be in the relatively high-metallicity regime, where O^{+} should be the dominant ionization state of oxygen. Here, the average electron temperature will be best described by the auroral-to-nebular line ratio of [O II] (with the previously mentioned caveats regarding density inhomogeneities). Nevertheless, emission from [O III]λ4363 can still be produced, albeit more weakly, and given the exponential temperature dependence, it will be biased toward hotter gas. Therefore, if there are temperature inhomogeneities, the [O III] temperatures may reflect a small amount of hot, high-ionization gas and may not agree with the auroral-to-nebular line ratio of [O II]. Yates et al. (2020) predicted that regions with $T_{e,[O\,III]} > T_{e,[O\,II]}$ will be O^{+} dominant, i.e., $O^{+}/H^{+} > O^{2+}/H^{+}$. Because [O III]/[O II] $\propto O^{2+}/O^{+}$, we would expect to see the largest deviations in $T_{e,[O\,III]}$ at the lowest [O III]/[O II]. To summarize, Yates et al. (2020) postulated that the differences between hotter high-ionization zone temperatures, $T_{e,[O\,III]}$, and the low-ionization zone temperature, $T_{e,[O\,II]}$, will increase with decreasing ionization parameter. These trends should, in theory, also be evident for sulfur, although these correlations were not explored by Yates et al. (2020). Similar trends of temperature differences associated with different ionization states of the gas have been discussed by Berg et al. (2020).

In Figure 14, we plot the T_e–T_e between $T_{e,[O\,III]}$–$T_{e,[O\,II]}$ and $T_{e,[S\,III]}$–$T_{e,[S\,II]}$ colored by the value of [O III]/[O II] and [S III]/[S II]. We also annotate the plot according to the schematics from Figure 3 of Yates et al. (2020). For both oxygen and sulfur, the largest ratios of $T_{e,[X\,III]}/T_{e,[X\,II]}$, where X is either S or O, occur for the lowest values of ionization parameter, as indicated by the value of the line ratio. This suggests we are observing a correlation with the ionization parameter similar to that postulated by Yates et al. (2020).

If we consider the similarity between our results and those of Yates et al. (2020) as evidence for correlations between ΔT_e and U, then why is it that the correlation between $\Delta(T_{e,[S\,II]}, T_{e,[S\,III]})$ and U traced by [S III]/[S II] is not evident when using [O III]/[O II] as a tracer for U? It might be the case that [S III]/[S II] and [O III]/[O II] do not change with U in similar ways, as [S III] and [O III] arise from different ionization zones and conditions. It is also possible that density inhomogeneities may be playing a role; both [S II] and [O II] have similarly low critical densities, unlike either [S III] or [O III]. It remains unclear why some ΔT_e versus U trends disappear.

We explore the correlations with ΔT_e using a combination of both [S III]/[S II] and [O III]/[O II]. Vilchez & Pagel (1988) defined the "radiation softness" parameter, $\eta = ([O\,II]/[O\,III])/([S\,II]/[S\,III])$, as a diagnostic of the effective temperature of the ionizing stars. As shown in Appendix E in Figure 31, we find a correlation between $\Delta(T_{e,[S\,II]}, T_{e,[S\,III]})$ and η that exhibits p and ρ values similar to those of the correlation with U. There are no correlations between temperature differences involving $T_{e,[O\,III]}$ with η. Because η is a measure of the ionizing properties of the ionizing stars, the correlation between η and $\Delta(T_{e,[S\,II]}, T_{e,[S\,III]})$ may suggest that T_e values derived from sulfur lines are sensitive to the stellar population while T_e values from oxygen are more sensitive to the physical conditions of the ionized gas. However, a future comparison with a larger sample of $T_{e,[O\,III]}$ measurements would be beneficial in solidifying such an interpretation.

7.3.2. Temperature Differences with Stellar Mass and Age

Next, we compare temperature differences to stellar mass and ages from compact stellar clusters and associations matched to our H II regions. As presented in Appendix C, Figures 32–34, we find no correlations between ΔT_e with cluster mass and cluster age, nor with association mass and age.

Although the correlation is not statistically significant according to our criteria, we speculate on a possible positive correlation between the most reliable ΔT_e indicator without density inhomogeneity issues, $\Delta(T_{e,[N\,II]}, T_{e,[S\,III]})$, with the association mass. Figure 15 shows the comparisons between $\Delta(T_{e,[S\,II]}, T_{e,[S\,III]})$, $\Delta(T_{e,[O\,II]}, T_{e,[S\,III]})$, and $\Delta(T_{e,[O\,II]}, T_{e,[S\,III]})$. While the scatters for both $\Delta(T_{e,[S\,II]}, T_{e,[S\,III]})$ and

$\Delta(T_{e,[O\,II]}, T_{e,[S\,III]})$ are centered around zero, it appears to be the case that $T_{e,[N\,II]}$ is cooler than $T_{e,[S\,III]}$ toward the low-mass end and vice versa on the high-mass end. As discussed in Section 6.5, we assigned the largest-mass stellar population to the H II region if the region was matched to more than one association. To see if this choice has any impact on the strength of the correlation, we plot in Figure 16 the $\Delta(T_{e,[N\,II]}, T_{e,[S\,III]})$ against the sum of the matched association masses. Using the total masses, we observe no change in the strength of the correlation.

It is possible that the correlation between $\Delta(T_{e,[N\,II]}, T_{e,[S\,III]})$ and association mass may result from biases introduced by an undersampling of the initial mass function. Similar to our study, Scheuermann et al. (2023) matched the stellar association catalog (Larson et al. 2023) to H II regions in the Nebular catalog (Kreckel et al. 2019; Groves et al. 2023). Instead of including all masses measured for the associations, which we do in this work, Scheuermann et al. (2023) implement a cutoff and assume masses $<10^4 M_\odot$, as masses below the threshold do not sample the IMF (da Silva et al. 2012). We perform no such cutoff in this study. The correlation between $\Delta(T_{e,[N\,II]}, T_{e,[S\,III]})$ and $M_{Association}$ correlation includes many regions with masses $<10^4 M_\odot$, where the IMF may not be fully sampled. Despite this, we do not fully dismiss this correlation; however, the effects that undersampling the IMF could have on the correlation with $\Delta(T_{e,[N\,II]}, T_{e,[S\,III]})$ warrants further investigation with a larger sample size in order to expand the dynamic range of association mass.

7.3.3. Temperatures Differences and Molecular Gas Properties

We compare temperature differences to the properties of the molecular gas derived from CO emission measured within the projected boundaries of our sample of H II regions. For the comparisons to I_{CO}, shown in Figure 35 of Appendix E, and the comparisons to T_{peak}, shown in Figure 36 of Appendix E, we observe no correlations with temperature differences between the low-, intermediate-, and high-ionization zones.

We show in Figure 17 the temperature differences compared to the CO velocity dispersion ($\sigma_{v,CO}$). We observe a moderate correlation between $\sigma_{v,CO}$ and $\Delta(T_{e,[N\,II]}, T_{e,[S\,III]})$. The values of $\Delta(T_{e,[N\,II]}, T_{e,[S\,III]})$ over the range of $\sigma_{v,CO}$ are small, only encompassing $\Delta(T_{e,[N\,II]}, T_{e,[S\,III]})$ from -1000 to 2000 K. Given the possible correlation with association mass, and this correlation with $\sigma_{v,CO}$, we find it intriguing that these correlations between the low- and intermediate-ionization zones are only seen in $\Delta(T_{e,[N\,II]}, T_{e,[S\,III]})$. It is possible that the low scatter in the T_e–T_e relationship between $T_{e,[S\,III]}$ and $T_{e,[N\,II]}$ in the presence of density inhomogeneities, in contrast to the temperatures from [S II] and [O II], allows for better insight into these underlying trends.

We observe that all of the correlations of ΔT_e involving $T_{e,[O\,III]}$ and $\sigma_{v,CO}$ have large, negative ρ-values, but are all insignificant according to their p-values. The high Spearman rank values for the comparisons between ΔT_e and $\sigma_{v,CO}$ appears to be largely driven by the highest values of $T_{e,[O\,III]}$. Despite the fact that the correlations are not strong, it is clear that the high-$T_{e,[O\,III]}$ regions go along with high CO velocity dispersion.

The CO velocity dispersion can be enhanced by low-velocity shocks originating from the interaction of molecular gas with late-time expansion of supernovae remnants (see Koo et al. 2001; Zhou et al. 2023), as well as from interaction with low-velocity shocks from H II region expansion driven by radiation pressure (Hill & Hollenbach 1978; Kothes & Kerton 2002; Watkins et al. 2023). These low-velocity shocks are also predicted to enhance $T_{e,[O\,III]}$. Shock modeling has shown that outward-expanding low-velocity shocks can create conditions, such as pockets of high post-shock temperature, where the strength of [O III]λ4363 emission will be enhanced compared to the little-to-no increase in emission from [O III]λ5007 (Peimbert et al. 1991; Binette et al. 2012; Méndez-Delgado et al. 2021). The combination of large temperature differences with $T_{e,[O\,III]}$ and high $\sigma_{v,CO}$ suggests that we may be observing the effects of low-velocity shocks. Motivated by this scenario, we search the H II regions for evidence of low-velocity shocks in the following section.

7.3.4. Investigating H II Regions for the Presence of Low-velocity Shocks

The correlations of ΔT_e involving the high-ionization zone and H II region properties [S III]/[S II], [O III]/[O II], and the CO velocity dispersion appears to be driven by the presence of regions with high $T_{e,[O\,III]}$, high $\sigma_{v,CO}$, and low U. One potential explanation is the presence of low-velocity shocks enhancing $T_{e,[O\,III]}$ (Peimbert et al. 1991; Binette et al. 2012; Méndez-Delgado et al. 2021). To test this explanation, we search for evidence of shocks in enhanced optical-line ratios and line broadening.

When shocks collide with and compress gas, the ionization parameter of the gas is reduced, leading to partially ionized zones of enhanced nebular emission of low-ionization species such as S^+ and O relative to Hβ and/or Hα (Dopita & Sutherland 1996; Allen et al. 2008). In Figure 18, we show the [S II]/Hα versus [O I]/Hα ratios, color coded by $T_{e,[O\,III]}$, for regions with measured [O III]λ4363. We find that H II regions with hotter $T_{e,[O\,III]}$ tend to populate a region with enhanced [S II]/Hα and [O I]/Hα ratios, which suggests that these regions may host a partially ionized zone due to shocks. Between the two line ratios, $T_{e,[O\,III]}$ is better correlated with [S II]/Hα (p-value = 0.0004) than [O I]/Hα (p-value = 0.0016). We note here that it is possible that harder photons and X-rays produced by X-ray binaries also enhance [S II] and [O I] relative to the Balmer emission (Abolmasov et al. 2007; Grisé et al. 2008). Furthermore, X-rays would provide high-energy photons able to boost [O III]λ4363. However, lacking the high spatial resolution X-ray imaging of these H II regions, exploration of X-ray contributions to [O III]λ4363 emission is beyond the scope of this paper.

Another tracer that may indicate presence of shocks is the He II λ4686/Hβ ratio (Allen et al. 2008), though it is also sensitive to the shape of the Lyman continuum below 228 Å (Garnett et al. 1991; Guseva et al. 2000; Allen et al. 2008). Wolf–Rayet (WR) stars are capable of releasing photons able to produce He II λ4686. WR stars host stellar winds and can be a source of high-energy photons, $E > 54$ eV, capable of doubly ionizing Helium. We measured the He II λ4686/Hβ in H II regions with $T_{e,[O\,III]}$ detections and found that these regions exhibit an average He II λ4686/H$\beta = 4.1\% \pm 1.6\%$. This value is within the expected range of He II λ4686/Hβ values for H II regions with WR, 0.04%–7% (Guseva et al. 2000; Thuan & Izotov 2005; Mayya et al. 2023), and 100 km s^{-1} shocks, 4%–6% (Allen et al. 2008). We visually inspected the spectra of regions with measured $T_{e,[O\,III]}$ for the characteristic red/blue bump associated with the presence of WR stars. We found the

blue bump in only two regions with measurable [O III]λ4363, both of which have $T_{e,[O\,III]} < 10^4$ K. Nevertheless, the He II λ4686/Hβ for the high-$T_{e,[O\,III]}$ regions constitutes evidence that these regions may host shocks or undetected WR stars.

We also searched for kinematic signatures of shocks, but found no clear kinematic evidence. Shocks can imprint asymmetries and/or broad emission near the base of an emission line. We inspected the fit residuals of [O III]λ5007 in H II regions with measured $T_{e,[O\,III]}$ and found no evidence of line broadening due to shocks. Next, we inspected the measured line widths of [O III]λ5007 in these regions. We compared the line-spread function corrected [O III]λ5007, as measured by MUSE, velocity dispersion, $\sigma_{v,\lambda5007}$ versus the CO velocity dispersion, $\sigma_{v,CO}$. The line widths of the optical and CO emissions for regions with high $T_{e,[O\,III]}$ are comparable to those of regions with low or nondetected $T_{e,[O\,III]}$. Despite this, the absence of these features may only exclude the presence of high-velocity shocks.

If the regions do host low-velocity shocks, then their impact on the line width of the optical emission may be too small to be resolved, given the resolution of MUSE: $\sim$70 km s^{-1} at $\lambda = 5007$ Å. The high-velocity resolution, 2.5 km s^{-1}, of the PHANGS-ALMA data makes it more sensitive than MUSE to low-velocity shocks, and these data are the strongest evidence for the presence of such shocks in the high-$T_{e,[O\,III]}$ H II regions.

8. Discussion

8.1. Electron Density Inhomogeneities

Similar to the results of Méndez-Delgado et al. (2023b), described in Section 7.2, we have found that the presence of electron density inhomogeneities may cause the temperatures measured from [O II] and [S II] to be biased hotter compared to those measured using the [N II] auroral lines.

The critical densities of the nebular lines of [S II]$\lambda\lambda$6716, 6731 and more so [O II]$\lambda\lambda$3726, 3729 are low enough that, at densities $n_e > 10^3$ cm^{-3}, the lines will undergo increased collisional de-excitation. In the presence of density inhomogeneities above this value, the low critical densities will reduce the emissivity of the nebular emission lines from [S II] and [O II]. Because of this, the nebular diagnostic lines of [S II] and [O II] will mainly describe gas components with $n_e < 10^3$ cm^{-3}. This biases the [S II] and [O II] density diagnostic to return electron densities that are lower than the true average density of the H II region. Since the auroral-line critical densities are far higher, this also makes the measured [S II] and [O II] temperatures appear to reflect hotter values.

This effect has been observed in many studies. Densities measured in Milky Way H II regions (the Orion Nebula, NGC 3604, and NGC 3576) using [Cl III], which is sensitive to greater densities than [S II], routinely show that the [S II] diagnostic returns lower values than [Cl III]. (Pogge et al. 1992; García-Rojas & Esteban 2007; Núñez-Díaz et al. 2013; Weilbacher et al. 2015). Although densities derived from the [S II] doublet are commonly used in the literature, due to their strengths and their insensitivity to dust extinction, the [S II] λ6731/λ6716 ratio is less sensitive to density than [Cl III], [Ar IV], and [Fe III] diagnostics when $n_e > 10^3$ cm^{-3} (see Figure 2 in Méndez-Delgado et al. 2023b). If the equality $T_{e,[O\,II]} \approx T_{e,[S\,II]} \approx T_{e,[N\,II]}$ predicted by photoionization models is true, then the auroral-to-nebular line ratios would suggest a factor of 10 higher density than that of the [S II] doublet, but neither may represent well the true average density of the region.

Electron density variations may arise from shocks, turbulence, and pre-existing nonuniform structure in the ISM (Hill & Hollenbach 1978; Dopita & Sutherland 1996; Allen et al. 2008). Jin et al. (2022) have extended photoionization modeling of ionized nebulae to more complex geometries. Starting with an initial clumpy ISM, ionizing photons will pass through diffuse regions more readily than denser clumps. The resulting photoionized region will exhibit fluctuations in density and irregular geometry as opposed to a uniform density and spherical morphology. The ionization parameter in the dense clumps will be relatively lower than other regions of the nebulae, due to the increased density. At these locations, the emissions of low-ionization species, including [S II] and [O II], will be enhanced compared to those of higher-ionization species. Due to the higher critical densities of the auroral lines of these ions, the emissivities of the auroral lines will be greater than those of the nebular lines in the high-density portion of the nebula. In this scenario, the nebular density diagnostics can return an average density that traces the low-density portion of the nebula. In doing so, the value of n_e returned by the nebular diagnostics may inaccurately describe the ionizing conditions of the high-density clumps where the auroral-line emissivities are greater than the nebular lines, and thus it may overestimate [S II] temperatures.

Density inhomogeneities have been reported in studies of highly resolved local H II regions like Orion where the inhomogeneities can be spatially resolved (Baldwin et al. 1991; Pogge et al. 1992; Weilbacher et al. 2015; McLeod et al. 2016; O'Dell et al. 2017). Weilbacher et al. (2015) mapped the spatial variation of density in the Orion nebulae and found variations of density between 500 cm^{-3} and in excess of 10,000 cm^{-3}. A maximum of 25,000 cm^{-3} is measured using [Cl III] at the location of the ionization front in the "Orion S" area. Density inhomogeneities, associated with turbulence-driven velocity fluctuations, have been invoked as one mechanism to generate surface brightness fluctuations within the Orion Nebula (Kainulainen et al. 2017).

The Orion Nebula is not particularly comparable to the H II regions studied here, due to the difference in scales (i.e., Orion is more compact) and resolution. A subset of our H II regions, as shown in the comparison between the MUSE H II regions masked in Appendix C, are unresolved clusters of individual regions. Measurements of density inhomogeneities using density diagnostics besides the nebular [O II] and [S II] doublets for extragalactic H II regions that more closely match our sample are rare and require deep, high-S/N spectra (Méndez-Delgado et al. 2023b). One consequence of the lack of different diagnostics is that many studies will often assume a fixed density of 100 cm^{-3} when either [S II] or [O II] returns a density in the low-density limit (e.g., Kreckel et al. 2019). Studies using mid-infrared observations have shown this latter assumption could be incorrect, as densities up to 1000 cm^{-3} have been measured using the [S III]λ18.7/33.5 μm density diagnostic (see Rubin et al. 2016), indicating that density inhomogeneities are present in extragalactic H II regions.

The consistency of auroral-to-nebular ratios with $n_e \sim$ 1000 cm^{-3} assuming $T_e = T_{e,[N\,II]}$ in Figure 11, as well as the correlation between degree of inhomogeneities with Hβ surface brightness observed for [S II], supports this picture that

inhomogeneities must be considered when deriving temperatures from the [O II] and [S II]. As a result, we consider $T_{e,[N\,II]}$ a more reliable indicator of the low-ionization zone temperature, due to its relative insensitivity to density.

8.2. $T_{e,[N\,II]}$ and $T_{e,[S\,III]}$ as Accurate Tracers of H II Region Temperatures

Within the set of T_e–T_e between the low- and intermediate-ionization zones, we observed that the comparisons between $T_{e,[S\,III]}$–$T_{e,[O\,II]}$ and $T_{e,[S\,III]}$–$T_{e,[S\,II]}$ largely agree with those from Zurita et al. (2021). However, similarly to recent studies (Berg et al. 2015, 2020; Zurita et al. 2021; Rogers et al. 2021, 2022), we observed that the T_e–T_e trend between $T_{e,[N\,II]}$ and $T_{e,[S\,III]}$ exhibits the lowest scatter and agrees with many of the literature trends presented in Figure 9. These results suggest $T_{e,[N\,II]}$ and $T_{e,[S\,III]}$ temperatures are optimal tracers of H II region temperatures, more so than $T_{e,[S\,II]}$, $T_{e,[O\,II]}$, and $T_{e,[O\,III]}$.

Judged from the oxygen CEL and RL temperatures, the high-ionization zone is expected to be most affected by temperature fluctuations, due to its proximity to sources of feedback (Méndez-Delgado et al. 2023a). To what degree the intermediate-ionization zone temperatures are affected is unclear (Méndez-Delgado et al. 2023b). In Figure 9, we showed that our best-fit trends, including those from the literature, between $T_{e,[N\,II]}$ and $T_{e,[S\,III]}$ "generally" (within 2σ) follow trends predicted from the BOND photoionization models with temperature fluctuations set to zero. This suggests that $T_{e,[S\,III]}$ may be minimally affected by temperature inhomogeneities. Díaz & Zamora (2022) provide additional arguments for the use of $T_{e,[S\,III]}$ over $T_{e,[O\,III]}$, including the fact that (1) the emission lines of [S III] have a lower exponential dependence on electron temperature, and (2) because [S III] overlaps gas volumes containing both O^{2+} and O^{+}, the value of $T_{e,[S\,III]}$ can be representative of the entire H II region.

We also showed that $\Delta(T_{e,[N\,II]}, T_{e,[S\,III]})$ is stable around the zero line across the range of molecular gas velocity dispersion and the low values of the ionization parameter, traced by both [O III]/[O II] and [S III]/[S II], observed in this work. This result follows the observations of Berg et al. (2020), who find that agreement between these two temperature tracers becomes more uncertain in high-ionization parameter, traced by [O III]/[O II], H II regions. Due to the stable behavior of between $T_{e,[N\,II]}$ and $T_{e,[S\,III]}$ across the multiple H II region properties observed in this work, and following the suggestions of Berg et al. (2015, 2020) and Rogers et al. (2021), we will compare "direct" metallicities derived prioritizing [N II] and [S III] temperatures to several calibrated methods (R. Vaught et al. 2024, in preparation).

8.3. The High-ionization Zone Temperature Excess

Within the sample of H II regions with measured [O III] λ4363, there are a small number of H II regions with high $T_{e,[O\,III]}$, enhanced velocity dispersion in the surrounding molecular gas, and low ionization parameters. We investigated these H II regions for enhancements in the low-ionization species emission-line ratios [S II]/Hα and [O I]/Hα, as well as in the high-ionization ratio He II/Hβ. We found that the high-$T_{e,[O\,III]}$ regions exhibited enhanced low-ionization line ratios suggestive of shock ionization (or possibly X-ray ionization). We also found that the He II/Hβ ratios for these regions are within the range of those expected from shock velocities $<100\,\mathrm{km\,s^{-1}}$ (Allen et al. 2008) and/or WR stars (Guseva et al. 2000; Thuan & Izotov 2005; Mayya et al. 2023), though we only found the characteristic red/blue bumps associated with the presence of WR stars in two H II regions, neither of which had elevated $T_{e,[O\,III]}$. Absent the WR signatures, we are motivated to explore shocks as enhancers of the [O III] temperature.

We did not find any kinematic signatures of shocks in the optical emission-line profiles. We have determined that, if shocks are present and broadening the CO emission, then the shock velocities are too low to be resolved by the MUSE spectral resolution. Either way, high-velocity shocks are not expected to effectively boost $T_{e,[O\,III]}$ (Méndez-Delgado et al. 2021). Despite the uncertainty in whether shocks are present in the high [O III] temperature regions, we can discuss the plausibility that low-velocity shocks are the cause for excess $T_{e,[O\,III]}$.

8.3.1. Shock-enhanced [O III] Temperature

Low-velocity, $<100\,\mathrm{km\,s^{-1}}$, shocks can increase [O III] λ4363 while leaving [O III]λ5007 unchanged (Peimbert et al. 1991; Binette et al. 2012; Méndez-Delgado et al. 2021). For a sample of giant H II regions, Binette et al. (2012) measured $T_{e,[O\,III]}$ up to 6000 K higher than $T_{e,[S\,III]}$ in regions with $T_{e,[S\,III]} < 10^4$ K. To explore whether shocks were boosting their [O III] temperatures relative to [S III], they modeled outward-expanding shocks, mimicking those generated by stellar winds, by combining shock+photoionization models, with increasing shock velocities (analogous to increasing the post-shock temperature from 1.6×10^4 K to 7.2×10^4 K) between 20 and 60 $\mathrm{km\,s^{-1}}$. Additionally, the models span five different metallicities between $Z = 0.01\,Z_\odot$ and $Z = 1.6\,Z_\odot$. Comparing the average properties between the lowest and highest shock velocity models, Binette et al. (2012) found that the mean doubly ionized fraction of oxygen, O^{2+}/O, decreased while at the same time leaving the doubly ionized fraction of sulfur, S^{2+}/S, unchanged. The imbalance of the ionization fraction between oxygen and sulfur means that hotter, post-shock gas contributes proportionally more to the observed [O III] emission than [S III]. Because of the exponential sensitivity to temperature, the [O III] auroral line will be enhanced, tracing the hotter post-shock temperature rather than the local photoionized nebula temperature returned by $T_{e,[S\,III]}$. Furthermore, the highest-metallicity models show the largest temperature differences between $T_{e,[S\,III]}$ and $T_{e,[O\,III]}$, up to $\sim$7000 K. Although this difference is 3000 K lower than our largest measured $\Delta(T_{e,[S\,III]}, T_{e,[O\,III]})$, a complete understanding of the degree of enhancement of [O III]λ4363 with shocks will require more complex 3D hydrodynamical simulations (Binette et al. 2012). Despite this, one extreme example of shock impact on electron temperatures was observed in the outflow of the H II region Sh 2–129 (Corradi et al. 2014). This outflow, with velocity $\approx100\,\mathrm{km\,s^{-1}}$, exhibits $T_{e,[O\,III]} =$ 55,000 K and $T_{e,[O\,II]} \sim$ 20,000 K. These values are much larger than the ΔT_e observed in this study.

It has also been shown that shocks driven by the radiation pressure from H II region expansion, as well as supernova remnants, impact the surrounding cold molecular and ionized gas. If the velocity of the expansion is greater than the sound speed of the ionized gas, $\sim10\,\mathrm{km\,s^{-1}}$, a layer of shocked H gas will form in between the expanding ionization front and a surrounding

molecular gas (Hill & Hollenbach 1978; Kothes & Kerton 2002; Tremblin et al. 2014; Watkins et al. 2023). The impact of shock interaction with molecular gas has been studied in 18 galaxies observed as part of PHANGS-ALMA (Leroy et al. 2021a, 2021b), where Watkins et al. (2023) identified hundreds of superbubbles (i.e., pockets of expanding gas arising as byproducts of feedback). The superbubbles were identified using spatial correspondence between CO shells and stellar populations contained in PHANGS-HST catalogs (Lee et al. 2022; Thilker et al. 2022; Larson et al. 2023). Due to the ALMA spatial resolution (50–150 pc), Watkins et al. (2023) measured the expansion velocity only for the largest superbubbles. Assuming the CO expansion velocity is equal to the shock velocity, Watkins et al. (2023) measure the velocity of the approaching/receding CO shells and determine an average line-of-sight expansion velocity of $v_{\rm exp} = 9.8 \pm 4.3$ km s^{-1}. Although this value is similar to the sound speed of the ionized gas, superbubbles exhibit asymmetries in their morphology, and the velocity can potentially reach up to a few tens of km s^{-1} depending on the conditions of the gas, source or energy injection, and age (Watkins et al. 2023). One-dimensional models indicate that, at minimum, H II regions exhibit expansion speeds of a $\sim$few km s^{-1} (Tremblin et al. 2014). This suggests that H II regions expand with a large range of velocities.

As for ionized gas, Egorov et al. (2023) identify in the PHANGS-MUSE galaxies more than 1400 regions of ionized gas with elevated intrinsic Hα velocity dispersions $>$45 km s^{-1}, and under the assumption that these regions are undergoing expansion, Egorov et al. (2023) infer expansion velocities between $v_{\rm exp} = 10$–40 km s^{-1} (see also Egorov et al. 2014, 2017; Cosens et al. 2022). The ubiquity of H II region expansion, as well as its effects on the surrounding molecular gas, makes it a good candidate to be a driver of low-velocity shocks capable of boosting [O III] temperatures.

8.3.2. Temperature Inhomogeneities

Temperature fluctuations within H II regions are another potential explanation for the high [O III] temperature. As discussed in Section 1, RL emissivities have a linear sensitivity to temperature, rather than the exponential sensitivity of CELs. In the presence of temperature fluctuations, CELs will return higher estimates of temperature. Méndez-Delgado et al. (2023a) have recently shown that differences between [O III] and [N II] temperatures are strongly correlated with the temperature fluctuation parameter, t^2, of the highly ionized gas. This suggests that $T_{\rm e,[O\,III]}$ is likely to overestimate the representative H II region temperature. The observed excesses in $T_{\rm e,[O\,III]}$ are likely to be produced by phenomena other than those commonly observed in H II regions. Simple models from Binette et al. (2012) and the observations from Méndez-Delgado et al. (2023a) show that the effect from $t^2 > 0$ is more pronounced in lower-metallicity/high-ionization-parameter regions. Furthermore, the temperature excess of $T_{\rm e,[O\,III]}$ relative to the other ionization zones is too large in our observations to be caused solely by inhomogeneities. Using our measured $\Delta(T_{\rm e,[N\,II]}, T_{\rm e,[O\,III]})$, we can infer from Méndez-Delgado et al. (2023a) that $t^2 > 0.2$ for $\Delta(T_{\rm e,[N\,II]}, T_{\rm e,[O\,III]}) > 5000$ K. These values are much higher than what has been observed in nearby H II regions (Binette et al. 2012; Peña-Guerrero et al. 2012; Méndez-Delgado et al. 2023a). Even in the presence of classical temperature inhomogeneities, a secondary effect would also need to be included to explain our [O III] temperatures.

8.3.3. Potential Observation Bias

Another possibility is that the high [O III] temperatures are statistical outliers. The galaxies in our sample exhibit strong line oxygen abundances $\gtrsim$8.3 (Kreckel et al. 2019). Because electron temperature is anticorrelated with the metallicity of the gas, the [O III]λ4363 temperatures for these galaxies are expected to be low. For [O III]λ4363 to be detectable, the temperature would need to be high; otherwise, we would likely not detect the auroral line. [O III] temperatures from a lower-metallicity sample may be compatible with photoionization models and $T_{\rm e}$–$T_{\rm e}$ relations. Finally, Rola & Pelat (1994) have shown that emission-line measurements with S/N $<$ 5 can potentially overestimate the true intensity by 80%. The average S/N [O III]λ4363 measured from our sample is $\sim$4.5. Nevertheless, why we would measure high [O III]λ4363, even after removal of [Fe II]λ4360 contamination, in regions that also exhibit enhanced molecular gas velocity dispersions is difficult to explain purely with statistical outliers.

9. Conclusions

We presented combined KCWI and MUSE observations of the [N II]λ5756, [O II]$\lambda\lambda$7320, 7330, [S II]$\lambda\lambda$4069, 4076, [O III]λ4363, and [S III]λ6312 auroral lines in a sample of 421 H II regions in seven nearby galaxies. We compared the derived electron temperatures and temperature differences between multiple H II region ionization zones to several H II region properties such as electron density, ionization parameter, molecular gas velocity dispersion, stellar mass, and age obtained from PHANGS observations. We found that:

1. Similar to the results from Méndez-Delgado et al. (2023b), temperatures obtained from [S II] and [O II] are consistent with being overestimated due to the presence of density inhomogeneities in the H II regions. Because of these potential biases, we recommend the use of [N II] temperatures to trace the low-ionization zone.
2. In addition to previous studies: Berg et al. (2015, 2020), Rogers et al. (2021), and Zurita et al. (2021), we found that the [N II] and [S III] temperatures exhibited the lowest scatter of the $T_{\rm e}$–$T_{\rm e}$ relations and follow trends predicted from photoionization models. The well-behaved relationship between [N II] and [S III], even in potentially inhomogeneous conditions, may be better tracing the underlying H II region temperatures. This result and those from the above studies further stress the prioritization of [N II] and [S III] temperatures for metallicity determinations.
3. We observed a subset of H II regions with high [O III] temperatures that do not agree with the cooler temperatures measured in the low- and intermediate-ionization zones. We found that the regions with high [O III] temperature tended to have enhanced molecular gas velocity dispersion and lower ionization parameter than those regions with [O III] temperatures that were in better agreement with other ionization zones. These regions also showed enhanced [S II]/Hα, [O I]/Hα, and He II/Hβ ratios indicating the presence of secondary ionization sources (e.g., shocks, Wolf–Rayet stars, and X-ray binary stars). Absent direct detection of shocks, we explored

whether or not shocks are able to both enhance $T_{e,[O\,III]}$ and CO velocity dispersion. We found that low-velocity shocks are a plausible explanation for the observed [O III] temperatures and CO velocity dispersions. However, disentangling the effects of shocks from possible contributions to [O III] temperatures by harder ionization sources such as Wolf–Rayet stars or X-ray binaries will require further investigation.

4. We also explored temperature inhomogeneities and observational uncertainties as causes for high [O III] temperatures measured for a small subsample of H II regions. We found that the degree of temperature inhomogeneity that would be required to produce the difference between high [O III] temperatures and those of the low- and intermediate-ionization zones are larger than what has been observed in most star-forming regions. Furthermore, if the regions with high [O III] temperatures are statistical outliers leading to overestimated temperatures, we lack an explanation as to why these temperatures would correlate with high molecular gas velocity dispersion.

In a follow-up paper, R. Vaught et al. (2024, in preparation), we will test temperature recommendations for measuring "direct" metallicities using our full set of measured auroral-line temperatures. This work, along with the PHANGS-MUSE survey, will demonstrate the power of integral field spectrographs on 10 m class telescopes for measuring faint auroral emission lines from large samples of H II regions in nearby galaxies. Future efforts with deeper observations or expanded samples will be critical for further elucidating the temperature and ionization behavior of these regions, in particular as [O III] λ4363 and other faint lines are now being routinely detected in galaxies at high redshift with JWST and used in metallicity determinations.

Acknowledgments

The authors thank the referee for a very thorough report that significantly improved the analysis presented here. The data presented herein were obtained at the W. M. Keck Observatory, which is operated as a scientific partnership among the California Institute of Technology, the University of California, and the National Aeronautics and Space Administration. The Observatory was made possible by the generous financial support of the W. M. Keck Foundation. The authors wish to recognize and acknowledge the very significant cultural role and reverence that the summit of Maunakea has always had within the indigenous Hawaiian community. We are most fortunate to have the opportunity to conduct observations from this mountain. We also wish to thank all of the Keck Observatory staff, including Gregg Doppman, Luca Rizzi, Sheery Yeh, and Rosalie McGurk for observational support.

This research is also based on observations collected at the European Southern Observatory under ESO programmes 094.C-0623 (PI: Kreckel), 095.C-0473, 098.C-0484 (PI: Blanc), 1100.B-0651 (PHANGS-MUSE; PI: Schinnerer), as well as 094.B-0321 (MAGNUM; PI: Marconi), 099.B-0242, 0100.B-0116, 098.B-0551 (MAD; PI: Carollo), and 097.B-0640 (TIMER; PI: Gadotti).

R.R.V. and K.S. acknowledge funding support from National Science Foundation Award No. 1816462. F.B. acknowledges funding from the INAF Fundamental Astrophysics 2022 program. R.R.V. wishes to thank Jonah Gannon, and Maren Consens for fruitful discussions on reducing the KCWI data. R.R.V. would also like to acknowledge discussions with J.E.M.-D., K.K., and O.V.E. that greatly improved the manuscript. K.K., J.E.M.-D., and O.V.E. gratefully acknowledge funding from the Deutsche Forschungsgemeinschaft (DFG, German Research Foundation) in the form of an Emmy Noether Research Group (grant No. KR4598/2-1, PI Kreckel). K.G. is supported by the Australian Research Council through the Discovery Early Career Researcher Award (DECRA) Fellowship (project number DE220100766) funded by the Australian Government. K.G. is supported by the Australian Research Council Centre of Excellence for All Sky Astrophysics in 3 Dimensions (ASTRO 3D), through project number CE170100013. J.N. acknowledges funding from the European Research Council (ERC) under the European Union's Horizon 2020 research and innovation program (grant agreement No. 694343). R.S.K. acknowledges funding from the European Research Council via the ERC Synergy Grant "ECOGAL" (project ID 855130), from the German Excellence Strategy via the Heidelberg Cluster of Excellence (EXC 2181-390900948) "STRUCTURES," and from the German Ministry for Economic Affairs and Climate Action in project "MAINN" (funding ID 50OO2206). He also thanks for computing resources provided by *The Länd* and DFG through grant INST 35/1134-1 FUGG and for data storage at SDS@hd through grant INST 35/1314-1 FUGG. G.A.B. acknowledges the support from the ANID Basal project FB210003.

This research made use of Montage. It is funded by the National Science Foundation under grant No. ACI-1440620, and was previously funded by the National Aeronautics and Space Administration's Earth Science Technology Office, Computation Technologies Project, under Cooperative Agreement Number NCC5-626 between NASA and the California Institute of Technology. This research has made use of NASA's Astrophysics Data System. This research made use of Astropy, a community-developed core Python package for Astronomy (Astropy Collaboration et al. 2013), as well as substantial use of the nebular diagnostics toolkit Pyneb (Luridiana et al. 2015).

The distances in Table 1 were compiled by Anand et al. (2021) and are based on Freedman et al. (2001), Nugent et al. (2006), Jacobs et al. (2009), Kourkchi & Tully (2017), Shaya et al. (2017), Kourkchi et al. (2020), Anand et al. (2021), and Scheuermann et al. (2022).

Appendix A
KCWI Seeing FWHM from Standard Star Observations and Table of Observations

We summarize the details of all of the KCWI observations and standard star observations in Tables 6 and 7. Additionally, we describe below the measurement of seeing from the set of standard stars.

To measure seeing, we fit a 2D Gaussian to each standard star observation. We find an average FWHM of $\sim 1\farcs2$; however, at some points during the nights of 2018 October 17, 2019 March 27, and 2019 March 28, the seeing was poorer, with values between $1\farcs6$ and $2''$. Aside from these portions of the nights, the seeing was stable near the average FWHM. The FWHM measurements for each standard star observation are summarized in Table 7.

Table 6
Summary of KCWI Observations

Field[a]	R.A. (deg)	R.A.$_{corr}$[b] (arcsec)	Decl. (deg)	Decl.$_{corr}$[b] (arcsec)	Date (UTC)	Exposure (s)	Airmass	PA (deg)	FWHM[c] (arcsec)
NGC0628F17	24.188826	0.16	15.771491	−1.75	2018-10-17T07:00:46	1200.0	1.46	45.0	2.14
NGC0628F17	24.189230	−1.30	15.771380	−1.35	2018-10-17T07:35:05	1200.0	1.28	45.0	1.79
NGC0628F17	24.189230	−1.30	15.771380	−1.35	2018-10-17T07:56:17	1200.0	1.20	45.0	1.97
NGC0628F18	24.189057	−0.68	15.771546	−1.95	2018-10-17T08:29:45	1200.0	1.11	45.0	2.49
NGC0628F18	24.188941	−0.26	15.771657	−2.35	2018-10-17T08:51:03	1200.0	1.07	45.0	2.49
NGC0628F22	24.189576	−2.55	15.771268	−0.95	2018-10-17T09:29:26	1200.0	1.02	45.0	2.20
NGC0628F22	24.189461	−2.13	15.771380	−1.35	2018-10-17T09:50:42	1200.0	1.01	45.0	2.49
NGC0628F23	24.189519	−2.34	15.770380	2.25	2018-10-17T10:24:20	1200.0	1.00	45.0	1.49
NGC0628F23	24.189634	−2.75	15.770324	2.45	2018-10-17T10:45:51	1200.0	1.01	45.0	1.60
NGC0628F04	24.190558	−6.08	15.770213	2.85	2018-10-16T10:08:04	1200.0	1.00	45.0	2.48
NGC1087F10	41.606106	−1.05	−0.494058	−0.15	2018-10-17T11:23:24	1200.0	1.07	90.0	1.26
NGC1087F10	41.606106	−1.05	−0.494058	−0.15	2018-10-17T11:44:36	1200.0	1.07	90.0	1.29
NGC1087F09	41.605773	0.15	−0.494446	1.25	2018-10-17T12:17:46	1200.0	1.09	90.0	1.19
NGC1087F09	41.605773	0.15	−0.494391	1.05	2018-10-17T12:38:58	1200.0	1.12	90.0	1.15
NGC1087F08	41.605884	−0.25	−0.494391	1.05	2018-10-17T13:12:00	1200.0	1.19	90.0	1.16
NGC1087F08	41.605884	−0.25	−0.494446	1.25	2018-10-17T13:33:09	1200.0	1.25	90.0	1.27
NGC1087F04	41.606050	−0.85	−0.494169	0.25	2018-10-17T14:06:31	1200.0	1.39	90.0	1.21
NGC1087F04	41.606050	−0.85	−0.494113	0.05	2018-10-17T14:27:51	1200.0	1.52	90.0	1.31
NGC1087F11	41.605884	−0.25	−0.494391	1.05	2018-10-16T13:30:01	1200.0	1.23	90.0	1.24
NGC1087F11	41.605773	0.15	−0.494391	1.05	2018-10-16T13:08:26	1200.0	1.17	90.0	1.16
NGC1087F12	41.606939	−4.05	−0.495113	3.65	2018-10-16T11:36:44	1200.0	1.07	90.0	1.07
NGC1087F12	41.606050	−0.85	−0.494724	2.25	2018-10-16T12:11:21	1200.0	1.08	90.0	1.19
NGC1087F12	41.606050	−0.85	−0.494669	2.05	2018-10-16T12:32:55	1200.0	1.11	90.0	1.19
NGC1300F1	49.903140	−2.39	−19.400675	1.25	2021-10-07T10:58:14	1200.0	1.44	90.0	1.14
NGC1300F1	49.903140	−2.39	−19.400786	1.65	2021-10-07T11:19:16	1200.0	1.38	90.0	1.50
NGC1300F2	49.903022	−1.96	−19.401008	2.45	2021-10-07T11:52:07	1200.0	1.32	90.0	1.14
NGC1300F2	49.903022	−1.96	−19.400953	2.25	2021-10-07T12:13:05	1200.0	1.30	90.0	1.33
NGC1300F3	49.902963	−1.75	−19.401619	4.65	2021-10-07T12:45:25	1200.0	1.29	90.0	1.34
NGC1300F3	49.902963	−1.75	−19.401508	4.25	2021-10-07T13:06:26	1200.0	1.30	90.0	1.20
NGC1300F4	49.903788	−4.72	−19.401341	3.65	2021-10-07T13:42:40	1200.0	1.35	90.0	1.04
NGC1300F4	49.903729	−4.51	−19.401341	3.65	2021-10-07T14:03:37	1200.0	1.40	90.0	1.03
NGC1300F5	49.903611	−4.08	−19.401730	5.05	2021-10-07T14:36:25	1200.0	1.51	0.0	1.33
NGC1300F5	49.903552	−3.87	−19.401730	5.05	2021-10-07T14:57:23	1200.0	1.62	0.0	1.34
NGC1385F1	54.372099	−2.25	−24.496321	1.65	2021-10-06T10:52:05	1200.0	1.70	90.0	1.52
NGC1385F1	54.372099	−2.25	−24.496321	1.65	2021-10-06T11:13:46	1200.0	1.59	90.0	1.43
NGC1385F2	54.372038	−2.03	−24.496265	1.45	2021-10-06T11:50:22	1200.0	1.47	90.0	1.26
NGC1385F2	54.372038	−2.03	−24.496321	1.65	2021-10-06T12:11:22	1200.0	1.43	90.0	1.20
NGC1385F3	54.371916	−1.59	−24.496432	2.05	2021-10-06T12:44:09	1200.0	1.40	90.0	1.06
NGC1385F3	54.371916	−1.59	−24.496487	2.25	2021-10-06T13:05:09	1200.0	1.39	90.0	1.35
NGC1385F4	54.371794	−1.15	−24.496265	1.45	2021-10-06T13:38:12	1200.0	1.42	90.0	1.16
NGC1385F4	54.371794	−1.15	−24.496265	1.45	2021-10-06T13:59:12	1200.0	1.45	90.0	1.06
NGC1385F5	54.371611	−0.49	−24.495710	−0.55	2021-10-06T14:41:06	1200.0	1.57	0.0	1.21
NGC2835F1	139.471355	−3.51	−22.341874	0.05	2019-03-27T05:57:41	1200.0	1.47	90.0	1.42
NGC2835F1	139.471355	−3.51	−22.341874	0.05	2019-03-27T06:18:44	1200.0	1.42	90.0	1.52
NGC2835F2	139.471475	−3.95	−22.342430	2.05	2019-03-27T06:52:51	1200.0	1.36	90.0	1.51
NGC2835F2	139.471475	−3.95	−22.342430	2.05	2019-03-27T07:13:56	1200.0	1.35	90.0	1.42
NGC2835F3	139.471114	−2.65	−22.342874	3.65	2019-03-27T07:47:08	1200.0	1.36	90.0	1.39
NGC2835F3	139.471054	−2.43	−22.342874	3.65	2019-03-27T08:08:11	1200.0	1.38	90.0	1.52
NGC2835F4	139.470694	−1.14	−22.343041	4.25	2019-03-27T08:42:01	1200.0	1.45	90.0	1.26
NGC2835F4	139.470634	−0.92	−22.342985	4.05	2019-03-27T09:03:11	1200.0	1.51	90.0	1.17
NGC3627F1	170.056873	−2.92	12.998914	1.45	2017-12-24T12:43:33	120.0	1.32	90.0	1.27
NGC3627F1	170.056873	−2.92	12.998858	1.65	2017-12-24T12:46:31	120.0	1.30	90.0	1.27
NGC3627F1	170.056873	−2.92	12.998858	1.65	2017-12-24T12:49:28	120.0	1.29	90.0	1.26
NGC3627F1	170.056873	−2.92	12.998858	1.65	2017-12-24T12:52:26	120.0	1.28	90.0	1.27
NGC3627F1	170.056873	−2.92	12.998858	1.65	2017-12-24T12:55:24	120.0	1.26	90.0	1.27
NGC3627F1	170.056132	−0.26	12.999192	0.45	2017-12-24T15:33:08	120.0	1.01	90.0	1.16
NGC3627F1	170.056132	−0.26	12.999192	0.45	2017-12-24T15:36:06	120.0	1.01	90.0	1.22
NGC3627F1	170.056132	−0.26	12.999192	0.45	2017-12-24T15:39:04	120.0	1.01	90.0	1.21
NGC3627F1	170.056132	−0.26	12.999192	0.45	2017-12-24T15:42:02	120.0	1.01	90.0	1.20
NGC3627F2	170.057215	−4.16	12.998747	2.05	2017-12-24T13:02:38	120.0	1.24	90.0	1.21
NGC3627F2	170.057215	−4.16	12.998747	2.05	2017-12-24T13:05:35	120.0	1.23	90.0	1.23
NGC3627F2	170.057215	−4.16	12.998747	2.05	2017-12-24T13:08:33	120.0	1.22	90.0	1.22
NGC3627F2	170.057215	−4.16	12.998747	2.05	2017-12-24T13:11:31	120.0	1.21	90.0	1.19
NGC3627F2	170.057215	−4.16	12.998747	2.05	2017-12-24T13:14:29	120.0	1.20	90.0	1.23
NGC3627F3	170.057215	−4.16	12.998747	2.05	2017-12-24T13:20:54	120.0	1.18	90.0	1.13
NGC3627F3	170.057215	−4.16	12.998747	2.05	2017-12-24T13:23:52	120.0	1.17	90.0	1.12
NGC3627F3	170.057215	−4.16	12.998747	2.05	2017-12-24T13:26:50	120.0	1.16	90.0	1.12

Table 6
(Continued)

Field[a]	R.A. (deg)	R.A.$_{corr}$[b] (arcsec)	Decl. (deg)	Decl.$_{corr}$[b] (arcsec)	Date (UTC)	Exposure (s)	Airmass	PA (deg)	FWHM[c] (arcsec)
NGC3627F3	170.057215	−4.16	12.998747	2.05	2017-12-24T13:29:48	120.0	1.15	90.0	1.12
NGC3627F3	170.057215	−4.16	12.998747	2.05	2017-12-24T13:32:45	120.0	1.14	90.0	1.14
NGC3627F4	170.057215	−4.16	12.998580	2.65	2017-12-24T13:40:31	120.0	1.12	90.0	1.14
NGC3627F4	170.057215	−4.16	12.998580	2.65	2017-12-24T13:43:29	120.0	1.12	90.0	1.14
NGC3627F4	170.057215	−4.16	12.998580	2.65	2017-12-24T13:46:27	120.0	1.11	90.0	1.14
NGC3627F4	170.057215	−4.16	12.998580	2.65	2017-12-24T13:49:25	120.0	1.10	90.0	1.15
NGC3627F4	170.057215	−4.16	12.998580	2.65	2017-12-24T13:52:23	120.0	1.10	90.0	1.15
NGC3627F5	170.057215	−4.16	12.998525	2.85	2017-12-24T13:58:52	120.0	1.09	90.0	1.06
NGC3627F5	170.057158	−3.95	12.998525	2.85	2017-12-24T14:01:50	120.0	1.08	90.0	1.07
NGC3627F5	170.057158	−3.95	12.998525	2.85	2017-12-24T14:04:48	120.0	1.08	90.0	1.07
NGC3627F5	170.057158	−3.95	12.998525	2.85	2017-12-24T14:07:46	120.0	1.07	90.0	1.07
NGC3627F5	170.057158	−3.95	12.998525	2.85	2017-12-24T14:10:44	120.0	1.07	90.0	1.07
NGC3627F6	170.056246	−0.67	12.999136	0.65	2017-12-24T14:24:16	120.0	1.05	90.0	1.12
NGC3627F6	170.056189	−0.46	12.999136	0.65	2017-12-24T14:27:14	120.0	1.04	90.0	1.15
NGC3627F6	170.056189	−0.46	12.999136	0.65	2017-12-24T14:30:11	120.0	1.04	90.0	1.17
NGC3627F6	170.056189	−0.46	12.999136	0.65	2017-12-24T14:33:10	120.0	1.04	90.0	1.17
NGC3627F6	170.056189	−0.46	12.999136	0.65	2017-12-24T14:36:07	120.0	1.03	90.0	1.15
NGC3627F7	170.056303	−0.87	12.999136	0.65	2017-12-24T14:42:14	120.0	1.03	90.0	1.16
NGC3627F7	170.056303	−0.87	12.999136	0.65	2017-12-24T14:45:11	120.0	1.03	90.0	1.16
NGC3627F7	170.056303	−0.87	12.999136	0.65	2017-12-24T14:48:09	120.0	1.02	90.0	1.17
NGC3627F7	170.056303	−0.87	12.999136	0.65	2017-12-24T14:51:07	120.0	1.02	90.0	1.18
NGC3627F7	170.056303	−0.87	12.999136	0.65	2017-12-24T14:54:05	120.0	1.02	90.0	1.20
NGC3627F8	170.056303	−0.87	12.998914	1.45	2017-12-24T15:00:09	120.0	1.02	90.0	1.05
NGC3627F8	170.056303	−0.87	12.998914	1.45	2017-12-24T15:03:07	120.0	1.01	90.0	1.05
NGC3627F8	170.056246	−0.67	12.998914	1.45	2017-12-24T15:06:05	120.0	1.01	90.0	1.05
NGC3627F8	170.056246	−0.67	12.998914	1.45	2017-12-24T15:09:03	120.0	1.01	90.0	1.06
NGC3627F8	170.056246	−0.67	12.998914	1.45	2017-12-24T15:12:00	120.0	1.01	90.0	1.05
NGC3627F9	170.056018	0.15	12.998803	1.85	2017-12-24T15:15:05	120.0	1.01	90.0	1.12
NGC3627F9	170.056018	0.15	12.998803	1.85	2017-12-24T15:18:03	120.0	1.01	90.0	1.12
NGC3627F9	170.056018	0.15	12.998803	1.85	2017-12-24T15:21:01	120.0	1.01	90.0	1.12
NGC3627F9	170.056018	0.15	12.998803	1.85	2017-12-24T15:23:59	120.0	1.01	90.0	1.11
NGC3627F9	170.056018	0.15	12.998803	1.85	2017-12-24T15:26:57	120.0	1.01	90.0	1.11
NGC5068F1	199.704057	−2.20	−21.023638	0.85	2019-03-27T09:49:19	1200.0	1.47	90.0	1.51
NGC5068F1	199.704057	−2.20	−21.023694	1.05	2019-03-27T10:10:22	1200.0	1.41	90.0	1.33
NGC5068F2	199.703819	−1.34	−21.023638	0.85	2019-03-27T10:44:05	1200.0	1.35	90.0	1.40
NGC5068F3	199.703938	−1.77	−21.023971	2.05	2019-03-27T11:38:24	1200.0	1.32	90.0	2.49
NGC5068F3	199.703938	−1.77	−21.023971	2.05	2019-03-27T11:59:28	1200.0	1.34	90.0	2.49
NGC5068F4	199.703700	−0.91	−21.024138	2.65	2019-03-27T12:32:51	1200.0	1.39	90.0	1.55
NGC5068F4	199.703700	−0.91	−21.024194	2.85	2019-03-27T12:53:55	1200.0	1.45	90.0	1.88
NGC5068F5	199.703403	0.16	−21.023860	1.65	2019-03-27T13:28:21	1200.0	1.58	90.0	1.97
NGC5068F5	199.703998	−1.98	−21.023694	1.05	2019-03-28T10:19:33	1200.0	1.38	90.0	1.69
NGC5068F7	199.704057	−2.20	−21.023694	1.05	2019-03-28T10:54:58	1200.0	1.33	90.0	1.68
NGC5068F7	199.703998	−1.98	−21.023694	1.05	2019-03-28T11:16:01	1200.0	1.32	90.0	1.67
NGC5068F8	199.703879	−1.55	−21.024082	2.45	2019-03-28T11:49:43	1200.0	1.33	90.0	1.86
NGC5068F8	199.703819	−1.34	−21.024027	2.25	2019-03-28T12:10:49	1200.0	1.36	90.0	1.87
NGC5068F9	199.703403	0.16	−21.024138	2.65	2019-03-28T12:44:48	1200.0	1.43	90.0	1.67
NGC5068F9	199.703343	0.37	−21.024138	2.65	2019-03-28T13:05:52	1200.0	1.50	90.0	1.65
NGC5068F9	199.703700	−0.91	−21.023138	−0.95	2022-02-24T14:57:54	1200.0	1.46	0.0	1.39
NGC5068F9	199.703641	−0.70	−21.023138	−0.95	2022-02-24T15:08:56	600.0	1.50	0.0	1.46
NGC5068F10	199.703700	−0.91	−21.023527	0.45	2022-02-24T15:30:23	800.0	1.59	90.0	1.17
NGC5068F10	199.703700	−0.91	−21.023471	0.25	2022-02-24T15:38:22	420.0	1.63	90.0	1.13

Notes. This table reports the galaxy and the field observed (Field). The repeated fields are offset by 1/2 slice width, with the exception of all of the fields in NGC 3627. The table also reports: the original coordinates of the field center in R.A. and decl. (R.A., decl.), the applied astrometric correction in R.A. and decl. (R.A.$_{corr}$, decl.$_{corr}$) determined from the image registration, the UTC start time and total integration of the exposure in seconds (Date, Exposure), and the airmass (Airmass), position angle (Angle), and angular FWHM of the pointing.

[a] The field numbering is from internal lists of potential pointings that were not performed in numerical order, therefore the field number does not reflect the sequence of observations.

[b] The astrometric correction is described in Section 3.2.

[c] The measured angular FWHM for the pointing; see Section 3.4.

Table 7
Summary of KCWI Standard Star Observations

Star[a]	R.A.	Decl.	Date (UTC)	Exposure (s)	Airmass	FWHM[b] (arcsec)
He3	06:47:37.99	+37:30:57.1	2018-10-16T15:00:13	20.0	1.06	1.32
Feige15	01:49:09.49	+13:33:11.7	2018-10-17T09:04:57	10.0	1.07	1.69
Feige15	01:49:09.49	+13:33:11.7	2018-10-17T09:06:11	1.0	1.07	1.12
Feige15	01:49:09.49	+13:33:11.7	2018-10-16T10:44:02	10.0	1.01	1.04
Feige34	10:39:36.71	+43:06:10.1	2019-03-27T09:21:06	5.0	1.10	1.28
Feige34	10:39:36.71	+43:06:10.1	2019-03-27T09:22:26	1.0	1.10	1.21
Feige66	12:37:23.52	+25:03:59.3	2019-03-27T13:45:25	1.0	1.35	1.99
Feige66	12:37:23.52	+25:03:59.3	2019-03-28T13:19:36	1.0	1.26	1.83
Feige66	12:37:23.52	+25:03:59.3	2019-03-28T13:20:57	5.0	1.26	1.83
GD50	03:48:50.31	−00:58:35.8	2021-10-06T10:17:51	1.0	1.47	1.13
GD50	03:48:50.31	−00:58:35.8	2021-10-06T10:19:37	1.0	1.46	1.13
GD50	03:48:50.31	−00:58:35.8	2021-10-06T10:20:53	10.0	1.45	1.18
GD50	03:48:50.31	−00:58:35.8	2021-10-06T10:22:37	15.0	1.44	1.22
GD50	03:48:50.31	−00:58:35.8	2021-10-06T14:13:09	10.0	1.11	1.01
GD50	03:48:50.31	−00:58:35.8	2021-10-06T14:14:54	15.0	1.11	1.04
GD50	03:48:50.31	−00:58:35.8	2021-10-06T14:16:28	1.0	1.11	1.06
GD50	03:48:50.31	−00:58:35.8	2021-10-07T10:29:40	1.0	1.38	1.07
GD50	03:48:50.31	−00:58:35.8	2021-10-07T10:30:56	10.0	1.38	1.11
GD50	03:48:50.31	−00:58:35.8	2021-10-07T10:32:17	15.0	1.37	1.10
GD50	03:48:50.31	−00:58:35.8	2021-10-07T13:19:16	10.0	1.07	1.11
GD50	03:48:50.31	−00:58:35.8	2021-10-07T13:20:43	15.0	1.07	1.18

Notes.
[a] The name of each standard star as displayed in the KDRP list of standards.
[b] The angular FWHM was measured from a 2D Gaussian fit to a white-light image of the standard star.

Appendix B
KCWI Line-spread Function

The KCWI line-spread function in the large slicer is non-Gaussian. Deviations from a Gaussian profile have been observed in KCWI data before. For example, van Dokkum et al. (2019) did so by using a combination of the medium slicer and grating. Following van der Marel & Franx (1993), in order to parameterize the degree of deviation from a Gaussian profile, we fit the spectra from a pipeline-reduced arc lamp exposure by means of a Gauss–Hermite function of the form:

$$G(X) = \frac{\gamma}{\sigma\sqrt{2\pi}} \exp(-X^2/2) \times \left[1 + \ldots h_3 \frac{X(2X^2-3)}{\sqrt{3}} + h_4 \frac{4(X^2-3)X^2+3}{\sqrt{24}}\right], \quad \text{(B1)}$$

with $X = (\lambda - \lambda_0)/\sigma$, amplitude ($\gamma$), and spectral width ($\sigma$). The antisymmetric and symmetric deviations from pure Gaussian profiles are captured by the constants, h_3 and h_4. A Gaussian function is recovered by setting $h_3 = h_4 = 0$. In Figure 19, we show histograms of the fitted values from h_3 and h_4 after fitting Equation (B1) to approximately 20 isolated arc lamp emission lines. We find that the emission lines in the arc lamp images are consistently flat-topped, with an average value of $h_4 = -0.14 \pm 0.01$ across all spatial pixels. The degree to which the line profile is non-Gaussian due to asymmetric deviations is small compared to symmetric deviations with an average value of $h_3 = -0.007 \pm 0.01$.

The authors state that the root cause of the deviation from a Gaussian profile is due to the slit-width-limited resolution of the medium slicer (see Casini & de Wijn 2014). We posit that a

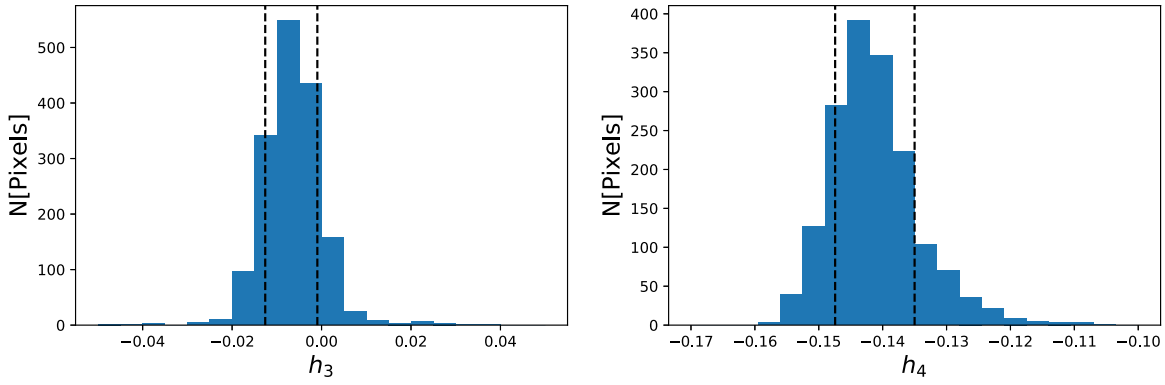

Figure 19. Histograms of the Gauss–Hermite parameters h_3, shown in the left panel, and h_4, shown in the right panel. The above histograms show the distribution of values for the fitted constants h_3 (antisymmetric) and h_4 (symmetric) from all pixels in the data cube. A Gaussian profile would exhibit $h_3 = h_4 = 0$; however, the above distributions show that the line profile of the instrument exhibits symmetric deviations. The broken black vertical lines represent the position of $\pm 1\sigma$.

similar limitation for the large slicer is responsible for the deviations measured in this work.

Appendix C
Comparison of H II Region Identification between KCWI and MUSE

We identify potential H II regions with Hβ emission maps constructed from the KCWI galaxy mosaics using `HIIPhot`. H II regions, for the same galaxies, in the PHANGS Nebular Catalog were identified with `HIIPhot` and MUSE Hα maps (Kreckel et al. 2019; Groves et al. 2023). Given the higher resolution of the MUSE imaging, as well as the threefold brightness increase of Hα relative to Hβ, we expect our H II region catalog to be less sensitive to the faintest and smallest H II regions.

In Figure 20, we show both the distribution of dust-corrected Hβ luminosity, $L_{\mathrm{H}\beta}$, and radii, for regions identified by *HIIPhot* using KCWI Hβ maps, "KCWI–Hβ regions,". We also include regions identified in MUSE Hα maps or "MUSE–Hα regions" that lie within the KCWI mosaic footprint. For KCWI–Hβ regions, we measure a median $\mathrm{Log}_{10}(L_{\mathrm{H}\beta}/[\mathrm{erg\ s^{-1}}])$ of $37.7^{+0.9}_{-0.7}$, while for MUSE–Hα regions, the median is $37.1^{+0.8}_{-1.7}$. This comparison shows that the KCWI Hβ map is less sensitive to regions with $\mathrm{Log}_{10}(L_{\mathrm{H}\beta}/[\mathrm{erg\ s^{-1}}]) < 37$. Tables 8 and 9 show the total number of H II regions per galaxy, and their measured emission line fluxes.

We also observe in Figure 20 that regions with radii less than the KCWI angular resolution are missed in the KCWI–Hβ region sample. This can be seen clearly in Figures 21–27, where we compare the boundaries of the MUSE–Hα and KCWI–Hβ regions. In these figures, we see that many of the missed regions are small and unresolved in the KCWI Hβ map. Also owing to the larger number of detections is that many of the larger KCWI–Hβ regions are resolved into smaller structures in the MUSE–Hα regions.

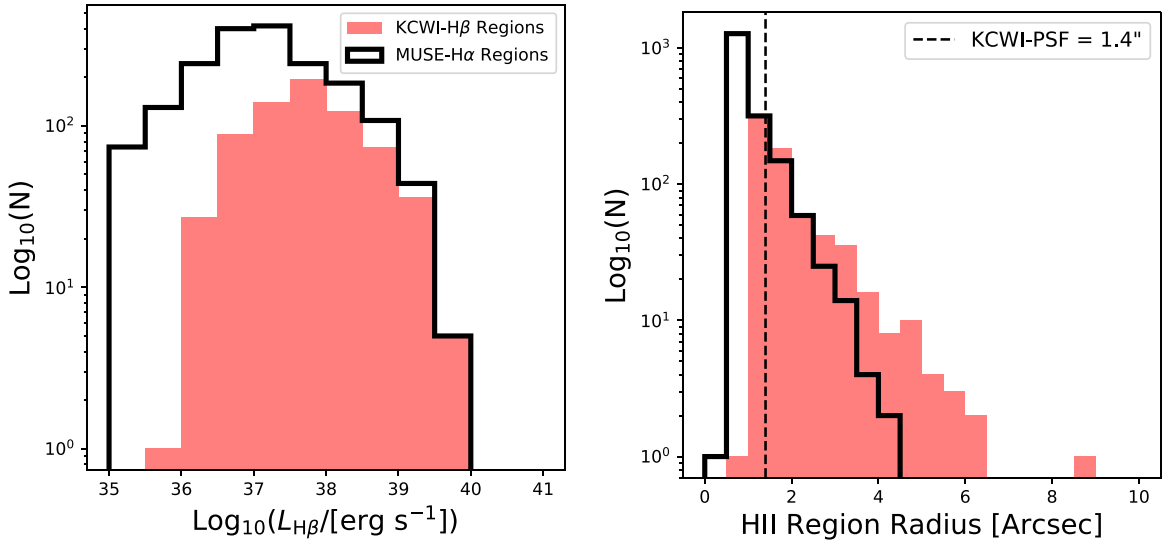

Figure 20. Histogram of the dust-corrected Hβ luminosity for regions identified by `HIIPhot` using KCWI–Hβ maps (red) and regions in the Nebular Catalog identified using MUSE–Hα maps (black). The number of faint regions detected using the KCWI–Hβ map is set by the limiting sensitivity, $\mathrm{Log}_{10}(L_{\mathrm{H}\beta}/[\mathrm{erg\ s^{-1}}]) < 37$, and angular resolution, FWHM $= 1\farcs4$.

Table 8
Total Number of Regions Identified by `HIIphot` as Potential H II Regions per Galaxy Using Both KCWI–Hβ and MUSE–Hα.

Name	N_{KCWI}	N_{MUSE}	N_{A}[a]
NGC 628[b]	10	230	8
NGC 1087	173	364	73
NGC 1300	60	191	28
NGC 1385	133	417	58
NGC 2835	87	135	26
NGC 3627	163	451	19
NGC 5068	62	392	48

Note.
[a] Number of region with significant detection in two or more auroral lines.
[b] NGC 628 was imaged in the least ideal observing conditions.

Table 9
Measured and Derived Properties for H II Regions with Two More Auroral Lines

ID	NGC5068_1	NGC5068_2	NGC5068_3	NGC5068_4	NGC5068_5	NGC5068_6	NGC5068_7	NGC5068_8
R. A. (°)	199.714	199.719	199.702	199.7	199.696	199.714	199.71	199.703
Decl.(°)	−21.027	−21.016	−21.012	−21.013	−21.014	−21.015	−21.038	−21.008
$E(B-V)$(Mag)	0.24	0.19	0.25	0.19	0.41	0.34	0.09	0.18
Hβ[a]	54.2 ± 0.1	70.7 ± 0.4	140.3 ± 0.6	1385.6 ± 7.3	211.4 ± 1.4	37.6 ± 0.2	27.2 ± 0.2	59.8 ± 0.3
[O III]λ4363	…	…	…	12.8 ± 0.7	…	…	…	…
[O III]λ5007	53.6 ± 0.1	125.3 ± 0.5	133.5 ± 0.6	3239.9 ± 15.0	415.7 ± 1.8	35.6 ± 0.1	16.5 ± 0.2	78.2 ± 0.3
[O II]λ7320	0.8 ± 0.1	…	2.4 ± 0.8	35.7 ± 2.2	3.9 ± 0.8	…	0.4 ± 0.1	0.9 ± 0.3
[O II]λ7331	0.8 ± 0.1	…	2.6 ± 0.8	31.1 ± 2.2	3.9 ± 0.8	…	0.4 ± 0.1	1.1 ± 0.3
[O II]λ3727	79.0 ± 0.5	128.0 ± 1.4	515.4 ± 2.6	3128.6 ± 25.3	639.0 ± 5.8	89.3 ± 0.6	62.1 ± 0.6	194.3 ± 1.2
[S II]λ4068	0.6 ± 0.1	1.5 ± 0.1	3.1 ± 0.9	46.4 ± 7.4	4.0 ± 1.2	0.8 ± 0.1	1.3 ± 0.4	1.4 ± 0.2
[S II]λ4076	0.2 ± 0.1	0.5 ± 0.1	3.1 ± 1.8	3.8 ± 3.6	0.0 ± 2.4	0.3 ± 0.1	0.1 ± 0.1	0.5 ± 0.2
[S III]λ6313	0.5 ± 0.0	0.7 ± 0.1	1.5 ± 0.1	18.9 ± 0.3	2.7 ± 0.1	0.4 ± 0.0	0.2 ± 0.0	0.7 ± 0.0
[S II]λ6716	12.7 ± 0.1	22.6 ± 0.2	60.4 ± 0.3	352.1 ± 0.9	71.0 ± 0.3	14.4 ± 0.1	10.6 ± 0.1	21.5 ± 0.1
[S II]λ6731	9.4 ± 0.1	15.8 ± 0.1	42.1 ± 0.3	259.1 ± 0.8	49.8 ± 0.3	10.1 ± 0.1	7.3 ± 0.1	14.8 ± 0.1
[S III]λ9069	11.9 ± 0.1	12.4 ± 0.2	20.5 ± 0.2	389.1 ± 1.2	42.3 ± 0.3	7.1 ± 0.1	4.5 ± 0.1	9.9 ± 0.1
[N II]λ5756	0.3 ± 0.0	0.3 ± 0.0	0.5 ± 0.1	4.3 ± 0.1	0.8 ± 0.1	0.1 ± 0.0	0.1 ± 0.0	0.2 ± 0.1
[N II]λ6548	10.2 ± 0.0	9.1 ± 0.1	20.3 ± 0.1	152.5 ± 0.3	25.2 ± 0.1	6.2 ± 0.0	4.7 ± 0.0	6.8 ± 0.0
[N II]λ6584	30.1 ± 0.1	26.9 ± 0.2	59.7 ± 0.3	449.8 ± 1.0	74.1 ± 0.3	18.3 ± 0.1	13.9 ± 0.1	20.0 ± 0.1
n_e(cm^{-3})	99	21	13	91	20	22	12	10
[O III]/[O II]	0.68 ± 0.0	0.98 ± 0.01	0.26 ± 0.0	1.04 ± 0.01	0.65 ± 0.01	0.4 ± 0.0	0.27 ± 0.0	0.4 ± 0.0
[S III]/[S II]	1.87 ± 0.02	1.13 ± 0.02	0.7 ± 0.01	2.23 ± 0.01	1.23 ± 0.01	1.01 ± 0.01	0.88 ± 0.01	0.95 ± 0.01
$T_{e,[N\ II]}$ (K)	8179.0 ± 291.0	8769.0 ± 563.0	8122.0 ± 489.0	8486.0 ± 90.0	9056.0 ± 458.0	7461.0 ± 657.0	8208.0 ± 778.0	8232.0 ± 858.0
$T_{e,[S\ II]}$ (K)	7580.0 ± 768.0	10364.0 ± 594.0	11467.0 ± 3028.0	14318.0 ± 2652.0	7704.0 ± 2444.0	8661.0 ± 1044.0	14772.0 ± 4095.0	10029.0 ± 1260.0
$T_{e,[O\ II]}$ (K)	10941.0 ± 1467.0	…	7999.0 ± 1134.0	11243.0 ± 700.0	8785.0 ± 1009.0	…	9042.0 ± 1421.0	8120.0 ± 1143.0
$T_{e,[S\ III]}$ (K)	8513.0 ± 110.0	9528.0 ± 421.0	10235.0 ± 273.0	8755.0 ± 52.0	9807.0 ± 180.0	9249.0 ± 365.0	8438.0 ± 185.0	10250.0 ± 297.0
$T_{e,[O\ III]}$ (K)	…	…	…	8658.0 ± 135.0	…	…	…	…

Note.
[a] Emission-line strengths and uncertainties are reported in units of 10^{-16} × erg s^{-1} cm^{-2}.

(This table is available in its entirety in machine-readable form.)

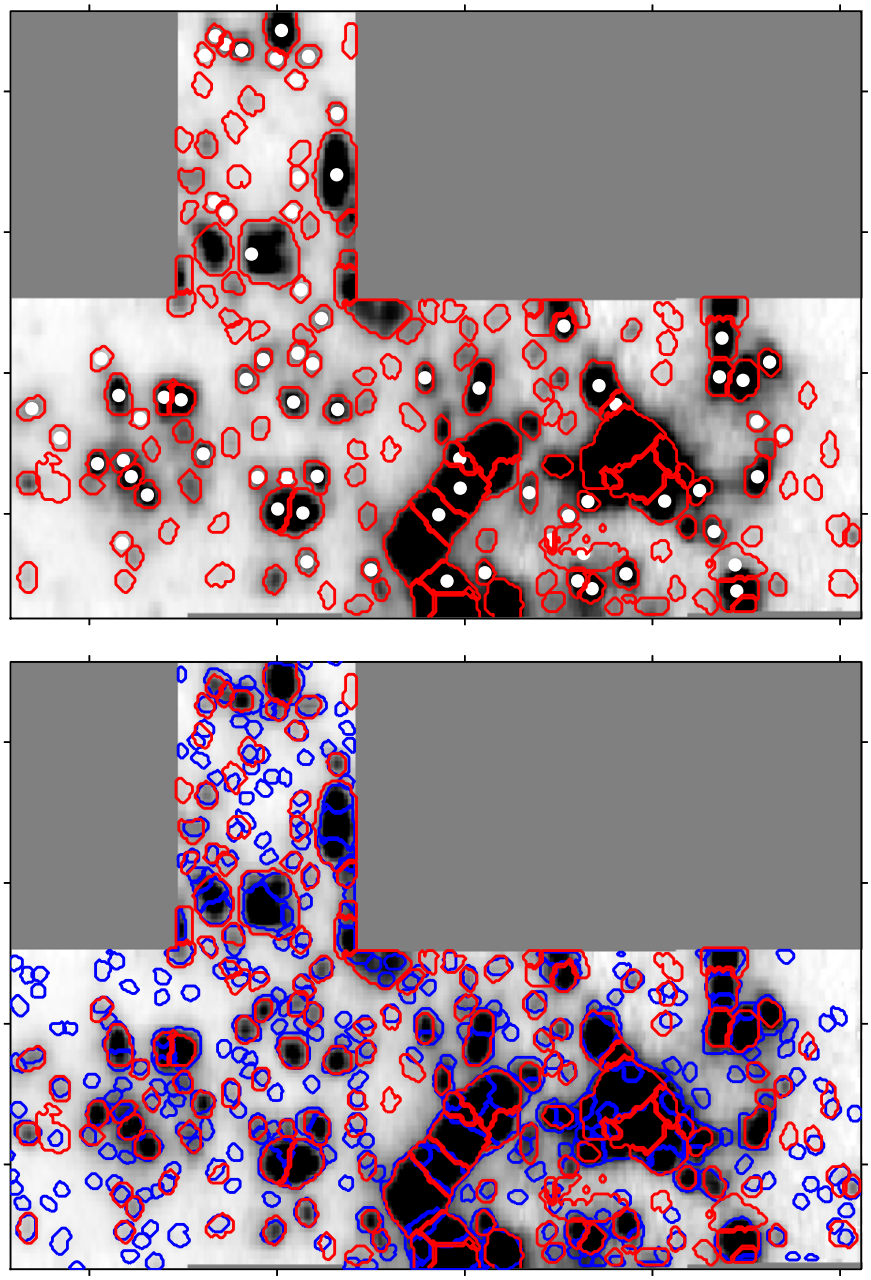

Figure 21. Comparison of region boundaries identified using `HIIPhot` and either KCWI–Hβ or MUSE–Hα emission-line maps for the galaxy NGC 1087. The KCWI–Hβ emission-line map is shown in both panels. We overlay in red the morphology of regions identified by `HIIPhot` using the KCWI–Hβ emission-line map. A white marker indicates a region with significant auroral-line detections in two or more auroral lines. In blue, we overlay region boundaries from `HIIPhot` using the MUSE Hα emission-line maps (Kreckel et al. 2019; Groves et al. 2023).

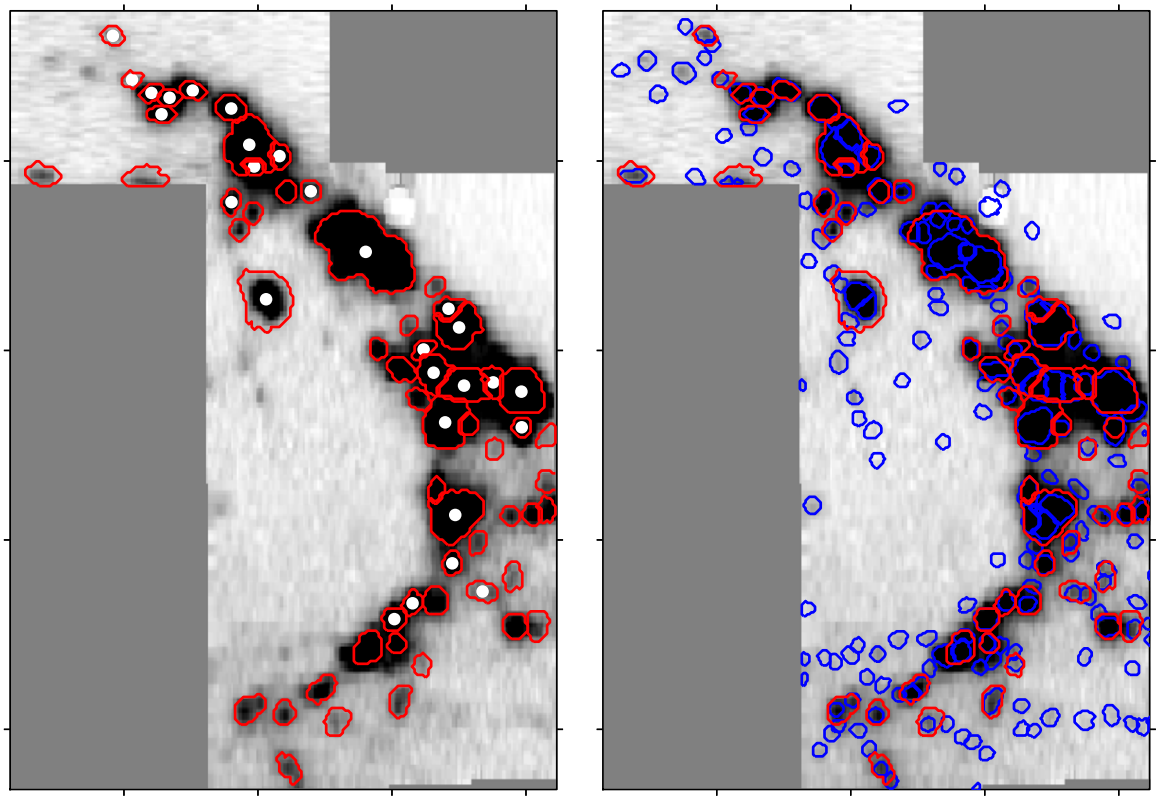

Figure 22. Comparison of H II region boundaries in NGC 1300, following Figure 21.

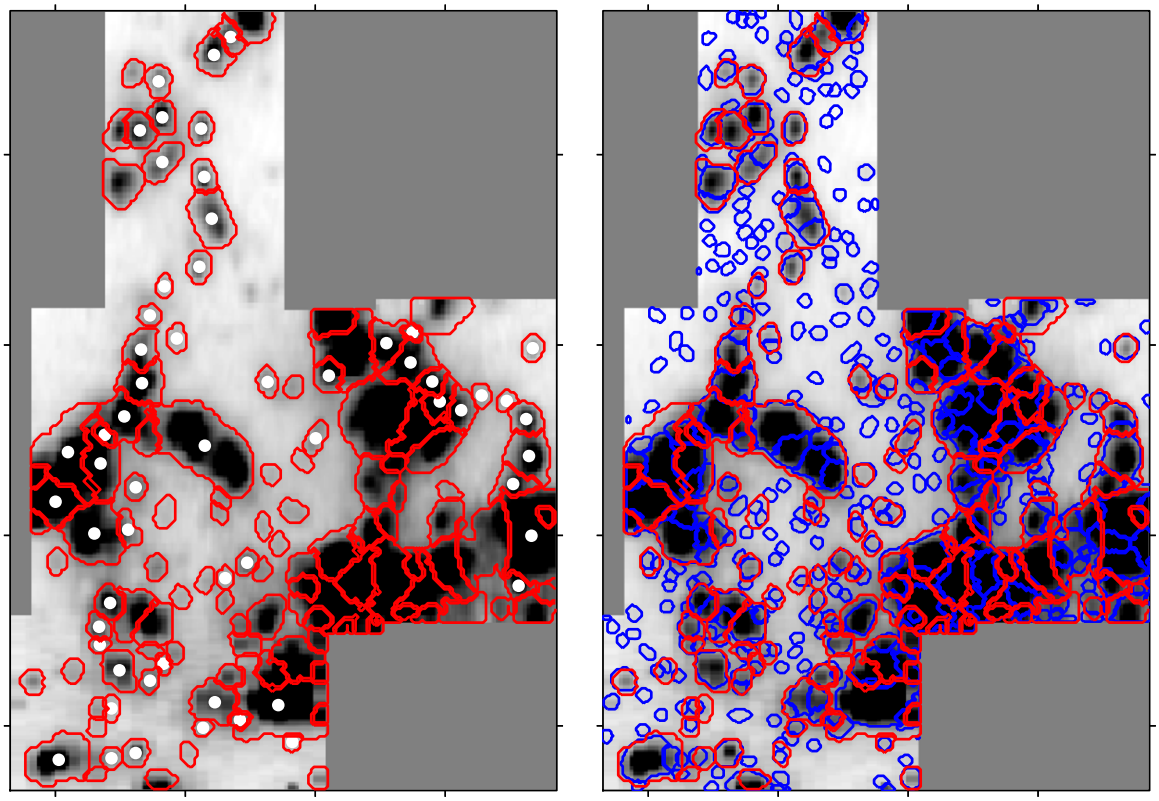

Figure 23. Comparison of H II region boundaries in NGC 1385, following Figure 21.

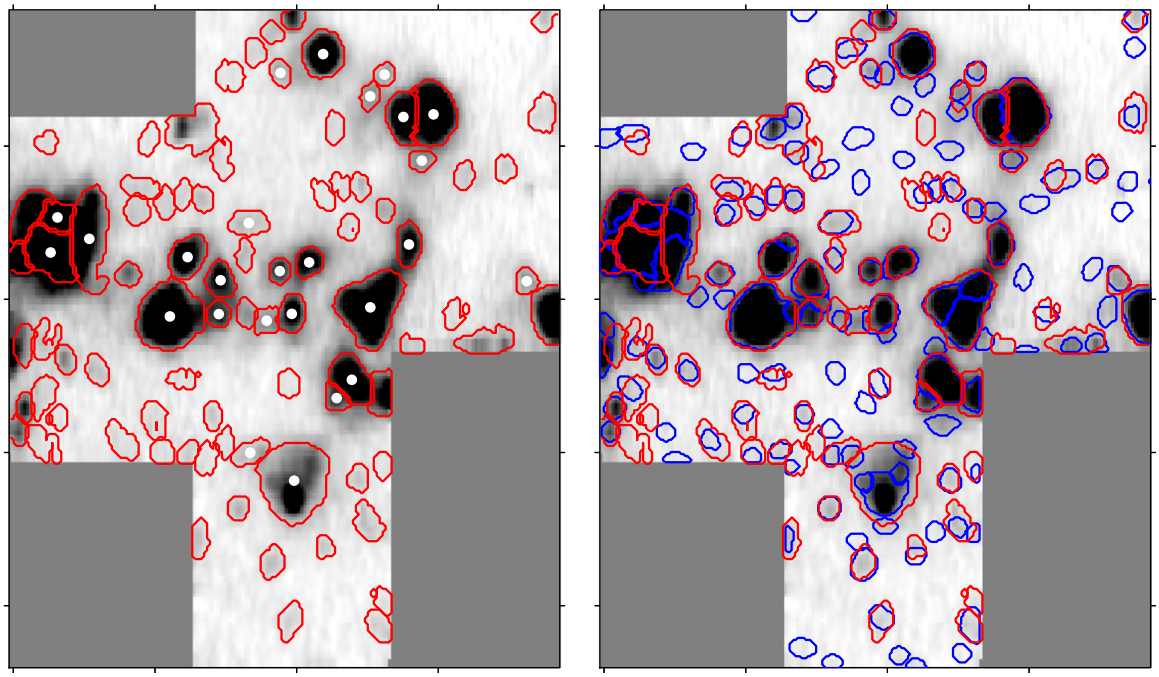

Figure 24. Comparison of H II region boundaries in NGC 2835, following Figure 21.

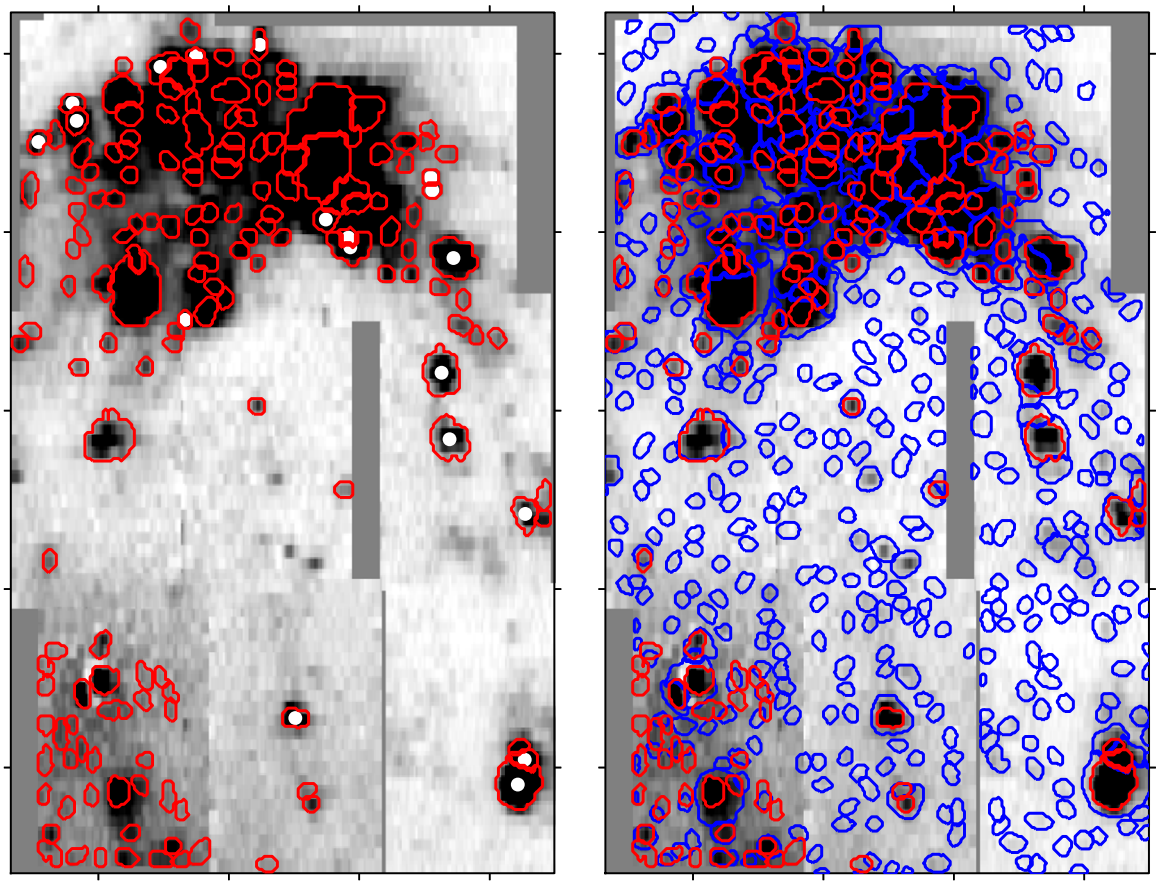

Figure 25. Comparison of H II region boundaries in NGC 3627, following Figure 21.

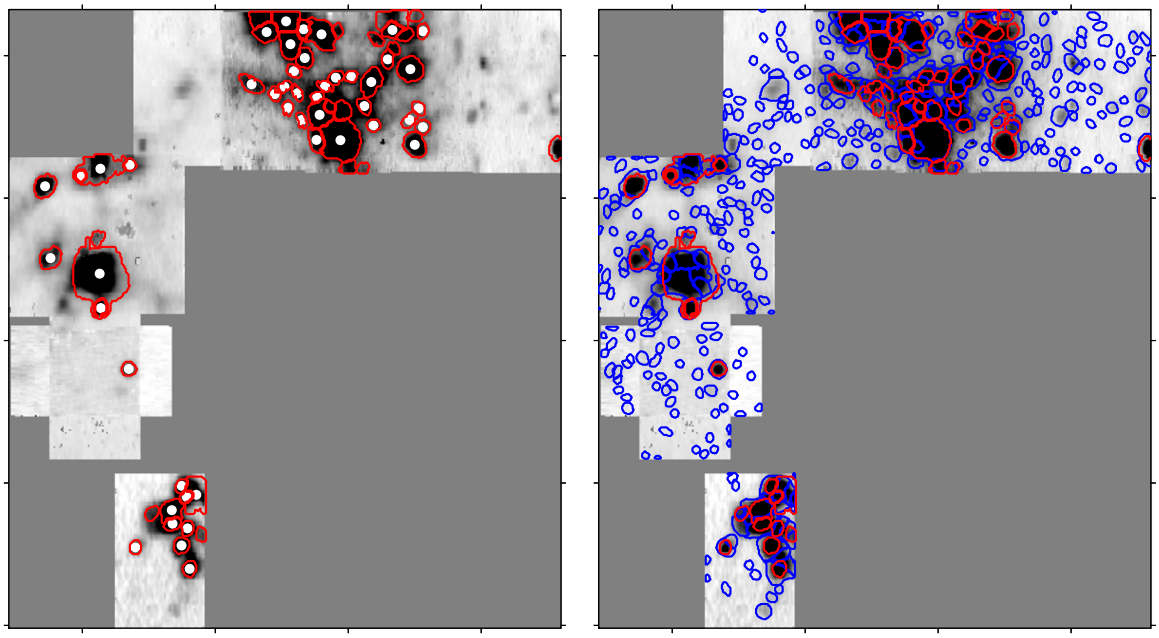

Figure 26. Comparison of H II region boundaries in NGC 5068, following Figure 21.

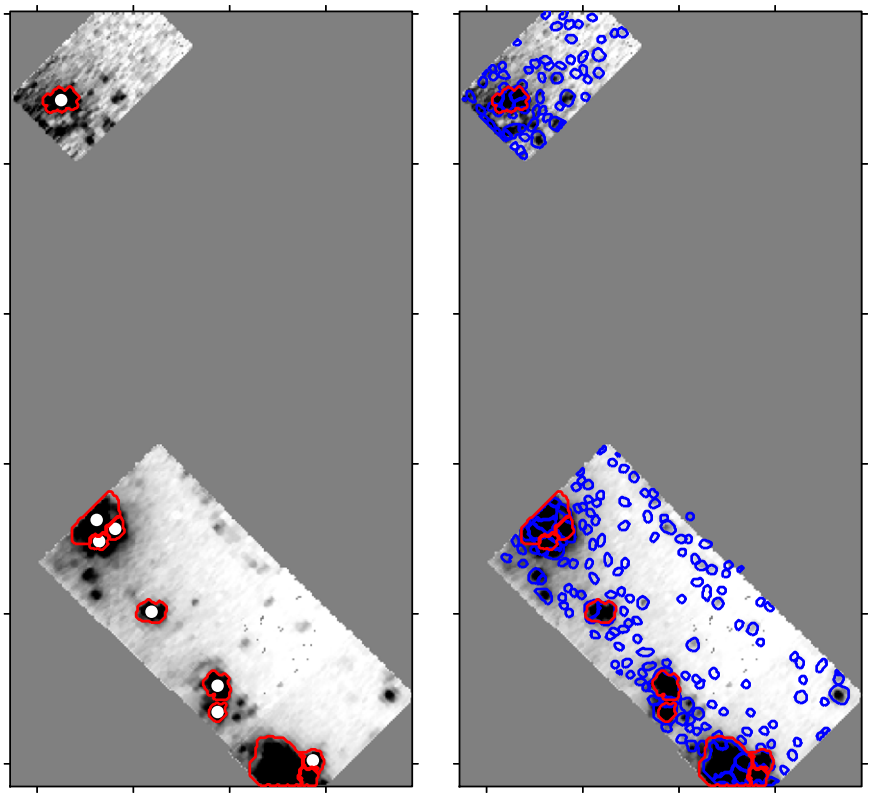

Figure 27. Comparison of H II region boundaries in NGC 628, following Figure 21.

Appendix D
Example Gaussian Fits to Auroral Lines

In this section, we show example auroral-line fits. In Figure 28, we show fits to high-S/N auroral lines from an H II region in NGC 5068. We also include in Figure 28 annotations describing the standard deviation of the fit residuals, σ_{res}, the S/N for a single emission line (or in the instance of simultaneous double line fits, the S/Ns of the red and purple Gaussian fits, i.e., S/N_r and S/N_p), the continuum noise, $\sigma_{\rm cont}$, and the reduced χ^2. In this particular example, the auroral line in these fits are isolated from contaminating sky lines or nearby emission, especially in the case of [O III] λ4363 Å, where the contribution from [Fe II]λ4360 Å is negligible. To demonstrate fitting [Fe II]λ4360 alongside [O III]λ4363, we show a low-S/N detection with nonnegligible contamination from [Fe II]λ4360 Å in Figure 29.

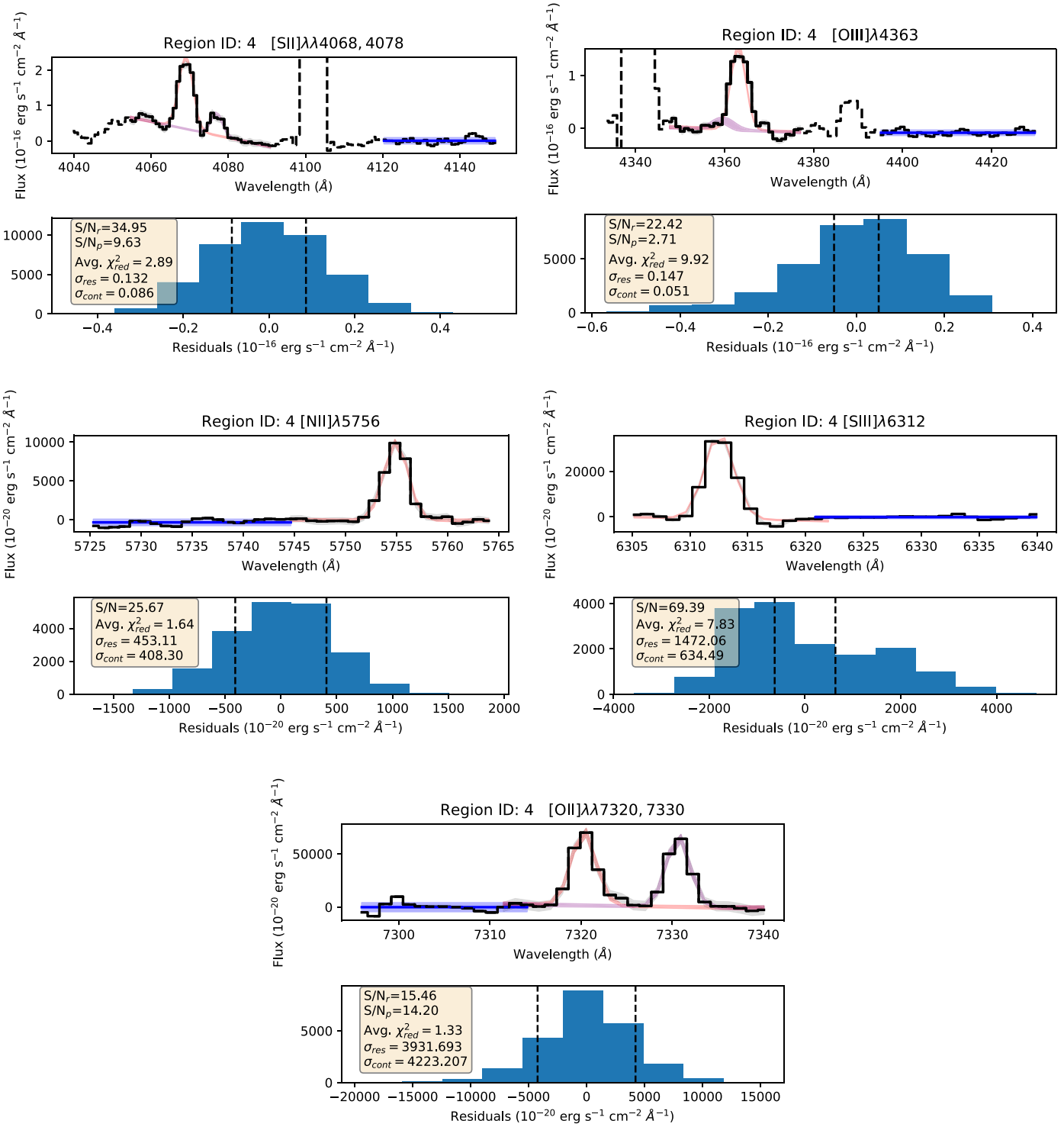

Figure 28. Auroral-line fits for an H II region in NGC 5068. We show in each panel a summary of auroral-line fits for a single H II region in NGC 5068. The top frame in each panel shows the data, (black solid), for the fitting and continuum wavelength ranges. In the wavelength range where $\sigma_{\rm cont}$ is measured, we overlay $\pm\sigma_{\rm cont}$ region (blue shaded) around the line, indicating the average value of the continuum (blue solid). The red shaded and purple shaded regions for the double Gaussian fits show the 1σ ranges of the fitted models. The bottom frame in each panels shows a histogram of the residuals. We also print text summarizing the S/N and average reduced χ^2 of the fits as well as the 1σ of the residuals and value of $\sigma_{\rm cont}$.

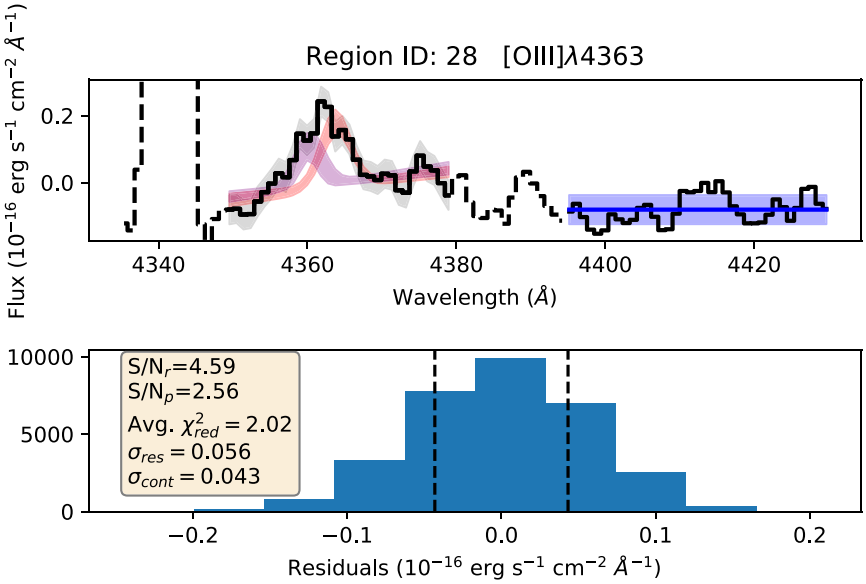

Figure 29. Example of an auroral-line fit measuring [O III]λ4363 Å flux with nonnegligible [Fe II]λ4360 contribution for an H II region in NGC 1087. Annotations follow those in Figure 28.

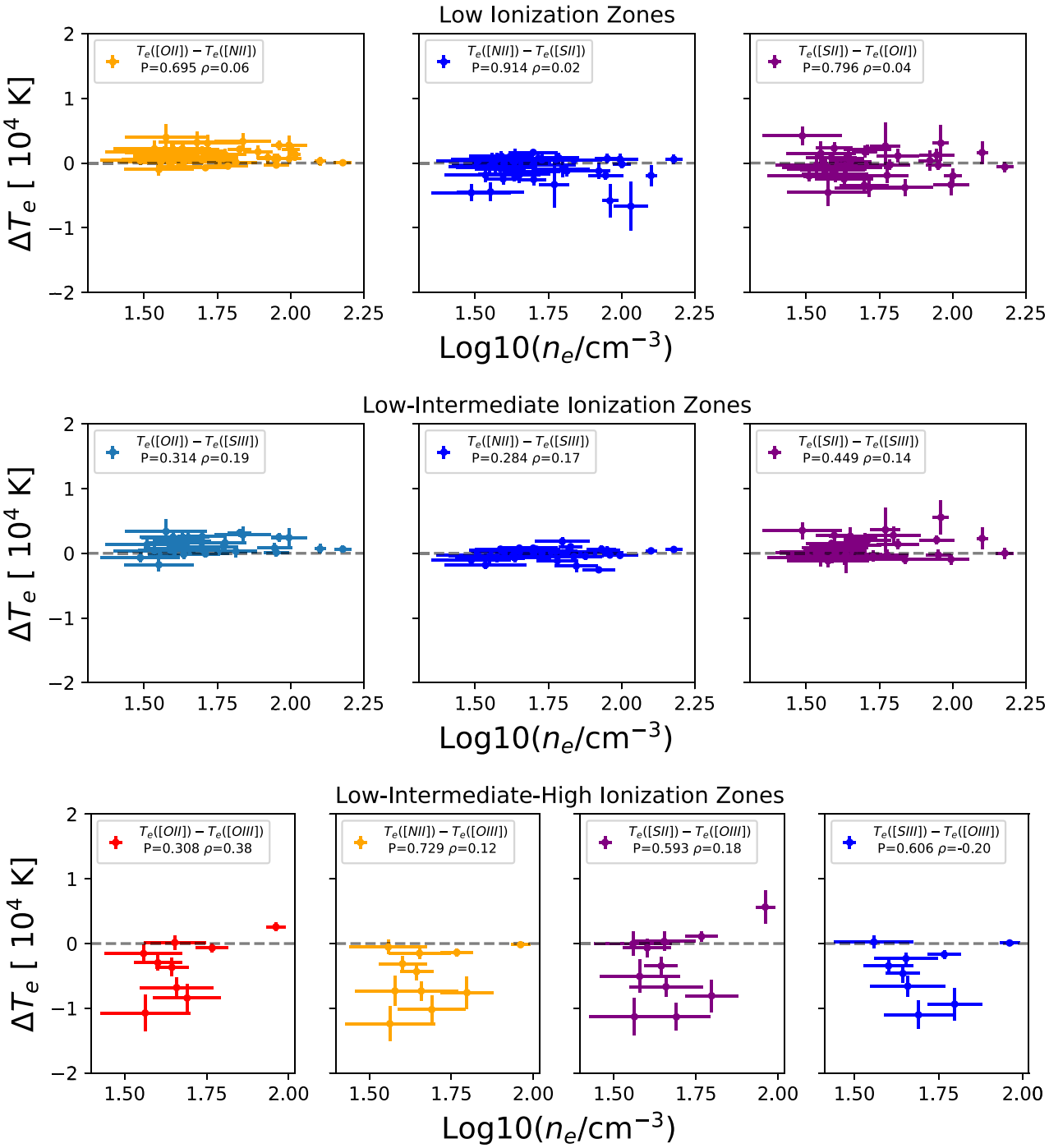

Figure 30. Electron temperature differences compared to the H II region electron density, n_e. Top: the values of ΔT_e between the low-ionization zone temperatures. Middle: the values of ΔT_e between the low- and intermediate-ionization zone temperatures. Bottom: the values of ΔT_e between the low-, intermediate-, and high-ionization zone temperatures.

Appendix E
Figures of the ΔT_e and H II Region Property Comparisons

In the section, we present in Figures 31–36 the comparisons between H II region properties that exhibit no significant correlations with ΔT_e.

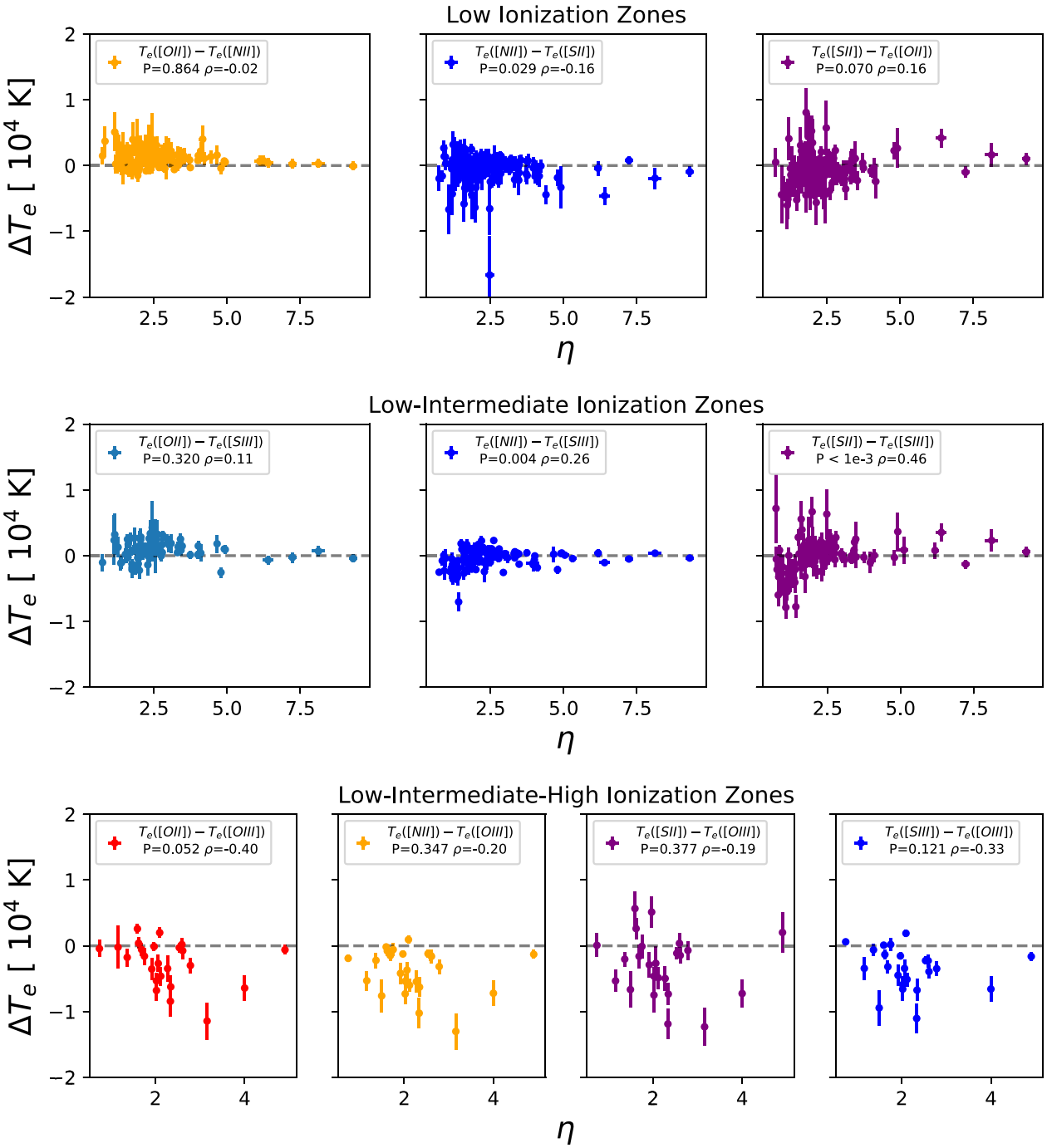

Figure 31. Electron temperature differences compared to the radiation softness parameter. The order of the panels follows that in Figure 30.

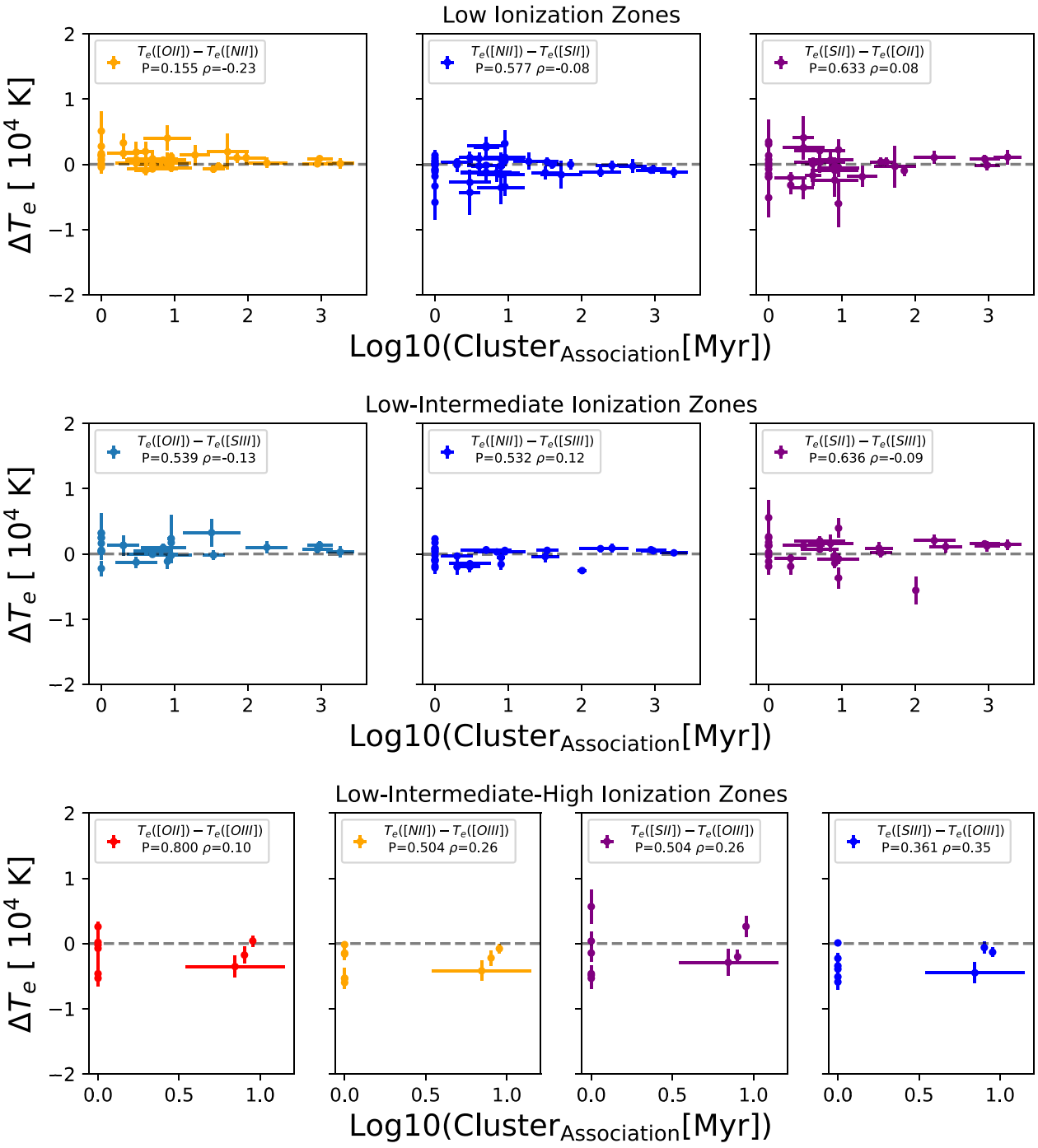

Figure 32. Electron temperature differences compared to the stellar cluster age. The order of the panels follows that in Figure 30.

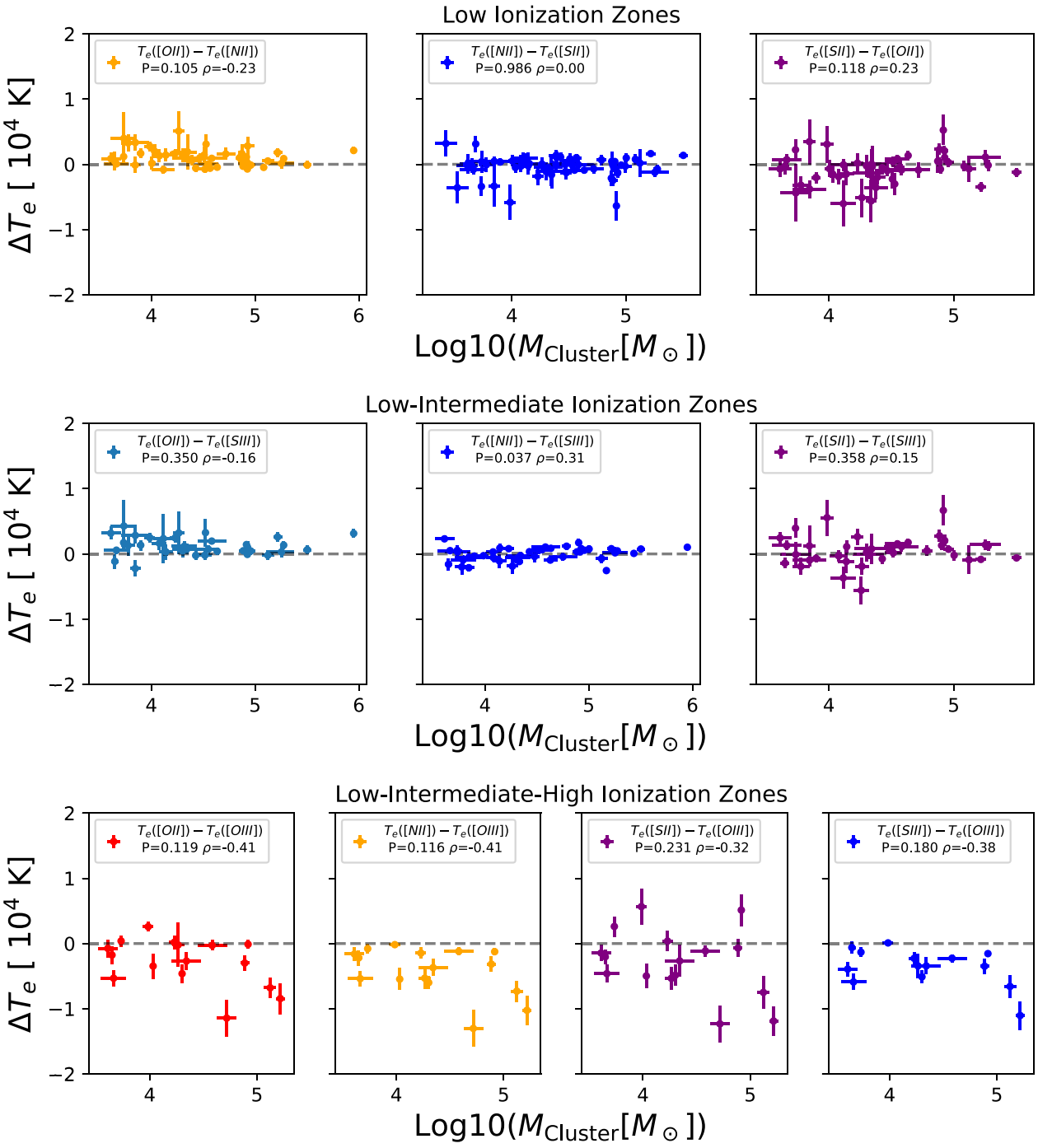

Figure 33. Electron temperature differences compared to the stellar cluster mass. The order of the panels follows that in Figure 30.

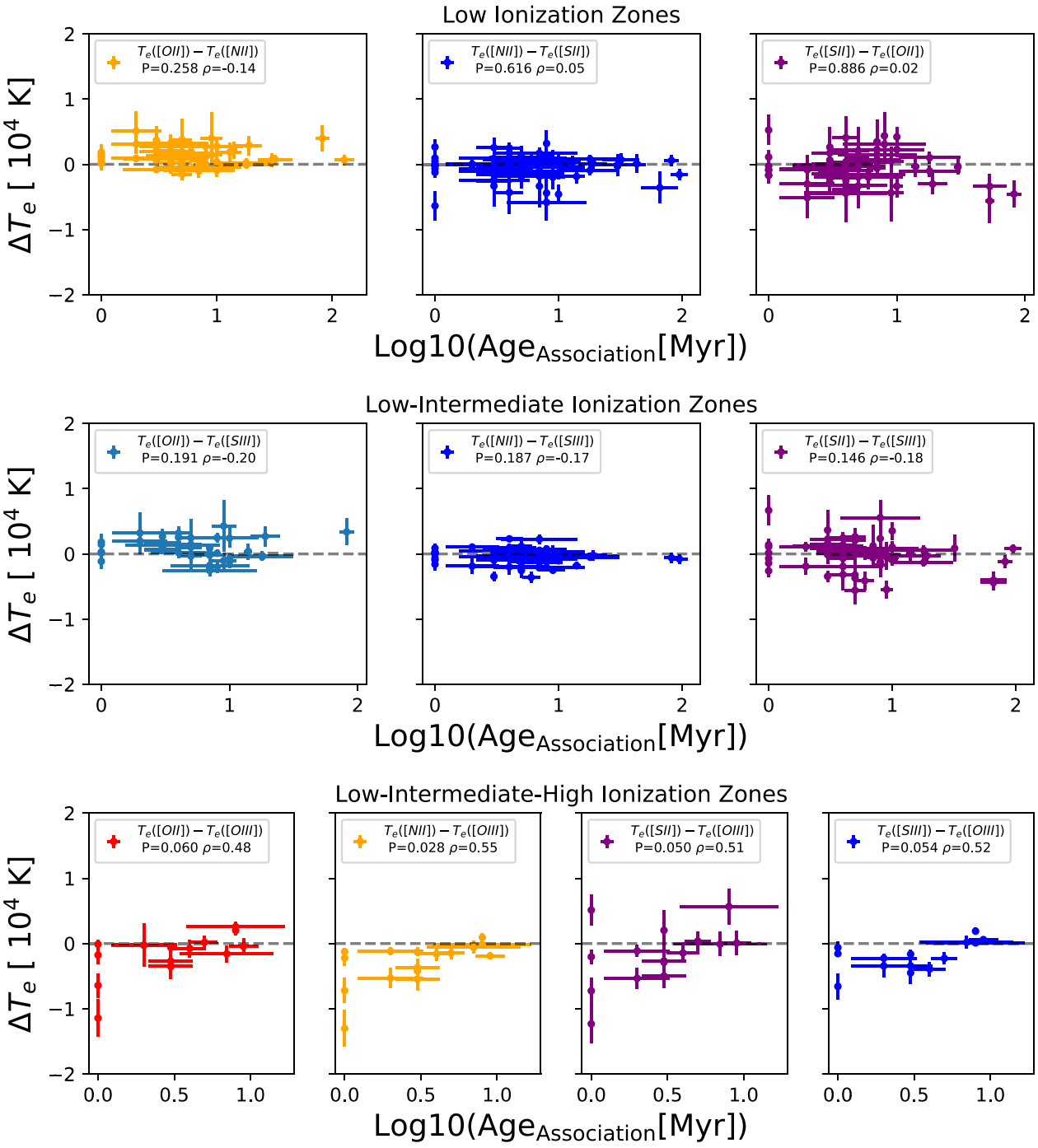

Figure 34. Electron temperature differences compared to the stellar association age. The order of the panels follows that in Figure 30.

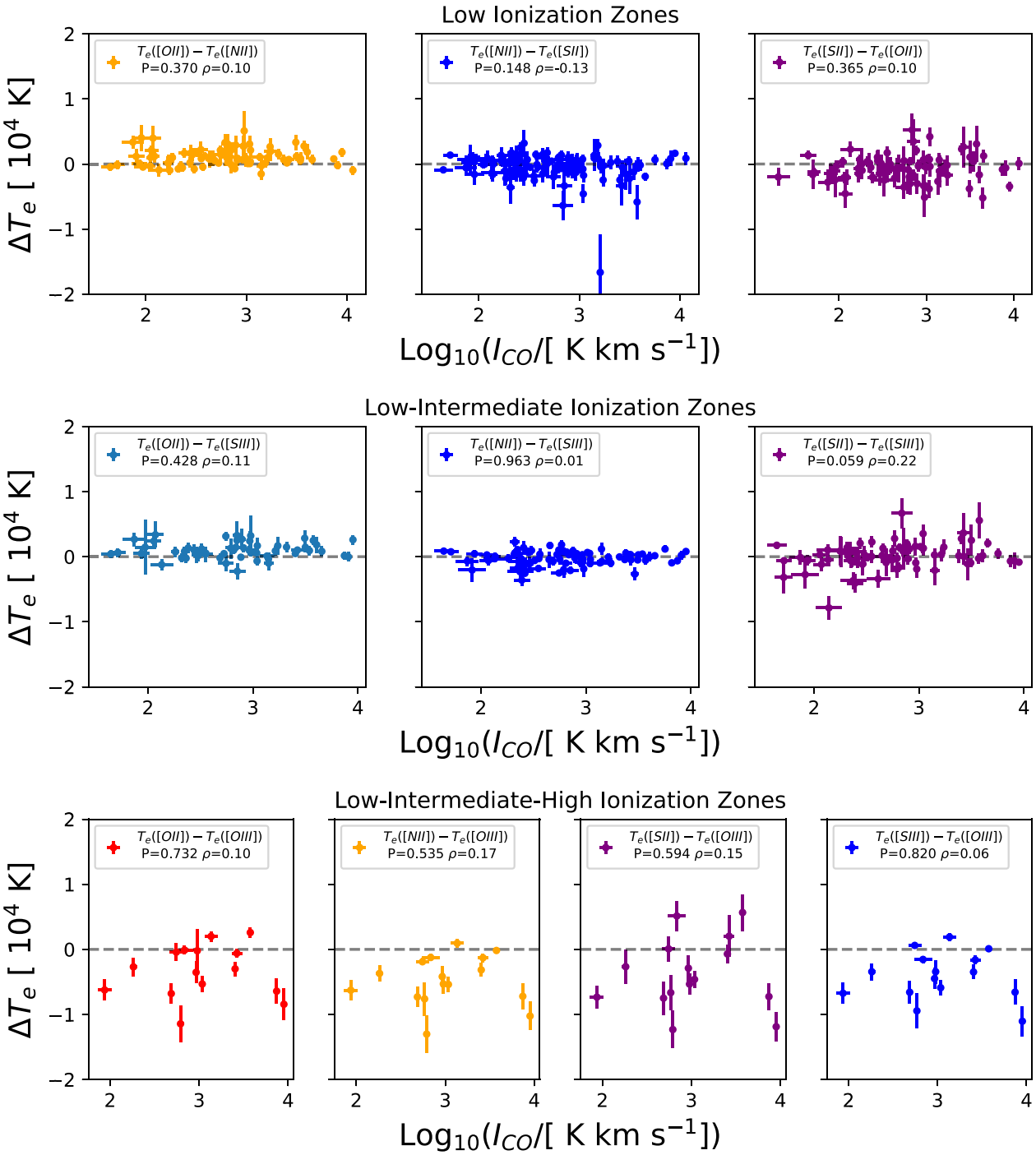

Figure 35. Electron temperature differences compared to the intensity of CO emission, I_{CO}. The order of the panels follows that in Figure 30.

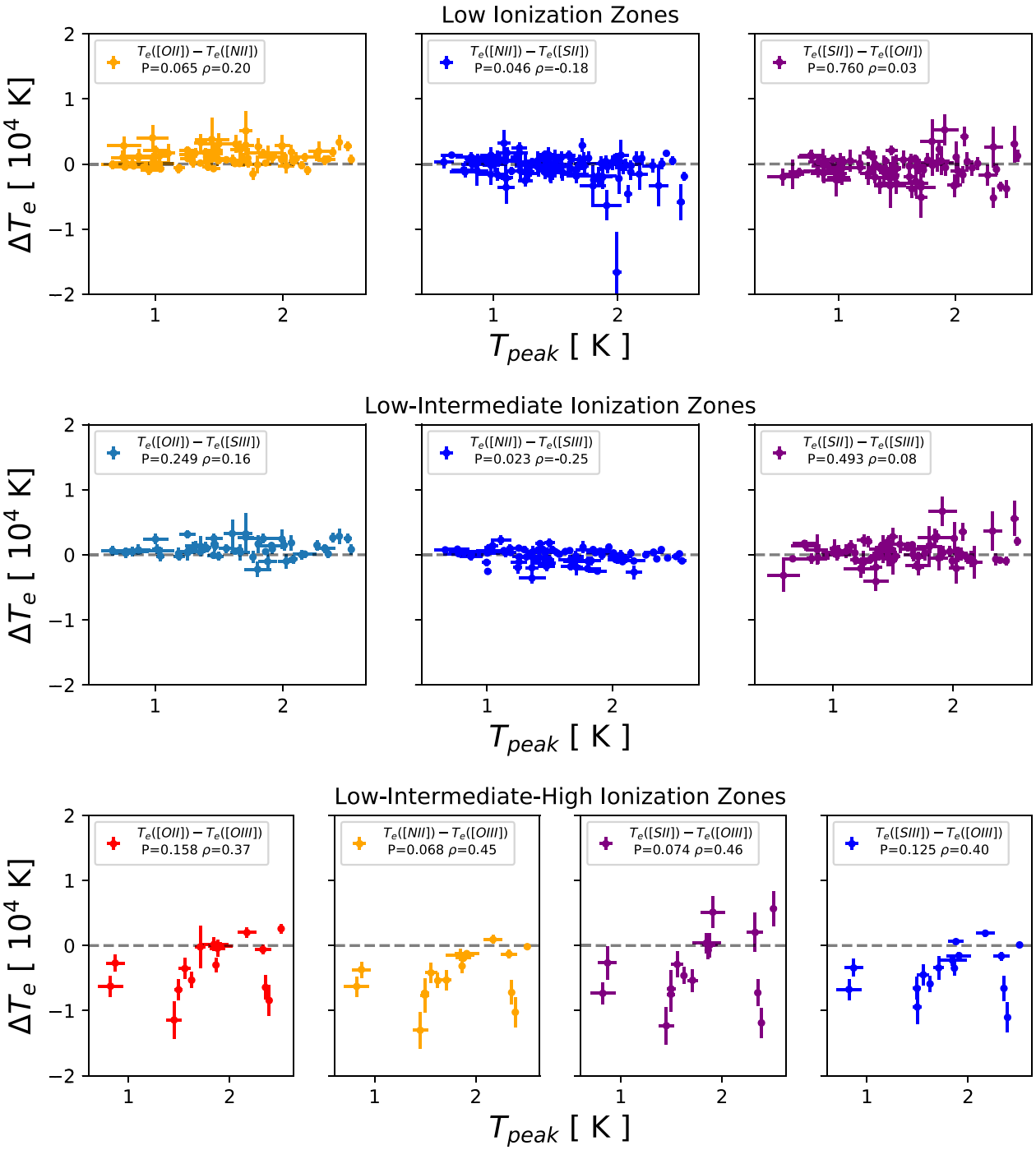

Figure 36. Electron temperature differences compared to the CO peak temperature, $T_{\rm peak}$. The order of the panels follows that in Figure 30.

ORCID iDs

Ryan J. Rickards Vaught https://orcid.org/0000-0001-9719-4080
Karin M. Sandstrom https://orcid.org/0000-0002-4378-8534
Francesco Belfiore https://orcid.org/0000-0002-2545-5752
Kathryn Kreckel https://orcid.org/0000-0001-6551-3091
J. Eduardo Méndez-Delgado https://orcid.org/0000-0002-6972-6411
Eric Emsellem https://orcid.org/0000-0002-6155-7166
Brent Groves https://orcid.org/0000-0002-9768-0246
Guillermo A. Blanc https://orcid.org/0000-0003-4218-3944
Daniel A. Dale https://orcid.org/0000-0002-5782-9093
Oleg V. Egorov https://orcid.org/0000-0002-4755-118X
Simon C. O. Glover https://orcid.org/0000-0001-6708-1317
Kathryn Grasha https://orcid.org/0000-0002-3247-5321
Ralf S. Klessen https://orcid.org/0000-0002-0560-3172
Justus Neumann https://orcid.org/0000-0002-3289-8914
Thomas G. Williams https://orcid.org/0000-0002-0012-2142

References

Abazajian, K., Adelman-McCarthy, J. K., Agüeros, M. A., et al. 2003, AJ, 126, 2081
Abolmasov, P., Fabrika, S., Sholukhova, O., & Afanasiev, V. 2007, AstBu, 62, 36

Allen, M. G., Groves, B. A., Dopita, M. A., Sutherland, R. S., & Kewley, L. J. 2008, ApJS, 178, 20
Anand, G. S., Lee, J. C., Van Dyk, S. D., et al. 2021, MNRAS, 501, 3621
Arellano-Córdova, K. Z., & Rodríguez, M. 2020, MNRAS, 497, 672
Astropy Collaboration, Robitaille, T. P., Tollerud, E. J., et al. 2013, A&A, 558, A33
Bacon, R., Accardo, M., Adjali, L., et al. 2010, Proc. SPIE, 7735, 773508
Baldwin, J. A., Ferland, G. J., Martin, P. G., et al. 1991, ApJ, 374, 580
Baldwin, J. A., Phillips, M. M., & Terlevich, R. 1981, PASP, 93, 5
Belfiore, F., Santoro, F., Groves, B., et al. 2022, A&A, 659, A26
Belfiore, F., Westfall, K. B., Schaefer, A., et al. 2019, AJ, 158, 160
Berg, D. A., Pogge, R. W., Skillman, E. D., et al. 2020, ApJ, 893, 96
Berg, D. A., Skillman, E. D., Croxall, K. V., et al. 2015, ApJ, 806, 16
Binette, L., Matadamas, R., Hägele, G. F., et al. 2012, A&A, 547, A29
Blanc, G. A., Kewley, L., Vogt, F. P. A., & Dopita, M. A. 2015, ApJ, 798, 99
Bresolin, F., Kennicutt, R. C., & Ryan-Weber, E. 2012, ApJ, 750, 122
Calzetti, D., Lee, J. C., Sabbi, E., et al. 2015, AJ, 149, 51
Campbell, A., Terlevich, R., & Melnick, J. 1986, MNRAS, 223, 811
Cappellari, M. 2017, MNRAS, 466, 798
Cappellari, M., & Emsellem, E. 2004, PASP, 116, 138
Casini, R., & de Wijn, A. G. 2014, JOSAA, 31, 2002
Congiu, E., Blanc, G. A., Belfiore, F., et al. 2023, A&A, 672, A148
Corradi, R. L. M., Grosso, N., Acker, A., Greimel, R., & Guillout, P. 2014, A&A, 570, A105
Cosens, M., Wright, S. A., Murray, N., et al. 2022, ApJ, 929, 74
Curti, M., Cresci, G., Mannucci, F., et al. 2017, MNRAS, 465, 1384
da Silva, R. L., Fumagalli, M., & Krumholz, M. 2012, ApJ, 745, 145
Díaz, Á. I., & Zamora, S. 2022, MNRAS, 511, 4377
Dopita, M. A., & Sutherland, R. S. 1996, ApJS, 102, 161
Dors, O. L. J., Krabbe, A., Hägele, G. F., & Pérez-Montero, E. 2011, MNRAS, 415, 3616
Draine, B. T. 2011, Physics of the Interstellar and Intergalactic Medium (Princeton, NJ: Princeton Univ. Press)
Egorov, O. V., Kreckel, K., Glover, S. C. O., et al. 2023, A&A, 678, A153
Egorov, O. V., Lozinskaya, T. A., Moiseev, A. V., & Shchekinov, Y. A. 2017, MNRAS, 464, 1833
Egorov, O. V., Lozinskaya, T. A., Moiseev, A. V., & Smirnov-Pinchukov, G. V. 2014, MNRAS, 444, 376
Emsellem, E., Schinnerer, E., Santoro, F., et al. 2022, A&A, 659, A191
Esteban, C., Peimbert, M., García-Rojas, J., et al. 2004, MNRAS, 355, 229
Fitzpatrick, E. L. 1999, PASP, 111, 63
Freedman, W. L., Madore, B. F., Gibson, B. K., et al. 2001, ApJ, 553, 47
Froese Fischer, C., & Tachiev, G. 2004, ADNDT, 87, 1
Froese Fischer, C., Tachiev, G., & Irimia, A. 2006, ADNDT, 92, 607
García-Rojas, J., & Esteban, C. 2007, ApJ, 670, 457
Garnett, D. R. 1992, AJ, 103, 1330
Garnett, D. R., Kennicutt, R. C. J., Chu, Y.-H., & Skillman, E. D. 1991, ApJ, 373, 458
Grasha, K., Calzetti, D., Adamo, A., et al. 2019, MNRAS, 483, 4707
Grasha, K., Chen, Q. H., Battisti, A. J., et al. 2022, ApJ, 929, 118
Grisé, F., Pakull, M. W., Soria, R., et al. 2008, A&A, 486, 151
Groves, B., Kreckel, K., Santoro, F., et al. 2023, MNRAS, 520, 4902
Guseva, N. G., Izotov, Y. I., & Thuan, T. X. 2000, ApJ, 531, 776
Hernandez, A. K., Wakker, B. P., Benjamin, R. A., et al. 2013, ApJ, 777, 19
Hill, J. K., & Hollenbach, D. J. 1978, ApJ, 225, 390
Ho, I. T., Medling, A. M., Groves, B., et al. 2016, Ap&SS, 361, 280
Ho, I. T., Seibert, M., Meidt, S. E., et al. 2017, ApJ, 846, 39
Jacobs, B. A., Rizzi, L., Tully, R. B., et al. 2009, AJ, 138, 332
Jin, Y., Kewley, L. J., & Sutherland, R. S. 2022, ApJL, 934, L8
Kainulainen, J., Stutz, A. M., Stanke, T., et al. 2017, A&A, 600, A141
Kaler, J. B., Aller, L. H., Czyzak, S. J., & Epps, H. W. 1976, ApJS, 31, 163
Kauffmann, G., Heckman, T. M., Tremonti, C., et al. 2003, MNRAS, 346, 1055
Kelly, B. C. 2007, ApJ, 665, 1489
Kennicutt, R. C., Jr. 1984, ApJ, 287, 116
Kennicutt, R. C., Jr., Bresolin, F., & Garnett, D. R. 2003, ApJ, 591, 801
Kennicutt, R. C., Jr., & Garnett, D. R. 1996, ApJ, 456, 504
Kewley, L. J., & Dopita, M. A. 2002, ApJS, 142, 35
Kewley, L. J., & Ellison, S. L. 2008, ApJ, 681, 1183
Kewley, L. J., Heisler, C. A., Dopita, M. A., & Lumsden, S. 2001, ApJS, 132, 37
Kisielius, R., Storey, P. J., Ferland, G. J., & Keenan, F. P. 2009, MNRAS, 397, 903
Koo, B.-C., Rho, J., Reach, W. T., Jung, J., & Mangum, J. G. 2001, ApJ, 552, 175
Kothes, R., & Kerton, C. R. 2002, A&A, 390, 337
Kourkchi, E., Courtois, H. M., Graziani, R., et al. 2020, AJ, 159, 67
Kourkchi, E., & Tully, R. B. 2017, ApJ, 843, 16
Kreckel, K., Egorov, O. V., Belfiore, F., et al. 2022, A&A, 667, A16
Kreckel, K., Ho, I. T., Blanc, G. A., et al. 2019, ApJ, 887, 80
Kreckel, K., Ho, I. T., Blanc, G. A., et al. 2020, MNRAS, 499, 193
Larson, K. L., Lee, J. C., Thilker, D. A., et al. 2023, MNRAS, 523, 6061
Law, D. R., Cherinka, B., Yan, R., et al. 2016, AJ, 152, 83
Lee, J. C., Whitmore, B. C., Thilker, D. A., et al. 2022, ApJS, 258, 10
Leroy, A. K., Hughes, A., Liu, D., et al. 2021a, ApJS, 255, 19
Leroy, A. K., Schinnerer, E., Hughes, A., et al. 2021b, ApJS, 257, 43
Luridiana, V., Morisset, C., & Shaw, R. A. 2015, A&A, 573, A42
Makarov, D., Prugniel, P., Terekhova, N., Courtois, H., & Vauglin, I. 2014, A&A, 570, A13
Maschmann, D., Lee, J. C., & Thilker, D. A. 2024, ApJS, submitted (arXiv: 2403.04901)
Mayya, Y. D., Plat, A., Gómez-González, V. M. A., et al. 2023, MNRAS, 519, 5492
McLeod, A. F., Weilbacher, P. M., Ginsburg, A., et al. 2016, MNRAS, 455, 4057
Méndez-Delgado, J. E., Esteban, C., García-Rojas, J., & Henney, W. J. 2022, MNRAS, 514, 744
Méndez-Delgado, J. E., Esteban, C., García-Rojas, J., Kreckel, K., & Peimbert, M. 2023a, Natur, 618, 249
Méndez-Delgado, J. E., Esteban, C., García-Rojas, J., et al. 2021, MNRAS, 502, 1703
Méndez-Delgado, J. E., Esteban, C., García-Rojas, J., et al. 2023b, MNRAS, 523, 2952
Mendoza, C., & Bautista, M. A. 2014, ApJ, 785, 91
Mendoza, C., Méndez-Delgado, J. E., Bautista, M., García-Rojas, J., & Morisset, C. 2023, Atoms, 11, 63
Morisset, C. 2009, MmSAI, 80, 397
Morrissey, P., Matuszewski, M., Martin, D. C., et al. 2018, ApJ, 864, 93
Nicholls, D. C., Kewley, L. J., & Sutherland, R. S. 2020, PASP, 132, 033001
Nugent, P., Sullivan, M., Ellis, R., et al. 2006, ApJ, 645, 841
Núñez-Díaz, M., Esteban, C., & Mesa-Delgado, A. 2013, Highlights of Spanish Astrophysics VII, ed. J. C. Guirado et al., 594, https://www.sea-astronomia.es/sites/default/files/archivos/proceedings10/via_lactea/ORALES/nunezm.pdf
O'Dell, C. R., Ferland, G. J., & Peimbert, M. 2017, MNRAS, 464, 4835
O'Donnell, J. E. 1994, ApJ, 422, 158
Oh, K., Sarzi, M., Schawinski, K., & Yi, S. K. 2011, ApJS, 195, 13
Osterbrock, D. E., & Ferland, G. J. 2006, Astrophysics of Gaseous Nebulae and Active Galactic Nuclei (Mill Valley, CA: Univ. Science Books)
Padmanabhan, N., Schlegel, D. J., Finkbeiner, D. P., et al. 2008, ApJ, 674, 1217
Peimbert, M. 1967, ApJ, 150, 825
Peimbert, M. 1971, BOTT, 6, 29
Peimbert, M., & Costero, R. 1969, BOTT, 5, 3
Peimbert, M., Peimbert, A., & Delgado-Inglada, G. 2017, PASP, 129, 082001
Peimbert, M., Sarmiento, A., & Fierro, J. 1991, PASP, 103, 815
Peña-Guerrero, M. A., Peimbert, A., & Peimbert, M. 2012, ApJL, 756, L14
Pogge, R. W., Owen, J. M., & Atwood, B. 1992, ApJ, 399, 147
Rodríguez, M. 1999, A&A, 348, 222
Rogers, N. S. J., Skillman, E. D., Pogge, R. W., et al. 2021, ApJ, 915, 21
Rogers, N. S. J., Skillman, E. D., Pogge, R. W., et al. 2022, ApJ, 939, 44
Rola, C., & Pelat, D. 1994, A&A, 287, 676
Rubin, R. H. 1989, ApJS, 69, 897
Rubin, R. H., Simpson, J. P., Colgan, S. W. J., et al. 2016, MNRAS, 459, 1875
Rynkun, P., Gaigalas, G., & Jönsson, P. 2019, A&A, 623, A155
Santoro, F., Kreckel, K., Belfiore, F., et al. 2022, A&A, 658, A188
Sarzi, M., Falcón-Barroso, J., Davies, R. L., et al. 2006, MNRAS, 366, 1151
Scheuermann, F., Kreckel, K., Anand, G. S., et al. 2022, MNRAS, 511, 6087
Scheuermann, F., Kreckel, K., Barnes, A. T., et al. 2023, MNRAS, 522, 2369
Seaton, M. J., & Osterbrock, D. E. 1957, ApJ, 125, 66
Shaya, E. J., Tully, R. B., Hoffman, Y., & Pomarède, D. 2017, ApJ, 850, 207
Stasińska, G. 1980, A&A, 84, 320
Storey, P. J., & Hummer, D. G. 1995, MNRAS, 272, 41
Storey, P. J., Sochi, T., & Badnell, N. R. 2014, MNRAS, 441, 3028
Tayal, S. S. 2011, ApJS, 195, 12
Tayal, S. S., & Gupta, G. P. 1999, ApJ, 526, 544
Tayal, S. S., & Zatsarinny, O. 2010, ApJS, 188, 32
Taylor, J. 1997, Introduction to Error Analysis, the Study of Uncertainties in Physical Measurements (2nd ed.; Mill Valley, CA: Univ. Science Books)
Thilker, D. A., Braun, R., & Walterbos, R. A. M. 2000, AJ, 120, 3070
Thilker, D. A., Whitmore, B. C., Lee, J. C., et al. 2022, MNRAS, 509, 4094
Thuan, T. X., & Izotov, Y. I. 2005, ApJS, 161, 240

Tokunaga, A. T., & Vacca, W. D. 2005, PASP, 117, 421
Tremblin, P., Anderson, L. D., Didelon, P., et al. 2014, A&A, 568, A4
Vale Asari, N., Stasińska, G., Morisset, C., & Cid Fernandes, R. 2016, MNRAS, 460, 1739
van der Marel, R. P., & Franx, M. 1993, ApJ, 407, 525
van Dokkum, P., Wasserman, A., Danieli, S., et al. 2019, ApJ, 880, 91
van Loon, M. L., Mitchell, P. D., & Schaye, J. 2021, MNRAS, 504, 4817
Vazdekis, A., Koleva, M., Ricciardelli, E., Röck, B., & Falcón-Barroso, J. 2016, MNRAS, 463, 3409
Vazdekis, A., Sánchez-Blázquez, P., Falcón-Barroso, J., et al. 2010, MNRAS, 404, 1639
Vilchez, J. M., & Pagel, B. E. J. 1988, MNRAS, 231, 257
Watkins, E. J., Kreckel, K., Groves, B., et al. 2023, A&A, 676, A67
Weilbacher, P. M., Monreal-Ibero, A., Kollatschny, W., et al. 2015, A&A, 582, A114
Wood, D. O. S., & Churchwell, E. 1989, ApJS, 69, 831
Yates, R. M., Schady, P., Chen, T. W., Schweyer, T., & Wiseman, P. 2020, A&A, 634, A107
Zakardjian, A., Pety, J., Herrera, C. N., et al. 2023, A&A, 678, A171
Zeippen, C. J. 1982, MNRAS, 198, 111
Zhang, S., Zavagno, A., López-Sepulcre, A., et al. 2021, A&A, 646, A25
Zhou, X., Su, Y., Yang, J., et al. 2023, ApJS, 268, 61
Zurita, A., Florido, E., Bresolin, F., Pérez-Montero, E., & Pérez, I. 2021, MNRAS, 500, 2359